FORSCHUNGSZENTRUM ROSSENDORF FZR

Mitglied der Leibniz-Gemeinschaft

Lars Röntzsch

Self-Organization of Nanocluster δ-Layers at Ion-Beam-Mixed Si-SiO$_2$ Interfaces

Diplomarbeit

Lars Röntzsch

Self-Organization of Nanocluser δ-Layers at Ion-Beam-Mixed Si-SiO₂ Interfaces

Diplomarbeit

Self-Organization of Nanocluster δ-Layers at Ion-Beam-Mixed Si-SiO$_2$ Interfaces

Diplomarbeit
zur Erlangung des akademischen Grades
Diplom–Physiker

vorgelegt von

Lars Röntzsch

geboren in Dresden

Institut für Ionenstrahlphysik und Materialforschung

Forschungszentrum Rossendorf

Fachrichtung Physik

Fakultät Mathematik und Naturwissenschaften

der Technischen Universität Dresden

2003

1st examiner / 1. Gutachter: Prof. Dr. rer. nat. habil. W. Möller

2nd examiner / 2. Gutachter: Prof. Dr. rer. nat. habil. J. Weber

Day of submitting / Datum des Einreichens: 26. September 2003

Abstract:

This diploma thesis presents experimental evidence of a theoretical concept which predicts the self-organization of δ-layers of silicon nanoclusters in the buried oxide of a MOS-like structure. This approach of "bottom-up" structuring might be of eminent importance in view of future semiconductor memory devices.

Unconventionally, a 15 nm thin SiO_2 layer, which is enclosed by a 50 nm poly-Si capping layer and the Si substrate, is irradiated with Si^+ ions. Ion impact drives the system to a state far from thermodynamic equilibrium, i.e. the local composition of the target is modified to a degree unattainable in common processes. A region of SiO_x $(x<2)$ – where x is a function of depth – is formed which is not stable.

During annealing, the system relaxes towards equilibrium, i.e. phase separation (via spinodal decomposition and nucleation) sets in. Within a certain time window of annealing, the structure of the system matches with a structure similar to the multidot non-volatile memory device, the principal character of which is a 2D layer of Si nanoclusters of $\approx$3 nm in diameter which is embedded in a 3D SiO_2 matrix at a distance of $\approx$3 nm from the Si substrate.

The physical mechanisms of ion mixing of the two Si–SiO_2 interfaces and subsequent phase separation, which result in the desired sample structure, are elucidated from the viewpoint of computer simulations. In addition, experimental evidence is presented based on various methods, including TEM, RBS, and SIMS. A novel method of Si nanocluster decoration is of particular importance which applies Ge as contrast enhancing element in TEM studies of tiny Si nanoclusters.

Kurzfassung:

In dieser Diplomarbeit wird der experimentelle Nachweis eines theoretischen Konzepts präsentiert, welches die Selbstorganisation von Silizium-Nanoclustern in δ-Schichten vorhersagt, die in das vergrabene Oxid einer MOS-Struktur eingebettet sind. Diese Methode der "Bottom-Up-Strukturierung" könnte von hoher Bedeutung in Hinblick auf zukünftige Halbleiterspeicherbauelemente sein.

In unkonventioneller Weise wird eine 15 nm dicke SiO_2 Schicht, welche zwischen eine 50 nm Poly-Si Deckschicht und das Si-Substrat eingebettet ist, mit Si^+ Ionen durchstrahlt. Die in den Festkörper eindringenden Ionen treiben das System zu einem Zustand, der weit vom thermodynamischen Gleichgewicht entfernt ist, d.h. die lokale Zusammensetzung der Probe wird zu einem so hohen Grade modifiziert, wie er in herkömmlichen Prozessen nicht erreichbar ist. Ein Bereich von nichtstabilem SiO_x ($x<2$) – wobei x eine Funktion der Probentiefe ist – wird gebildet.

Während der Ausheilung relaxiert das System hin zum Gleichgewicht, d.h. Phasenseparation (über den Weg der spinodalen Entmischung und der Nukleation) setzt ein. Innerhalb eines bestimmten Zeitfensters der Ausheilung entspricht die Systemstruktur einer Struktur, die der eines nichtflüchtigen Halbleiterspeicherbauelements ähnlich ist, dessen Hauptmerkmal eine zweidimensionale und ebene Anordnung von Silizium-Nanoclustern von ≈ 3 nm im Durchmesser ist, die in einem Abstand von ≈ 3 nm vom Si-Substrat in die dreidimensionale SiO_2 Matrix eingebettet ist.

Die physikalischen Mechanismen des Ionenmischens der zwei Si-SiO_2-Grenzflächen sowie der anschließenden Phasenseparation, welche in der gewünschten Probenstruktur resultieren, werden mit Hilfe von Computersimulationen beschrieben. Weiterhin werden experimentelle Nachweise erbracht, die auf verschiedenen Analysemethoden beruhen – darunter TEM, RBS und SIMS. Von besonderer Bedeutung ist eine neuartige Methode der Si-Nanocluster-Dekoration, die sich Germaniums bedient, welches den Kontrast von winzigen Si-Nanoclustern in TEM-Untersuchungen erhöht.

Contents

Abbreviations

The following acronyms are used in order to avoid frequently occurring and space consuming expressions. Common scientific and technological terms were taken into account.

AC	alternate current
BC	binary collision
CMOS	complementary metal-oxide-silicon
CS	cross-section
CM	center of mass
dpa	displacements per atom
DC	direct current
EOR	end-of-range
EEPROM	electrically erasable programmable read only memory
FN	Fowler-Nordheim
FT	Fourier transfrom
IBS	ion beam synthesis
KLMC	kinetic lattice Monte-Carlo
MOS	metal-oxide-semiconductor
MOSFET	metal-oxide-semiconductor field-effect transistor
NC	nanocluster
NN	nearest neighbor
OR	Ostwald ripening
PV	plane-view
PVD	physical vapor deposition
RBS	Rutherford backscattering spectrometry
RF	radio frequency
RT	room temperature

RTA   rapid thermal annealing

SCn sample configuration n $(n = \{1,\, 2,\, 3\})$

SBE   surface binding energy

SIMS   secondary ion mass spectroscopy

SIMOX   separation by implantation of oxygen

TEM   transmission electron microscopy

ToF   time-of-flight

ULSI   ultra-large-scale integration

Chapter 1

Morphogenesis

Aggregation and subsequent formation of condensed matter results in various kinds of physical structures. This process of structurization is generally entitled *morphogenesis*. Throughout human history, numerous philosophers, theologians, and scientists dedicated themselves to this elemental subject in order to explain shape and order of physical objects.

Scientific observations have shown that the organization of matter does not necessarily require divine influence. Matter is able to structure itself, macroscopically as well as microscopically. Self-organization is important as it indicates that the evolution of inanimate and, consequently, also of animate entities can be understood in terms of the physical and chemical parameters of the system under study.

Here, we consider the self-organization of physical structures on the nanometer scale – in particular the self-organization of an ensemble of *nanoclusters*. A nanocluster (NC) is in first approximation a spherical agglomerate of several hundreds to a few thousand atoms which is embedded in a host matrix. Therefore, probabilistic considerations are obligatory in order to physically describe evolution and organization of an NC ensemble. Consequently, we tend to describe the corresponding order mechanisms applying statistical, i.e. thermodynamic principles.

From a thermodynamic point of view, the discussion of mechanisms concerning order is inseparably connected to its opposite, i.e. disorder. The second law of thermodynamics contains fundamental features as it introduces entropy, S, as an attractive quantity for isolated systems. Ludwig Boltzmann was the first to interpret an irreversible increase of entropy as an indication of growing atomic disorder [FAI90, EBW98]. Once an isolated system has reached the state of maximum entropy, i.e. the most disordered or most probable state ($S = k_B \ln P$), it has reached thermodynamic equilibrium.

Likewise, in the case of closed systems (at constant volume and temperature) equilibrium is defined by the minimum of another thermodynamic potential – the free energy $F = E - TS$. This implies that in closed systems equilibrium is an outcome of the balance between energy and entropy which is decisively determined by the weighting factor temperature.

Given these considerations one could conclude that a physical system evolves irreversibly towards extreme values of thermodynamic potentials such as entropy or free energy and that differences in the system are equalized by reaching a single and most disordered state. This scenario was thrillingly articulated by Rudolf Clausius who nominated the constant increase of entropy the "heat death" of the universe.

Yet, evolutionary processes which lead to complexity are known and ordered structures, which are in extreme contrast to "equilibrium structures," occur. The decisive characteristic of these systems is their openness, i.e. the exchange of matter as well as energy with the surroundings. External influence can drive a physical system from a state at or close to equilibrium to a non-equilibrium state. In the present case, non-equilibrium is the key for the formation of an ensemble of NCs.

In a fascinating manner, Nobel laureate Ilya Prigogine announced non-equilibrium to be a "source of order" [PRI77, PRI84]. He introduced dissipative structures as stable structures which are formed far from equilibrium and beyond critical parameters. By dissipativity one understands the "export" of entropy. In agreement with the 2nd law of thermodynamics, such dissipative processes can only occur in parts of the universe. They result in ordered structures – or metaphorically speaking in "islands of order" [EBW98].

At this very moment of the prologue, the ion beam comes into play as an instrument to transport both matter and energy into a targeted system. As a result of ion bombardment, the target is forced towards non-equilibrium since its atomic composition is compulsorily changed. This transformation may cause supersaturation in the system as the atomic concentration of the incoming ion species exceeds a critical value, namely the maximum equilibrium solubility in the solid. Similarly, stochiometric excess of matrix components may be achieved by collisional mixing of interfaces.

The system responds to these compositional changes by phase separation, as a result of which stable precipitates are formed. Originating in non-equilibrium, these structures arrange their position and shape in a self-organizing manner, i.e. they evolve to an ensemble of NCs. Note, that the system is "closed" after ion irradiation and, therefore, relaxes from now on towards thermodynamic equilibrium. Thus, the order of the NC ensemble is of transient nature.

To a certain degree, the path of relaxation can be controlled from the outside by adjusting the physical parameters of the system. On the way towards equilibrium, the system runs through a large number of intermediate states which correspond to local minima of the thermodynamic potential. If such a midway state matches with a nanostructure of physical or technological interest, the relaxation process can simply be stopped by rapidly dropping the temperature of the system. Such "frozen" structures are highly remarkable because they would not have been producible applying conventional processes which apply quasi-equilibrium thermodynamics.

From a technological point of view, NCs, which are arranged in a two-dimensional pattern within a three-dimensional matrix, are of particular interest with regard to future semiconductor memory devices. Therefore, morphogenetic methods are required which go far beyond the hitherto applied techniques of semiconductor device fabrication. In this context, self-organization of NCs resulting from ion beam treatments and subsequent phase separation is a highly favorable approach.

Besides all euphoria, a careful and sophisticated choice of the physical parameters is essential in order to guide the system along the specific relaxation path which corresponds to the desired NC arrangement. With good reason, Heinig et al. [HEK03] articulate in a Shakespearean manner the wish of "taming" nanostructures.

The goal of this work is to present methods which experimentally confirm the theoretical concept of self-organization of an NC ensemble in the oxide of a MOS structure which was irradiated with ions previously.

For this purpose, the physical and technological background of the desired NC arrangement is discussed in chapter two, at first.

The subsequent chapter portrays structure and preparation of the samples involved in the experimental investigations and characterizes the methods of sample analysis.

Chapter four deals with ion-solid interactions which drive the system to a state far from equilibrium. The structural modifications of the particular samples are examined from a simulative and experimental point of view.

The relaxation path of the system towards equilibrium is discussed in chapter five. The mechanisms which lead to the formation of the desired NC alignment are theoretically portrayed and experimentally confirmed.

The last chapter summarizes the results and suggests further investigations on this field of physical research.

Chapter 2

Physico-Technological Motivation

Structures on the nanometer scale are of tremendous interest in many fields of science and technology and, therefore, they have intensively been studied in recent years. Particularly in semiconductor technology, the fabrication of future memory devices depends strongly on the ability to reduce device dimensions. The subsequent sections briefly throw light on the principal physical as well as technological peculiarities of nanosized entities – of nanoclusters, in particular.

2.1 Properties of Nanostructures

Nanostructures are in respect to their proportion considered as *mesoscopic*[1] systems. As soon as the structure size decreases and approaches the low nanometer range, the physical properties of the system under study become noticeably functions of size in comparison with the corresponding bulk values.

For technological reasons mentioned below, the NCs, which are considered within the frame of this thesis, consist preferably of semiconducting materials such as Si or Ge. The NC diameter ranges between one and a few nanometers. That indicates that the NC dimension is considerably larger than a diatomic bond length[2] but significantly smaller than the hitherto minimum feature size in semiconductor device fabrication.[3] Due to the tininess, the NC can be considered as *quantum dot* or "artificial atom", i.e. its electronic states are quantized and the density of states $\varrho(E)$ is singular, e.i.

$$\varrho(E) = \delta(E - E_\alpha) \tag{2.1}$$

for an electron gas occupying the quantized energy level E_α. The energetic spacing between neighboring energy levels increases with decreasing cluster size. Given an insulating matrix surrounding the NC, the cluster can be regarded as a potential well of finite depth. In order to illustrate this energetic peculiarity, the NC can be interpreted as a spherically symmetric potential well. Therefore, the wave function $\Psi(\vec{r})$ of a bound electron is expected to be spherically symmetric, too. Thus, the Schrödinger equation is separable and the radial component of $\Psi(\vec{r}) = R(r)\Theta(\theta)\Phi(\phi)$ obeys for a particle of effective mass m^* the following relation (angular momentum is not considered here, i.e. $l=0$):

---

[1]Gk. μέσος = middle; intermediate.
[2]For example, $d_{\text{Si–Si}} = 0.235$nm.
[3]Nowadays, ULSI lithography minimally reaches 0.13μm.

$$-\frac{\hbar^2}{2m^*}\left(\frac{2}{r}\frac{\partial}{\partial r}+\frac{\partial^2}{\partial r^2}\right)R(r)+V(r)R(r)=E_rR(r)\ .\qquad(2.2)$$

In figure 2.1, numerical solutions (spherical Bessel functions) for a spherical quantum dot of 3 nm in diameter are presented which were calculated with EFSDOT, a numerical simulation program by Harrison [HAP00].
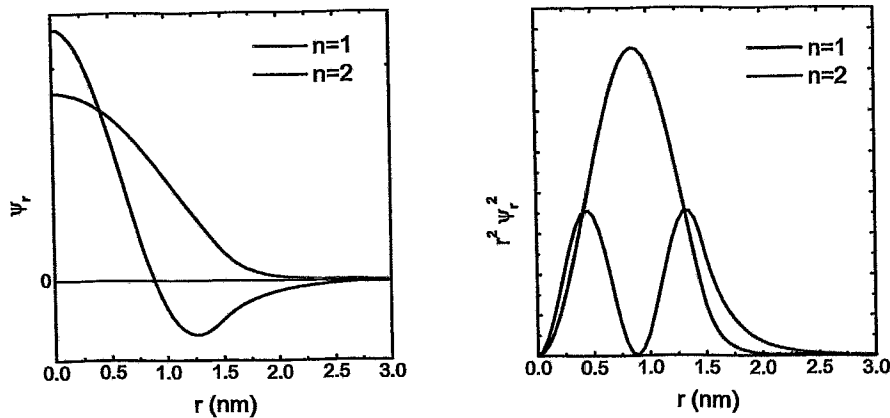
Figure 2.1: The radial components of the wave functions ψ_r and the corresponding charge densities $r^2\psi_r^2$ of the two lowest energy states in a 3 nm spherical quantum dot.

In this context, the cluster acts as a trap for particles, e.g. electrons or holes, since it confines particles with zero classical degrees of freedom. This effect of quantum (or rather particle) confinement is a principle electronic aspect of the nanostructures investigated in the present work.

A further striking feature of nanosized dimensions is *tunnelling* of charge carriers, i.e. the penetration of particle wave functions through a narrow potential barrier which they could not overcome in the corpuscular picture of classical physics. Quantum Mechanics claims that tunnelling through a finite potential barrier requires an empty state on the same energy level on the opposite side. Therefore, it is probabilistically favorable to provide on the one side of the potential barrier spatially extended systems, such as bulk semiconductors, which have a continuous band of energy levels. Thus, charge carriers of corresponding energy can flow through the potential barrier on or off a quantized energy level in the NC[4] (see fig. 2.2).

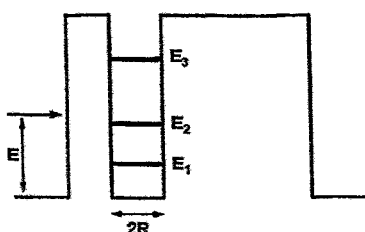[4]The number of electron energy levels in a NC is *finite*.

Figure 2.2: The narrow barrier on the left side permits tunnelling of particles with energy E_p $(0 < E_p < E)$ through the barrier occupying the quantized energy levels E_1 and E_2 in the cluster.

As soon as the barrier width falls below a characteristic value, which mainly depends on the height of the barrier, the tunnel probability drastically increases resulting in the observation of a substantial tunnel current. Concerning this, different tunnel mechanisms exist which are specified in section 2.3. By applying external electric fields to the system the shape of potential barriers and wells can partially be manipulated which may result in a desired electronic behavior.

In addition, semiconducting NCs show a size-dependent energy gap, as demonstrated in fig. 2.3, which inherently affects the electronic behavior.
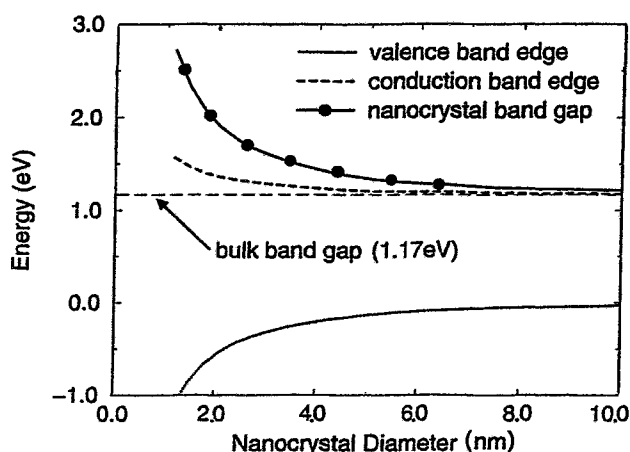

Figure 2.3: The band gap energy as function of the NC radius is shown for a spherical Si quantum dot. These graphs were calculated by a tight-binding technique. Here, the band edge positions have an uncertainty of 0.05 eV. [KIL97, TAT92]

Moreover, NCs are fascinating from a stereometric point of view since their surface-to-volume ratio is significantly larger in comparison with bulk materials which implies that the properties of the NCs are remarkably determined by surface or rather interface contributions. For example, the impurity equilibrium solubility, c, of monomers above a curved surface increases exponentially with decreasing curvature radius R which is expressed in the Gibbs-Thomson relation [STM96, STM01]:

$$c^{GT}(R) = c_\infty \exp\left(\frac{R_c}{R}\right) . \tag{2.3}$$

This equation becomes of particular interest during growth and arrangement of an ensemble of NCs which is examined in chapter 5 in detail.

2.2 Technology Roadmap of Nanoelectronics

Under the predictive pressure of Moore's law, postulating that the processing power of microelectronic circuits doubles every 18 months, technologists have pushed semiconductor devices to smaller and smaller dimensions over the last four decades [TRNE].

This permanent reduction of device dimensions has generated tremendous technical and economic benefits which concern for instance

- higher operating speeds,

- higher data storage densities,

- lower power consumption, and

- extremely reduced fabrication costs per bit.

Until today, a minimum feature size in semiconductor device fabrication of 0.13μm has been achieved. Enormous effort was put into optimization and improvement of conventional circuit scaling technologies which are mainly based on lithographic methods. This conservative *top-down* approach, however, will face serious difficulties in the remote future because the physical limits of optical lithography, i.e. the continuous wave length lowering, come into sight – quite apart from gigantic developmental costs. Therefore, it seems more than reasonable to develop alternative and unorthodox methods.

From a fundamental point of view, the generation of structures in the reverse mode, i.e. in the *bottom-up* approach, is highly promising. Nonetheless, in accordance with the "unwritten law of conservation of difficulty," important physical and technological questions remain to be answered which concern the assembly of single atoms or molecules culminating in the formation of nanosized structures, e.g. NCs, and even complex patterns of these structures.

As mentioned previously, the ability of matter to structure and to organize itself is a key element in the strategy of building up nanosized species. The physicists' and technologists' community has encountered severe difficulties in finding appropriate physical process parameters which lead to well-defined and mono-disperse species.

The Technology Roadmap for Nanoelectronics [TRNE] summarizes the demands on the bottom-up approach for becoming competitive to conventional top-down methods as follows:

Self-assembled structures

1. must be locatable at a desired position in space,

2. must be electronically addressable, and

3. must be integrative in CMOS technology.

The latter demand limits the choice of elements, from which self-assembled nanostructures can be constructed, to a few metals and semiconductors.

The most favored element is doubtlessly silicon since it is physically and chemically the most investigated material worldwide.[5] Moreover, Si does not electronically interfere with the functionality of already existing devices in CMOS technology. The same holds for Ge due to the equal number of valence electrons. Besides that, Ge shows chemical, crystallographic, and electronic properties similar to Si.

---

[5]Anthropologically speaking, we are living in the Silicon Age!

In the previous section, the possibility of electron (or hole) trapping was pointed out as a striking physical feature of NCs. If charge carriers like electrons or holes were confined in a potential well a quantum dot memory could be realized. For this purpose, two well-distinguishable characteristic curves of the memory device – micro-electronically speaking "0" and "1" – have to been defined referring to the occupied or empty potential well. If one imagines a single bit being reliably stored and erased in a single NC, data storage densities would rapidly scale up by many orders of magnitude beyond the hitherto achieved values. Instantly, this scenario reminds of Feynman's vision concerning the "plenty of room at the bottom." [FER59]

Besides data storage density, other relevant electronic properties of memory devices are subject of improvement, as for instance retention time, operating voltage, or endurance. With respect to this, figure 2.4 compares future quantum dot memory devices with conventional memory devices.
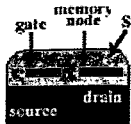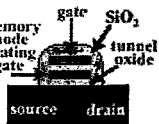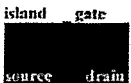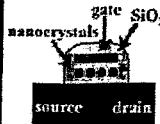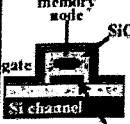
	Conventional Memory		Quantum Dot Memory		
	DRAM	Flash	SET	Nano-flash		Yano-type
				Multidot	Single dot	
device structure						
read time	~6 ns	~6 ns	1 ns	~10 ns	~10 ns	~20 µs
write time	~6 ns	1 ms	1 ns	~100 ns	<1 µs	~10 µs
erase time	< 1ns	~ 1 ms	< 1 ns	~1 ms	<1 ms	~10 µs
retention time	250 ms	~10 years	~ 1s	~1 week	~5 s	~1 day
endurance cycles	infinite	10^6	infinite	10^9	10^9	10^7
operating voltage	1.5 V	10 V	1 V	5 V	10 V	15 V
voltage for state inversion	0.2 V	3.3 V	< 0.1 V	0.65 V	0.1 V	0.5 V
electron number to write bit	10^4	250	1 (excluding no to change gate potential)	10^3	1 (excluding no to change gate potential)	2 (excluding no to change gate potential)
cell size	8.5 F^2/bit	~9F^2/bit	9-12 F^2/bit	9F^2/bit	9F^2/bit	2F^2/bit

Figure 2.4: This figure presents a comparison between conventional, multidot, and single dot electron memory devices according to the Technology Roadmap of Nanoelectronics [TRNE]. Here, the cell size is given in units of the minimum feature size squared per bit (F^2/bit).

Depending on the field of application, various memory devices are employed – among of which *non-volatile* memories. They allow data storage without frequent external refreshment, i.e. the information is reliably stored over long periods of time without power supply.

Today, the conventional flash memory is used for this purpose. This type of memory is structured like an ordinary MOSFET, whereas a so-called "floating gate" (which is usually a few nanometer thick poly-Si layer) is incorporated in the transistor's gate oxide. By charging or erasing the floating gate, two well-distinguishable states, "0" and "1", are realized (see fig. 2.5).
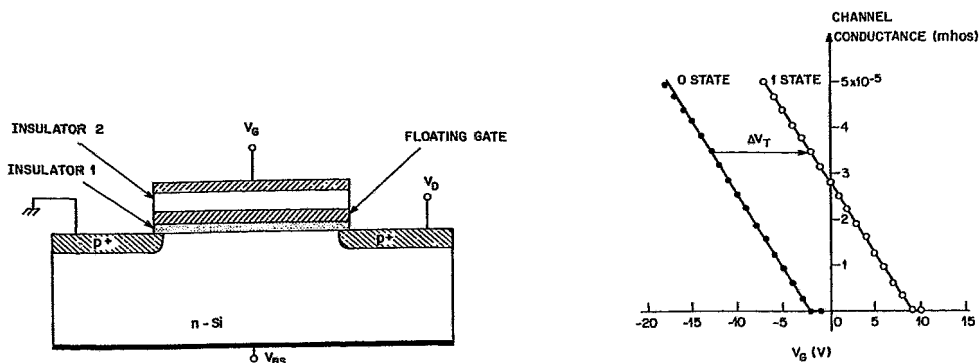

Figure 2.5: Electrons from the Si substrate are injected through the tunnel oxide (insulator 1) in the floating gate by applying a sufficient gate voltage V_G. Thus, a threshold voltage shift ΔV_T of the transistor is generated defining two well-distinguished states in terms of the transistor's channel conductance g_D [SZS81].

Conventional floating gate memories, however, show one decisive disadvantage. One single defect in the tunnel oxide can cause the discharge of the entire floating gate. A defect in the tunnel oxide may act as drain through which electrons, i.e. the carriers of information in this case, dissipate. Thus, conventional floating gate memories have tunnel oxide thicknesses of several (8...12) nanometers in order to prevent charge dissipation. These oxide thicknesses, however, merely permit Fowler-Nordheim (FN) tunnelling through a triangular oxide barrier [SZS81] (see fig. 2.6). FN tunnelling requires high electric fields in order to achieve a sufficient band deformation (see ibid.).
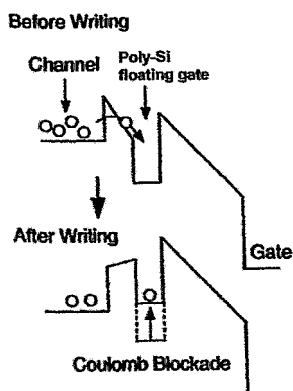
Figure 2.6: The band deformation generated by the applied gate voltage causes FN-like tunnelling from the Si substrate through a triangular barrier to the poly-Si floating gate. The tunnel current, J_{FN}, rapidly decreases when the total charge of the floating gate reduces the value of the electrical field strength, E, in the tunnel oxide [SZS81, SZS98]: $J_{FN} \propto E^2 \cdot \exp(-1/E)$. This phenomenon is generally known as "Coulomb blockade."

Electrons, which are accelerated by high electric fields, are likely to break atomic bonds. These hot carrier transport mechanisms cause the electrical degradation of the oxide which additionally limits endurance and data retention of the conventional floating gate memory cell.

One potential way to overcome these handicaps are quantum dot nano-flash memories (see fig. 2.4). The intermediate step from conventional flash memories towards the single dot nano-flash memory is the "multidot" nano-flash memory (framed in red ibid.). Here, the floating gate is broken up into a large number of electrically insulated quantum dots which act as individual charge traps. Thus, collective charge dissipation of the entire floating gate is prevented. Besides that, the multidot nano-flash memory exhibits further advantages which are – together with structural peculiarities – the object of illustration in the subsequent section.

2.3   Multidot Non-volatile Memory

The characteristic concept of a multidot non-volatile flash memory is the usage of a layer of equally sized NCs, which are a few nanometers in diameter, as floating gate instead of a continuous poly-Si layer (see fig. 2.7). For the first time, this concept was published by Tiwari and coworkers [TIS96a, TIS96b].
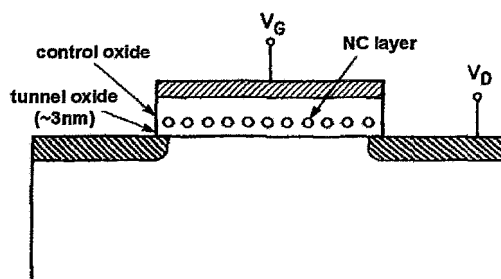

Figure 2.7: A modified MOSFET cell which contains a δ-layer of NCs, each of which is surrounded by SiO_2. The NC layer is aligned parallel to the Si substrate, from which it is separated by a tunnel oxide ($t_{tox} \approx 3nm$).

Insulating of individual NCs by a surrounding SiO_2 matrix prevents charge loss of the entire floating gate. In the case of local defects in the tunnel oxide, only those NCs are discharged which are positioned in the very region of the defect, whereas the majority of NCs remains charged and, thus, the information of the memory cell can be preserved. This requires, however, an average distance between single NCs in the range of the tunnel oxide thickness. Otherwise, thermally assisted quantum mechanical tunnelling of electrons from cluster to cluster is probable which results in information loss as well. This phenomenon, known as charge percolation, limits the NC density in the cluster layer which was structurally investigated by Müller et al. [MUT02].
Since total charge dissipation is prevented, the tunnel oxide of a multidot floating gate structure can be very thin ($\approx 3\,nm$) which allows direct quantum mechanical tunnelling of electrons as charge injection mechanism.
Tiwari et al. [TIS96a, TIS96b] pointed out that low electric fields of about 2 to $5\,MeVcm^{-1}$ are sufficient[6] and that the barrier, through which the electrons tunnel, remains trape-

---

[6]The corresponding gate voltage V_G ranges from 3 to $7.5\,V$ for a total oxide thickness of $15\,nm$.
In comparison, common poly-Si floating gate memories operate at gate voltages between 12 and $20\,V$.

zoidal (see fig. 2.8). Thus, the power consumption of the memory device can be reduced, and the oxide remains much longer electrically functional.
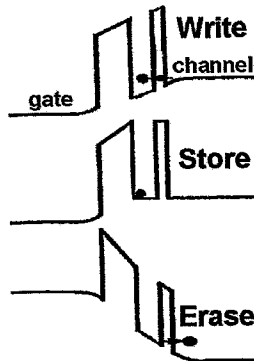

Figure 2.8: The band diagram is schematically drawn for charge injection, storage, and removal. Electrons tunnel quantum mechanically through a thin oxide to/from the cluster depending on the polarity of the applied electric field (after [TIS96a]).
Again, Coulomb blockade effects occur depending on the capacitance C_{NC} of individual NCs.

The storage of electrons in the NC δ-layer causes a shift of the MOSFET's threshold voltage, ΔV_T, which defines two well-distinguishable electronic states as pointed out previously. Assuming that a single electron is stored per NC, this threshold voltage shift is given by [TIS96a]:

$$\Delta V_T = \frac{q\, n_{NC}}{\epsilon_0\, \epsilon_{ox}} \left(t_{cont} + \frac{\epsilon_{ox}}{2\epsilon_{Si}} t_{NC} \right) \,, \tag{2.4}$$

where n_{NC} denotes the NC density, ϵ_0, ϵ_{ox}, and ϵ_{Si} permittivities, q the magnitude of electronic charge, t_{cont} the control oxide thickness, and t_{NC} the average dimension of the NCs. In order to achieve an electronically reasonable threshold voltage shift (see fig. 2.9) of some hundred millivolts, NC densities of about $10^{12}\,\text{cm}^{-2}$ are required[7].
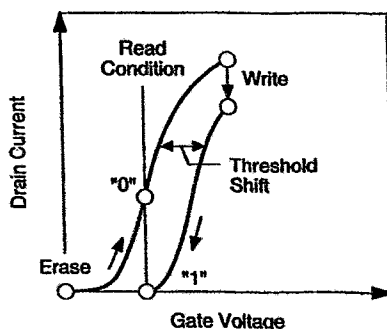

Figure 2.9: Raising the gate voltage causes electron injection into a multidot floating gate structure, as a result of which a shift in the threshold voltage of the MOSFET, ΔV_T, is observed. The two well-distinguishable characteristic curves express the usability as memory cell. (after [SZS98].)

The quantum mechanical tunnel mechanism assumes an ideal, i.e. an stoichiometrically and electronically integer, tunnel oxide. In reality however, the potential barrier is less perfect due to Si-SiO$_2$ interface states or defects within the oxide itself, all of which may affect and induce further tunnel mechanisms [SZS81]. In addition, these different processes may overlap and assist themselves in a certain parameter range which complicates the description of the electron injection mechanism to a further degree.
A discussion of these various processes is beyond the scope of this work. The interested reader is referred to the literature (see, for example, [SHY98] and given references therein).

---

[7]e.g. ΔV_T=0.32V for n_{NC}=10^{12}cm^{-2}; t_{cont}=7nm; t_{NC}=3nm; ϵ_{ox}=4.3; and ϵ_{Si}=11.9.

Likewise, the charge storage mechanism of multidot memory structures is still under intense discussion [SHY99]. The picture of electrons falling in the potential well of a NC, where they are three-dimensionally confined, does not exclude the possibility that electrons are directly trapped by oxide defects or by defects at the interface between the NCs and the SiO_2 matrix.

The synthesis of a MOS-like structure containing a NC layer at a distinct position in the oxide has become a severe challenge for materials scientists and physicists. Different technologies have been investigated based on disparate physical and chemical processes, as for instance CVD [TIS96a, TIS96b, HRB03], PVD [SCJ03], or conventional IBS [OHT94, BOJ99, BOJ02]. In order to attain the above described memory behavior, all methods have to meet the following structural aspects of the multidot memory cell:

- Si (or Ge) as preferred NC material,

- an approximate NC density of $10^{12}\,cm^{-2}$ in the δ-layer,

- NCs of roughly 3 nm in diameter,

- isodistant and isodiametric NCs,

- a tunnel oxide thickness of 2 to 3 nm, and

- an electronically and stoichiometrically integer oxide.

Besides these tough structural demands, the technological process has to be reliable as well as reproducible to a high degree of precision.

An unconventional method to produce a NC δ-layer was suggested by Heinig et al. [HEK01, HEK03]. They theoretically predicted the NC δ-layer formation by means of self-organization. This novel "bottom-up" approach is roughly divided into two parts:

1. medium energy ion irradiation through a MOS structure causing ion mixing of the Si-SiO_2 interface and

2. subsequent phase separation by thermal treatment.

A single medium energy ion implantation step provides the advantage of being entirely compatible and integrable in CMOS technology. Differently from conventional IBS of NCs, the excess of Si in the SiO_2 matrix is generated by ion mixing of the Si-SiO_2 interface rather than by direct Si implantation into the oxide.

Earlier experimental investigations, in which a conventional SiO_2 layer on top of a Si substrate was irradiated, suggested the correctness of this theoretical concept.

However, experimental evidence, that an irradiated MOS structure exhibits NC δ-layers in the oxide after thermal treatment, still has to be given. It became apparent that the direct structural proof of the existence of a Si NC layer within SiO_2 is very difficult due to the peculiarities of the principal method of analysis – common high resolution TEM.

The goal of this work is to present experimental evidence (including TEM) concerning the existence of Si NC δ-layers in the oxide of a MOS structure after ion irradiation and subsequent phase separation. Thus, the theory of self-organization of NCs in a δ-layer would be strongly supported.

Chapter 3

Preparation and Analysis

In order to illustrate the course of experimental investigations, the initial configuration of the samples, the course of sample preparation, and the analytic methods, which were used to determine the structural outcome of ion mixing and subsequent phase separation, are addressed in this chapter.

3.1 Initial Sample Design

Different MOS layer stacks, which are illustrated in the figures 3.1, 3.2, and 3.3, were experimentally examined. The structural variations originate from the choice of materials resembling the gate of the MOSFET.
Unfortunately, amorphous (and even crystalline) Si NCs of 2...3 nm in diameter within a SiO_2 matrix are not observable in TEM due to the weak Z-contrast. Thus, Ge was used to decorate the Si clusters by enhancing the contrast in TEM. Accordingly, three different layer structures were investigated two of which contain a Ge layer. The corresponding physical and analytical background is discussed in the subsequent chapters.

50nm poly-Si

15nm SiO₂

(100)Si substrate
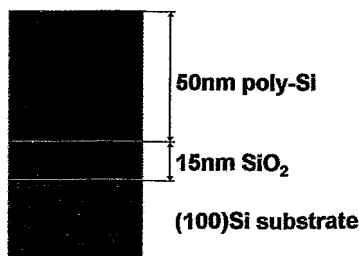
Figure 3.1: Block diagram of sample configuration 1 (SC1).
The original MOS structure – a poly-Si gate on top of the gate oxide.

50nm poly-Si

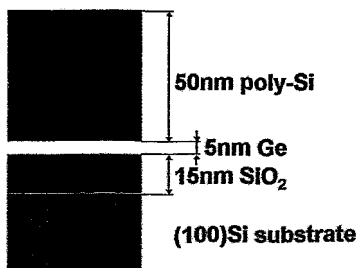**5nm Ge**

15nm SiO₂

(100)Si substrate

Figure 3.2: Block diagram of SC2.
A Ge layer was inserted in between poly-Si and the oxide as a first variation of SC1 in order to improve the contrast of the NCs in TEM.
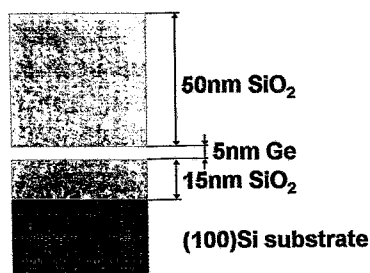
50nm SiO$_2$

5nm Ge
15nm SiO$_2$

(100)Si substrate

Figure 3.3: Block diagram of SC3. In a further variation, the poly-Si capping layer was substituted by SiO$_2$. Thus, the Ge layer is symmetrically surrounded by oxide. This strongly increases the expected contrast enhancement in TEM.

3.2 Wafer Preparation

Prior to the implantation step, numerous samples had to be prepared, consisting of

- a Si substrate in (100) orientation,

- an oxide layer, and

- a capping layer resembling the gate.

Starting from virgin 3" Si wafers of p-type, oxide layers of 15 nm were thermally grown. In the case of SC1, the capping Si layer was deposited in a standard CVD process at ZMD[1].

In the case of SC2 and SC3, however, the Si, Ge, and SiO$_2$ capping layers were deposited in an in-house magnetron sputtering process. For the sake of simplicity, the capping Si layer of SC2 is also denoted as "poly-Si" throughout this work, even though the layer is amorphous after deposition.

All these assignments were performed in a "class 100" clean room in order to achieve constant ambient conditions and to minimize wafer contamination throughout the course of preparation.

3.2.1 Oxidation

Even a blank Si wafer is covered by a few nanometer thin layer of natural oxide. In order to grow a SiO$_2$ layer of well-defined thickness, identical initial conditions for all wafers were necessary. Therefore, the natural oxide had to be completely removed prior to the oxidation step. This was performed in an etching process applying a 0.5% hydrofluoric acid (HF) solution which passivates the wafer surface for several hours. Thus, the wafers were prevented from naturally reoxidizing.

Subsequently, all wafers were immediately positioned in an furnace tube which had been heated up to 900 °C, previously. By closing the furnace, dry oxygen of a flow of constantly 1 l·min^{-1} started to stream through the tube (see fig. 3.4).

Thus, a dry ambient of constant oxygen concentration c_g was achieved to which the Si wafers were exposed.

Silicon covalently bonds to oxygen, and SiO$_2$ is formed. The oxidation mechanism is well understood which allowed a precise determination of the duration of the oxidation resulting in the desired oxide thickness – 50 min for an oxide thickness of 15 nm.

Fig. 3.5 schematically depicts the oxidation kinetics after Deal and Grove [NIY00]. The

---

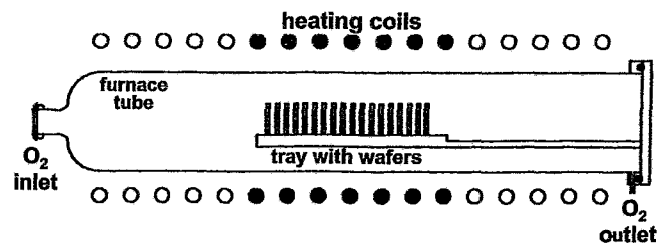[1]=Zentrum Mikroelektronik Dresden, partner in "NEON."

Figure 3.4: After HF etching, a tray of silicon wafers was placed into the furnace tube where they were oxidized. During oxidation, the temperature in the furnace was kept constant by heating coils surrounding the tube (after [HIU99]).

rate of oxide growth is determined by the amount of available silicon, the amount of available oxygen molecules, and the rate of the reaction. The oxidation proceeds by diffusion of the oxidant through the oxide which leads to a further oxidation of silicon at the buried interface.
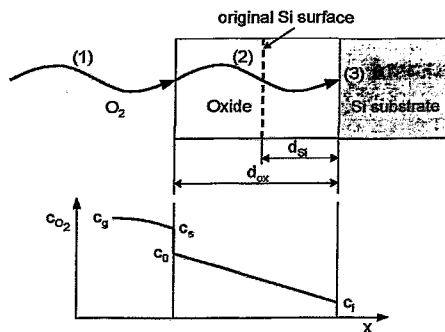

Figure 3.5: Oxidation results in consumption of Si. The produced SiO_2 film takes up double the volume compared to the initial Si layer: $d_{Si} \approx 0.46 \, d_{ox}$.

Permitting a tolerance of ± 1 nm, the simultaneous oxidation of a set of wafers generated equally sized oxide films on all wafers. These values were measured by ellipsometry – a standard method for this purpose. For a physical and technical description, the reader is referred to [AZR87].

The thermal growth of SiO_2 in dry oxygen ambient at a relatively low temperature of 900 °C produces an oxide density of 2.28 g/cm^3 [HIU99] which corresponds to an atomic density of 6.855 atoms/cm^3.

3.2.2 Deposition by Magnetron Sputtering

In several experimental runs, various layer sequences of distinct species were deposited by magnetron sputtering on top of the oxide layer.

Magnetron sputtering belongs to the realm of PVD processes. It is an extensively employed plasma deposition technique. The material to be deposited on a substrate is detached from a target by the impact of charged plasma ions (Ar^+) upon the atoms in the region next to the surface of the target. Due to nuclear collisions, energy is transferred from the incoming particles to the target atoms, as a results of which a collision cascade is established, within of which the momentum of the incoming ions is partially reversed. As soon as the energy transfer of a binary collision exceeds the

bulk binding energy of a target atom of the outermost atomic layers, the target atom leaves the target and is sputtered onto the substrate (see fig. 3.6).
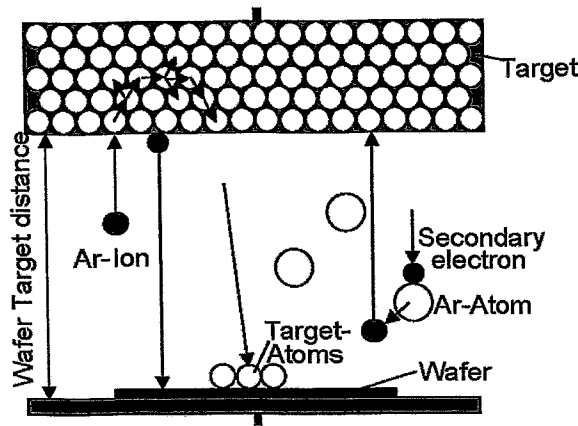

Figure 3.6: Sputtered target atoms are deposited on a substrate which leads to layer growth.
(after [HAJ01])

Basically, there are two different modes of sputtering:

1. **DC mode**, i.e. the target is negatively biased, thus, positive ions are accelerated towards the target and knock on target atoms. This mode could only be applied to Si and Ge which are conductive target materials – insulating substances (SiO_2) would accumulate charge at the surface interrupting the process.

2. **RF mode**, i.e. an AC voltage with a 13.56 MHz [SCJ03p] radio frequency is applied to the target and a second electrode (substrate). During two half waves, positive ions (in the negative half wave) or electrons (in the positive half wave) are alternatingly accelerated towards the target. In comparison to Ar ions, electrons have a higher mobility, thus, the target surface is negatively charged on average.[2] Therefore, also dielectric target materials like SiO_2 can be sputtered since the positive Ar ions are not repelled from the target by Coulomb forces.

The Si and Ge layers were deposited in an inert DC mode whereas the SiO_2 capping layer of SC3 was produced in an reactive RF mode, i.e. as a supplement to Ar, a small amount of oxygen was added to the plasma in order to guarantee stoichiometrically pure SiO_2 in the deposited layer. Examinations by Schmidt had demonstrated that sputtering of a SiO_2 target in an inert RF mode generates slightly sub-stoichiometric oxides ($SiO_{1.95...1.98}$) [SCJ03p].
The deposition was executed in the vacuum chamber NORDIKO 2000 which is schematically depicted in fig. 3.7 [SCJ03t].
The growth rate of the deposited layers could be manipulated by several process parameters. A listing of the used parameter values is compiled in table 3.1.

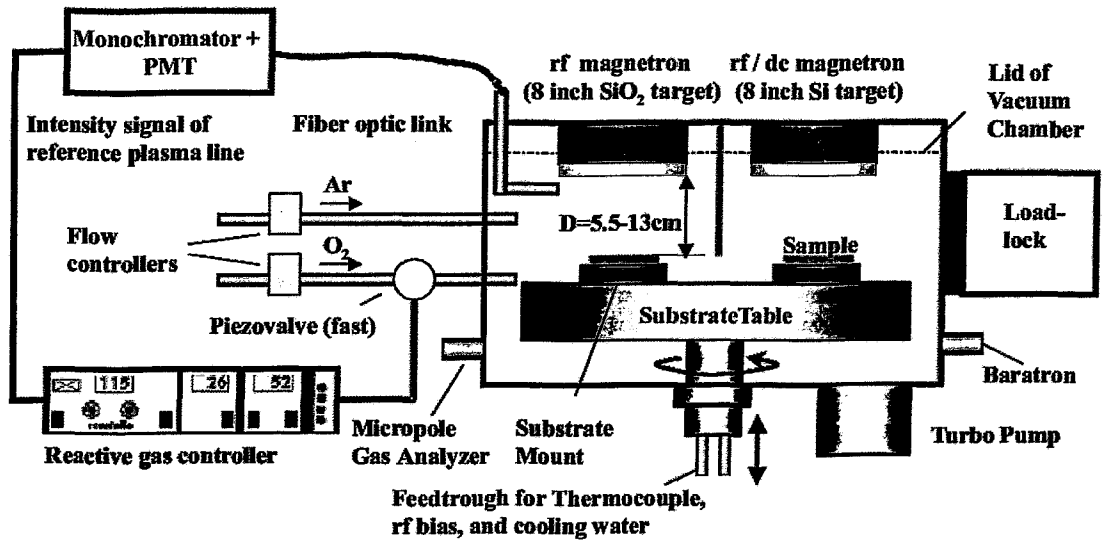[2]This phenomenon is called "negative self-biasing" [SCJ03p].

Figure 3.7: The sputter tool NORDIKO 2000 provides numerous features. For instance, the substrate table can be rotated which allows low growth rates of the deposited layers down to 0.2 nm/s.

	Si	SiO$_2$	Ge
sputtering mode	DC	RF	DC
chamber pressure (μbar)	6.7	6.7	6.7
process gas flow (sccm)			
Ar	50	46	50
O$_2$	-	6	-
throttle valve	50%	50%	50%
$P_{\text{sputtering}}$ (W)	250	1000	200
$t_{\text{sputtering}}$ (s)	133	107	30
substrate rotation (rpm)	-	-	30
separation	0%	0%	20%
nominal layer thickness (nm)	50	50	5
layer thickness from TEM (nm)	54.8	43.7	5.7
layer thickness from RBS (nm)	52.1	43.4	5.6

Table 3.1: The presented parameter values are outcomes of simple deposition rate experiments which were conducted previously in order to obtain the desired nominal layer thicknesses. Here, ellispometry served as method of measuring the layer thicknesses. The results of ellipsometry, from which the appropriate parameter values were calculated, are in adequate agreement with the outcomes of TEM and RBS (see sections 3.3.1 and 3.3.2.)

3.2.3 Ion Implantation

After layer deposition, the samples were implanted with Si^+ ions at energies $E=\{50;$ $100\}$ keV and various fluences up to $5 \cdot 10^{16}\,cm^{-2}$.

From an experimental point of view, the Si^+ implantations were performed in an Alpha 500kV implanter by High Voltage, a schematic drawing of which is presented in figure 3.8.

In the case of implantations at RT,[3] the target holder is generally tilt by an angle of 7° in order to avoid channelling. The deviation from normal incidence, which was predefined throughout all simulation runs, is negligible in terms of damage and implantation profiles since $\cos(7°)$=0.9925!

In the cases of $T_{implantation}=\{400; 600\}$°C, a heating target holder had to be used which only allowed normal incidence.

On average, ion currents of about 2 to $3\mu A$ were achieved.
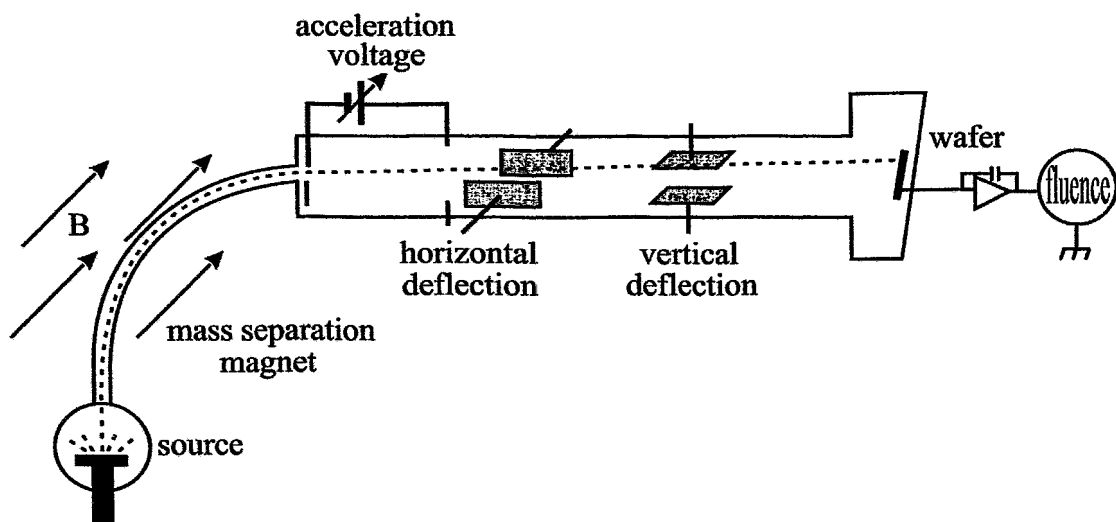
Figure 3.8: Block diagram of the ion implanter (after [MOT00]). For the sake of clarity, only one Faraday cup is drawn in this illustration. In the present cases, however, the ion fluence was measured with four Faraday cups which symmetrically surround the wafer.

---

[3]In the present case of a relatively low ion flux ($\Phi \approx 10^{12}\,s^{-1}cm^{-2}$), the temperature of the target slightly increases during implantation. Thus, RT actually means the temperature interval between 20 and 100°C.

3.2.4 Rapid Thermal Annealing

Under clean room conditions, all samples were annealed in the rapid thermal processor ADDAX XM, a schematic drawing of which is presented in fig. 3.9. The use of halogen lamps and a high temperature infrared pyrometer guaranteed a precise control of annealing time and temperature.

Prior to and subsequent to annealing, a mixture of inert process gases (N_2 and Ar) streamed through the RTA chamber for several minutes. During annealing, only Ar was used as process gas, thus, preventing chemical impact from the ambient.

The samples were heated up to the predefined annealing temperature with a constant rate of 15 K/s. The same rate was chosen for cooling the samples down. This rather moderate change in temperature was chosen in order to allow the system to accommodate to the temperature induced stress in the layers [FLA89].
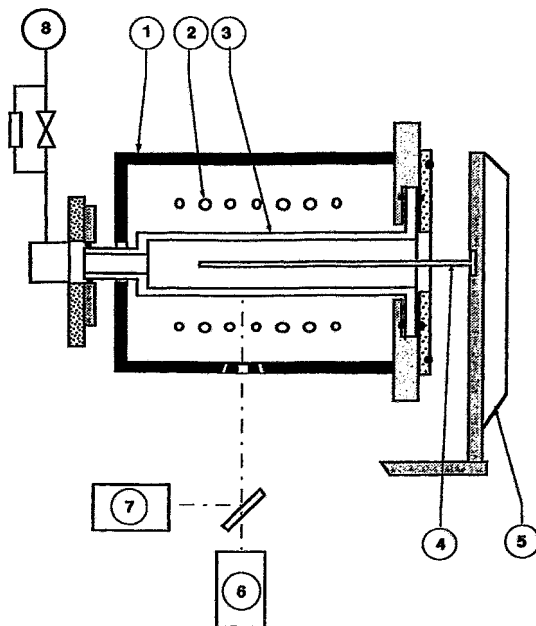

Figure 3.9: Block diagram of the rapid thermal processor ADDAX XM (after [ADA93]).

1   furnace
2   quartz halogen lamps
3   quartz chamber
4   quartz support
5   door
6   low temperature pyrometer
7   high temperature infrared pyrometer
8   gases evacuation system

3.3   Sample Analysis

Since the investigations deal with the generation of NCs, the *structure* of the samples was of principal interest. For this purpose, three analytical methods were mainly employed:

- (high resolution) TEM for a pictorial characterization in cross-section (CS) and plane-view (PV) images,

- RBS for determining element-specific area densities, and

- ToF-SIMS for stoichiometric depth profiling.

The following sections describe the physical principles of these methods. As-deposited samples of the three layer configurations will serve as illustrative examples.

3.3.1   TEM

High resolution micrographs are certainly the most illustrative and convincing arguments in the proof of the existence of NCs. Thus, a significant number of TEM images had to be taken in order to recognize the influence of the several process parameters on shaping and positioning of the NC ensemble.

In TEM, a focused high energetic electron beam radiates through the sample by which some of the electrons are scattered. This interaction strongly depends on the structure and the elemental composition of the specimen. After passing the sample, both the transmitted and the scattered part of the electron beam are guided through a system of electromagnetic lenses and is finally projected onto a screen. Thus, a highly magnified real image of the sample structure becomes visible. See fig. 3.10 for a plain impression of the ray path in the bright-field image mode of TEM (after [AMS97]), which was mostly used in search of NCs.
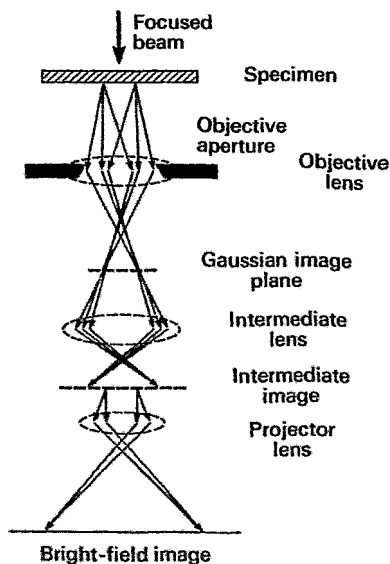

Figure 3.10: In the bright-field image mode, a beam of collimated electrons is partially scattered by the specimen. An image is formed in the image plane of the objective lens. The intermediate lens is focused on the image plane of the objective lens and an intermediate image is formed in the image plane of the intermediate lens. This image is the object for the projector lens which forms a final image on a projection screen. For a detailed physical and technical description of TEM, the reader is referred to [AMS97, BUP92].

The samples were examined in a PHILIPS CM 300 microscope, the point resolution of which is about 0.14 nm. A GATAN CCD camera served as recording device for the final image.

Unfortunately, Si NCs less than 3 nm in diameter within an amorphous SiO_2 matrix are only detectable in TEM if they are crystalline. This limitation originates from the weak mass contrast between amorphous Si and a-SiO_2 because scattering of electrons is based on Coulomb interaction, the strength of which increases with increasing atomic number Z of the scatterer.

In case of crystalline Si NCs, however, high resolution TEM would depict the lattice planes of the clusters which would attract the observer's attention in contrast to the non-crystalline amorphous surroundings. This requires, nonetheless, a minimum cluster size in order to achieve a sufficiently strong signal originating from coherent electron diffraction at the *periodic* crystal lattice of the NC. Crystalline Si NCs with a diameter of less than 3 nm within SiO_2 have not been observed which opens two possible interpretations: firstly, clusters smaller than 3 nm are generally amorphous, or, secondly, they are crystalline but the signal originating from coherent scattering at the lattice planes is to weak to be observed in high resolution TEM images.

In conclusion, the only way to indicate tiny Si NCs is to enhance their Z contrast. In view of the limitation of the TEM device at FZR, Ge ($Z_{Ge} \approx 2.6 Z_{Si}$) came into play in order to "decorate" already existing Si clusters. Consequently, $Si_x Ge_{1-x}$ clusters exhibit a significant contrast enhancement and, thus, indirectly prove the pre-existence of tiny Si clusters prior to decoration. Details concerning the growth kinetics of Si and $Si_x Ge_{1-x}$ clusters are discussed in chapter 5.

TEM images are generally two-dimensional projections of three-dimensional specimens. Thus, varying image perspectives support the understanding of the three-dimensional sample structure. Usually, cross-section (CS) images were taken since they depict the vertical sample structure in accordance with the block diagrams (see figs. 2.4 and 2.7). In the case of SC3, plane-view (PV) images were taken, too. Here, the capping SiO_2 layer does not disturb the view on the buried cluster ensemble. These two *modi observandi* are schematically illustrated in fig. 3.11.
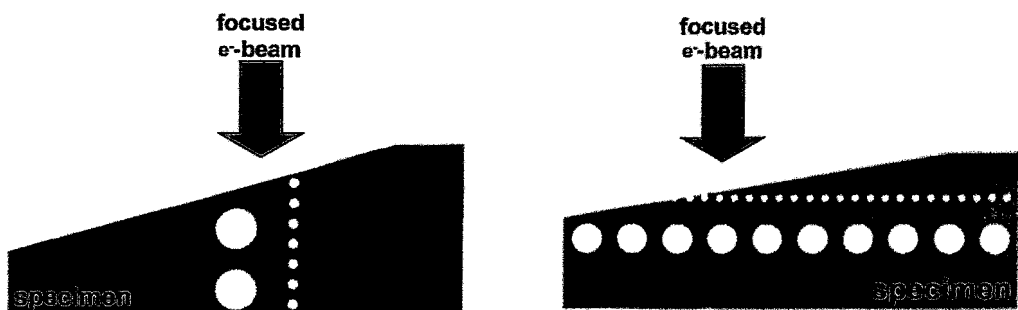

Figure 3.11: Comparison between CS (left) and PV (right) specimens in the case of SC3.

The following figures present the three SCs in as-deposited condition.
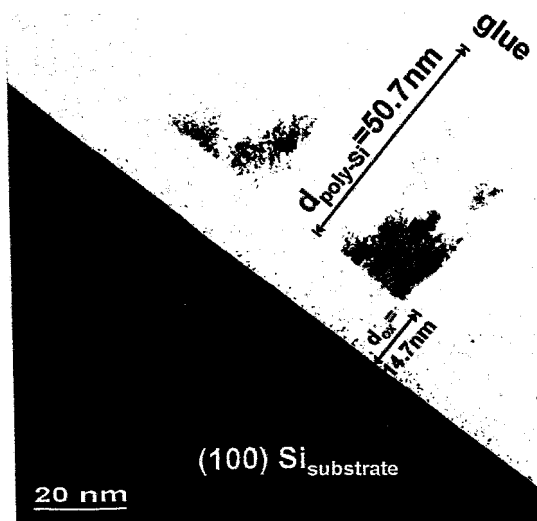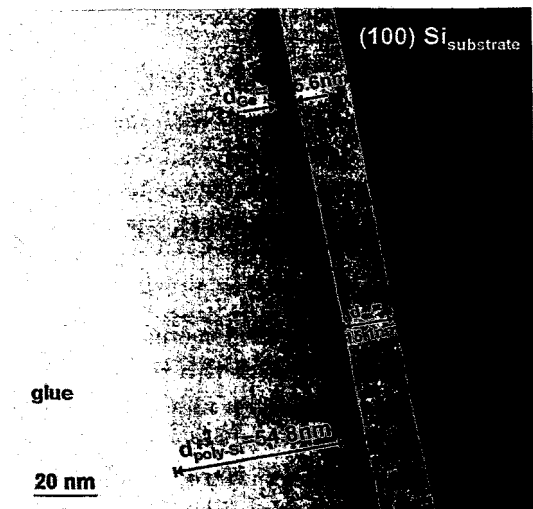
Figure 3.12:
CS TEM image of SC1.

Figure 3.13:
CS TEM image of SC2.
Note, that the label "poly-Si"
refers to a sputtered Si layer
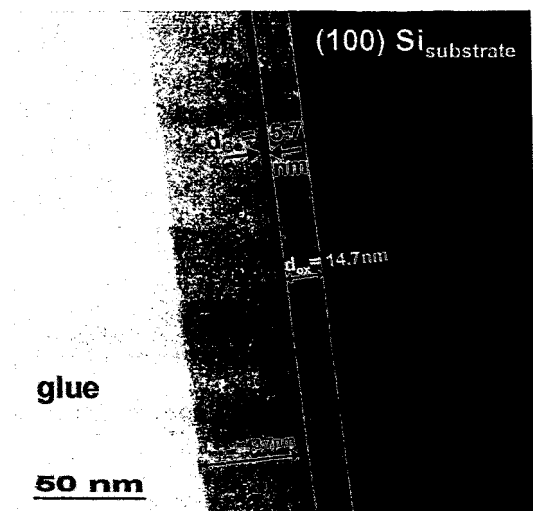which is actually amorphous after
deposition.

Figure 3.14:
CS TEM image of SC3.

3.3.2 RBS

The depth-dependent elemental composition of a sample and to a certain degree its atomic arrangement can be determined in scattering events between target atoms and high-energetic particles by observing the scattering kinematics.

A predominant method of ion beam analysis is Rutherford backscattering spectrometry (RBS) which is physically based on elastic backscattering of light and charged particles at the Coulomb potential of atomic nuclei in the target. From energy transfer and scattering angle of the projectile one is able to conclude the mass of the scatterer. The experimental arrangement of RBS is schematically depicted in fig. 3.15.
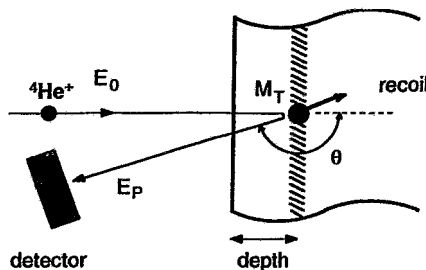

Figure 3.15: Block diagram of Rutherford backscattering in the case of normal incidence (after [SCG96]). In the performed RBS analyses, ^{4}He$^+$ ions of $E_0 = \{1.2; 1.7\}$ MeV from a Van de Graaff accelerator were used. Here, θ denotes the scattering angle. The other variables bear common meaning.

The assumption of pure Coulomb interaction between projectiles and target nuclei is only valid as far as the shielding influence of electronic shells on the scattering event is negligible. This is usually the case, thus, the Rutherford differential cross section in the center-of-mass system is applicable:

$$\frac{d\sigma}{d\Omega} = \left(\frac{Z_P Z_T e^2}{16\pi\epsilon_0 E} \right)^2 \frac{1}{\sin^4(\theta/2)} \,, \tag{3.1}$$

where Z_P and Z_T denote the atomic numbers of projectile and target atoms, respectively. The scattering event causes an energy transfer from the ^{4}He projectiles to the target atoms. Thus, the so-called kinematic factor K is defined as ratio between the projectile energy after and prior to the collision. Energy and momentum conservation allow a transcription in terms of the mass ratio $\frac{M_P}{M_T}$ and the scattering angle θ:

$$K := \frac{E_P}{E_0} = \left[\frac{\sqrt{1 - \left[\frac{M_P}{M_T} \sin\theta \right]^2} + \frac{M_P}{M_T} \cos\theta}{1 + \frac{M_P}{M_T}} \right]^2 . \tag{3.2}$$

In the case that the incoming ^{4}He$^+$ is directly scattered at the surface of the sample, it is detected with an energy $E_P = KE_0$. If the ^{4}He$^+$ projectile is scattered after

penetrating a layer of thickness x, it suffers twofold electronic energy loss on its path through the sample:

$$-\frac{dE}{dx} := -\lim_{\Delta x \to 0} \frac{\Delta E}{\Delta x} \ . \tag{3.3}$$

Here, the Bethe-Bloch formula in the non-relativistic limit is applicable since the considered particle velocities are low. Thus,

$$-\frac{dE}{dx} \propto \frac{1}{v^2} \propto \frac{1}{E} \ln E \ . \tag{3.4}$$

Fig. 3.16 demonstrates that particles, which are scattered at a depth x beneath the sample surface, leave the target with an energy $E_P(x) < KE_0$.
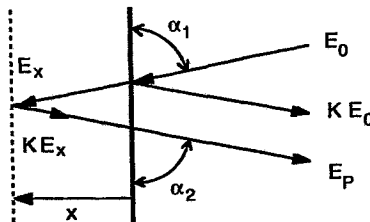
Figure 3.16: Geometry of backscattering (after [SCG96]).

The detection of this energy difference

$$\Delta E(x) = KE_0 - E_P(x) = \left[\frac{K}{\sin \alpha_1} \frac{dE}{dx} \bigg|_{E_0} + \frac{1}{\sin \alpha_2} \frac{dE}{dx} \bigg|_{KE_x} \right] x \tag{3.5}$$

allows element-specific and even isotope-specific depth profiling which is schematically addressed in fig. 3.17.

Figure 3.17: A schematic RBS spectrum is drawn for normal incidence. $H(E_P)$ increases towards smaller values of E_P since the number of backscattered particles grows with increasing depth, which coincides with higher electronic energy loss, due to $\frac{d\sigma}{d\Omega} \propto \frac{1}{E^2}$ (after [SCG96]).

The number of detected backscattered $^4\text{He}^+$ particles, i.e. the so-called RBS-yield, depends on the solid angle of the detector $\Delta\Omega$, the differential scattering cross section $\frac{d\sigma}{d\O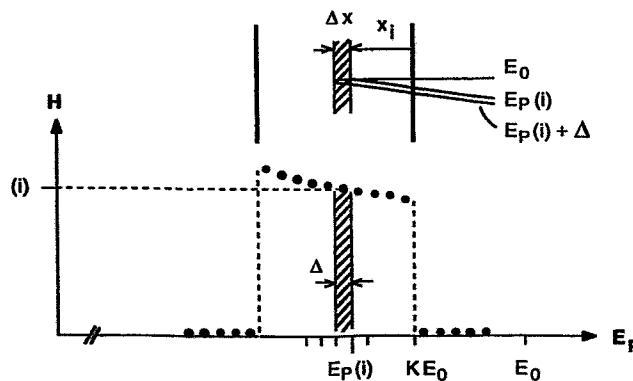mega}$, the total detected charge $I_0 t_0$, and the number of target atoms per irradiated area $N/A = n\Delta x$, where n denotes the density of target atoms in the irradiated volume V:

$$H(i) = \frac{d\sigma}{d\Omega}\bigg|_{E(x_i)} I_0 t_0 \, \Delta\Omega \, n\Delta x \, . \tag{3.6}$$

Thus, for measured H(i) one can calculate layer thicknesses by integrating $H(E_P)$ over E_P.

Figures 3.18, 3.19, and 3.20 depict the RBS spectra of the three initial SCs, i.e. in the as-deposited state. All three samples were analyzed under equal conditions: $^4\text{He}^+$ beam with $E_0 = 1.2\,\text{MeV}$, $Q_{\text{tot}} = 40\,\mu\text{C}$, $\alpha_1 = 20°$, $\alpha_2 = 170°$, and $\Delta\Omega = 1.24\,\text{msr}$. In accordance with figure 3.15, the scattering angle is $\theta = 170°$ which corresponds to K-values (after eq. 3.2) for Si and O of $K_{\text{Si}} = 0.565$ and $K_{\text{O}} = 0.363$, respectively.
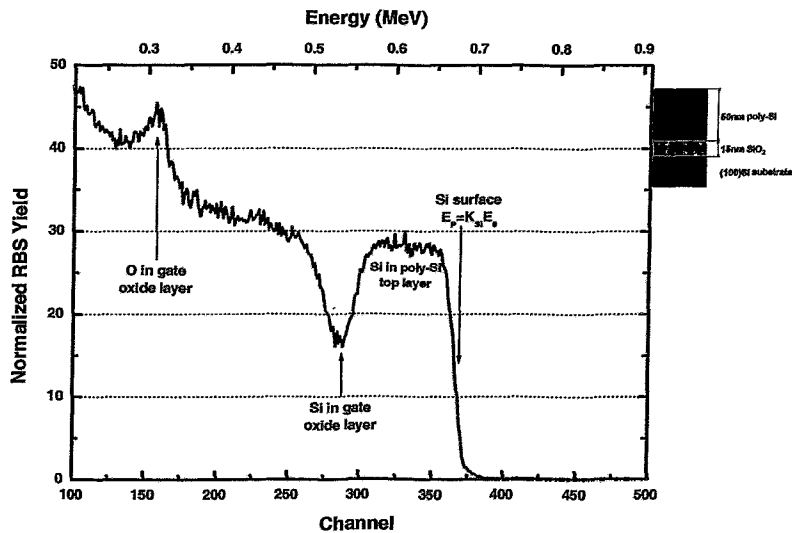

Figure 3.18: RBS spectrum of SC1 in as-deposited condition (θ=70°).
By integrating over the RBS yield, the layer thickness of the poly-Si capping layer could be determined: $d_{\text{poly-Si}}$=52.1 nm ($2.60 \cdot 10^{17}\,\text{Si/cm}^2$).

Note, that the resolution of the detector is limited: FWHM $= 14.0\,\text{keV}$. Thus, surface and interface signals do not appear as ideal step functions in contrast to the simplified illustration in fig. 3.17. Additionally, roughness limits the precision of the depth resolution at interfaces and surfaces. RBS is sensitive to the isotopical composition of the elements involved, since the scattering kinematics is determined by the mass of the scatterer. This diminishes the sharpness of the signals to a further degree which is of particular importance in the case of Ge[4]. Energy calibration, normalization of the spectra[5], and peak integration were performed with RUMP[6]. For a description of the program, the reader is referred to [DOL85, DOL86].

---

[4]Naturally occurring isotopes of germanium: Ge-70 (21.23%), Ge-72 (27.66%), Ge-73 (7.73%), Ge-74 (35.94%), and Ge-76 (7.44%).

[5]$Y_{\text{norm}} = \frac{\text{counts}}{Q \cdot \Delta\Omega \cdot (\Delta E/\text{channel})}$

[6]Rutherford Universal Manipulating Program.
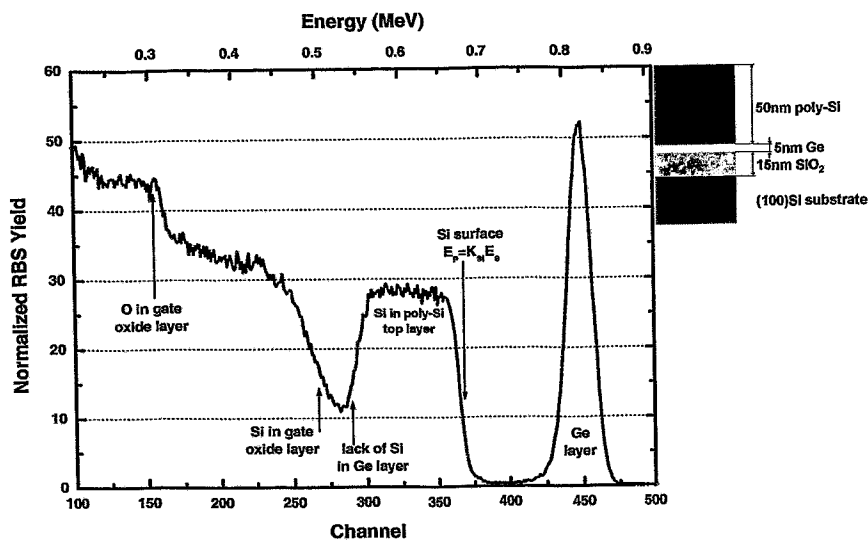
Figure 3.19: RBS spectrum of SC2 in as-deposited condition (θ=70°).
Here, $d_{\text{poly-Si}}$=50.6 nm (2.53·10^{17} Si/cm^2) and d_{Ge}=5.6 nm (2.49·10^{16} Ge/cm^2).
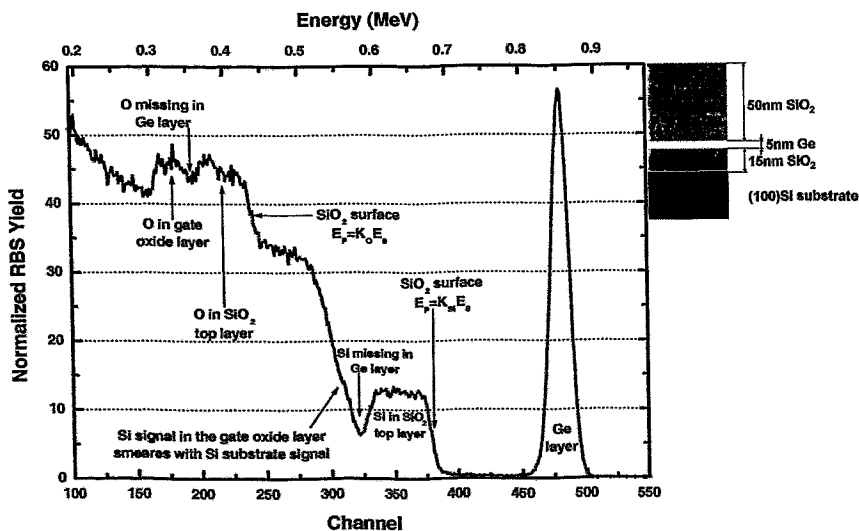

Figure 3.20: RBS spectrum of SC3 in as-deposited condition (θ=70°).
Here, d_{SiO_2}=43.4 nm (9.88·10^{16} Si/cm^2) and d_{Ge}=5.7 nm (2.51·10^{16} Ge/cm^2).

3.3.3 ToF-SIMS

The depth-dependent stoichiometric composition of the sample was obtained by ToF-SIMS measurements.

SIMS analysis is based on the impact of low energetic ions upon the sample surface which leads to a highly resolved layer-by-layer erosion of the target (see fig. 3.21).
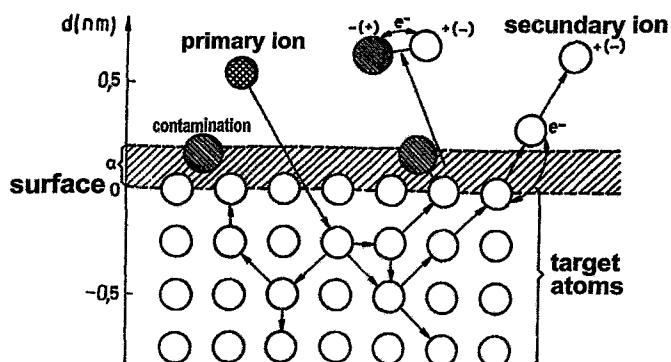

Figure 3.21: SIMS block diagram. The impact of the primary ions generates positively and negatively charged secondary ions which are sputtered from the outermost atomic layers of a surface (after [DUH99]).

In the case of ToF-SIMS, a short pulse of primary ions strikes the surface, and the secondary ions produced in the sputtering process are extracted from the sample surface into a time-of-flight mass spectrometer. These secondary ions are dispersed in time according to their velocities which are proportional to their mass-to-charge ratio. Discrete packets of ions of differing mass are detected as a function of time at the end of the flight tube.

Thus, the elemental and even isotopic concentration of the specific layer is determined with a minimum sensitivity of 10 ppm. Moreover, by focusing on signals of atomic conglomerates, atomic bonds can be revealed. This is of particular importance with regard to $Si_{n>1}^-$ or $Ge_{n>1}^-$ signals which indicate the existence of Si or Ge NCs within a SiO_2 matrix.

In cooperation with the laboratory at MDM-INFM[7] in Agrate Brianza, Italy, some of the samples considered here were analyzed with an ION-TOF CAMECA IV dual beam ToF-SIMS. Thus, two different ion species were applied for sputtering and analyzing, namely 1 keV Cs^+ and 25 keV Ga^+, respectively.

In order to avoid variations of the signal intensities, the ToF-SIMS data were normalized on the value of the $^{30}Si^-$ signal in the silicon bulk. For a depth calibration of the measurement, the SIMS diagrams were compared to high resolution TEM CS images assuming a constant sputter rate of 0.21 nm/s throughout the gate oxide layer. Details concerning the experimental setup and the dual beam method were recently published in [PEM03].

For illustration, fig. 3.22 depicts SIMS signals of SC1 in the condition prior to implantation.

---

[7]Materiali e Dispositivi per la Microelettronica - Istituto Nazionale per la Fisica della Materia, partner in "NEON".
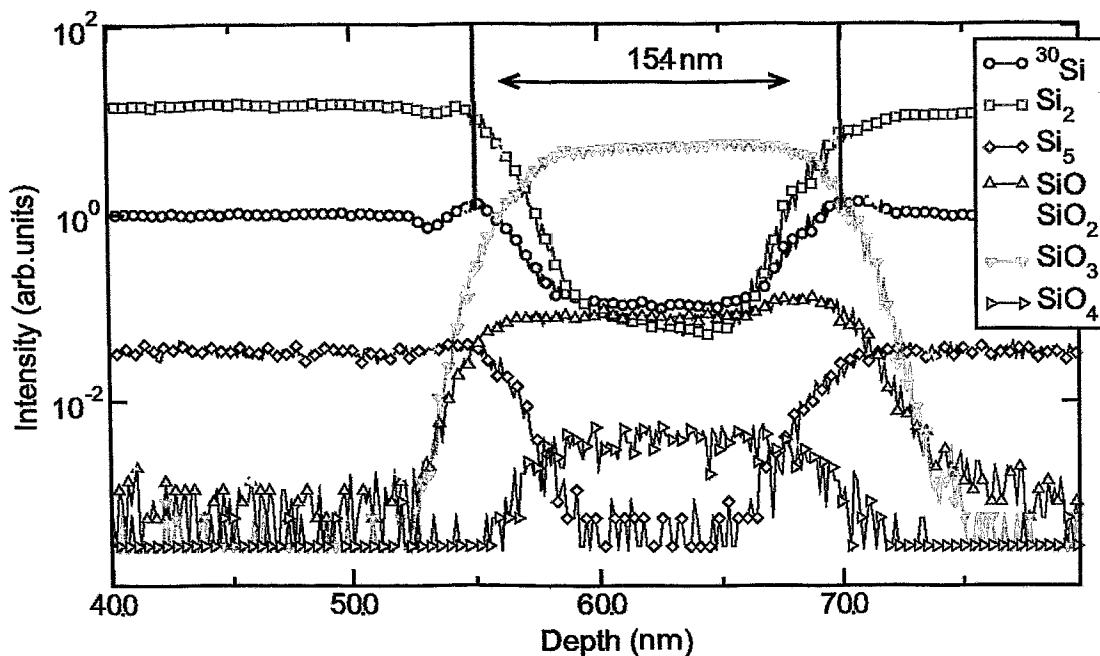
Figure 3.22: The SIMS depth-profile of SC1 prior to irradiation. At the interfaces, some signals (^{30}Si in particular) show hillocks.

Note, that the Si_2 signal is always below the ^{30}Si signal in stoichiometric SiO_2. In the SIMS profiles to come, the rise in the $Si_n (n>1)$ signals serves as indicator for the presence of excess Si in the oxide after irradiation or thermal annealing. Lokal maxima in the $Si_n (n>1)$ signals reveal the existence of Si NCs.

A general property of SIMS profiles is the decrease in depth resolution with increasing depth (see the above figure). Thus, the 50 nm thick poly-Si capping layer was chemically removed in some cases, as result of which the signals of the buried SiO_2 region appeared more accentuated.

Chapter 4

Interface Mixing vs. Conventional Implantation

The morphogenetic approach presented in this thesis is based on phase separation which originates in supersaturation of Si and Ge in a SiO_2 host matrix.

Supersaturation does not occur under thermodynamic equilibrium conditions. Thus, the system has to be forced towards non-equilibrium which is achieved by ion-solid interaction, the main consequences of which are twofold:

1. an atomic concentration of the implanted species even above the equilibrium solubility limit is obtained in the matrix and

2. atomic collisions cause a redistribution of the initial atomic set-up of the matrix.

Within the context of the sample structures presented in section 3.1, in this chapter, the discussion is focused on the physical principles of ion-solid interaction and on accompanying computer simulations in comparison with experimental results.

4.1 Physical Principles of Ion-Solid Interaction

Any target material undergoes structural modifications if it is exposed to a beam of energetic ions. Various monographs are available that deal with this topic. For a profound insight, the reader is referred to [NAM96], [RIE95], or [SMR97].

On its random path through the solid, the ion persistently looses energy until it comes to rest. Two principal physical processes are involved in decelerating the ionic projectile, namely elastic collisions with the target nuclei as well as inelastic interactions with the electron shells of the target atoms.

Thus, a stopping cross section S is defined which incorporates the energy loss per unit length (the so-called "stopping power") and the atomic density of the target:

$$S(E) = -\frac{1}{N}\left(\frac{dE}{dx}\right) = -\frac{1}{N}\left(\frac{dE}{dx}\right)_{nuclear} - \frac{1}{N}\left(\frac{dE}{dx}\right)_{electronic} = S_n(E) + S_e(E) \, . \quad (4.1)$$

Nuclear and Electronic Stopping

The sequence of nuclear collisions forms a collision cascade in the target. In every binary collision (BC), a defined amount of energy T is transferred from the incoming particle to the target atom which is assumed to be at rest, approximately. If the transferred energy exceeds a characteristic value – the displacement threshold energy E_d – the target atom is expelled from its initial site, which results in a modification of the atomic composition of the target. With regard to energy and momentum conservation, $S_n(E)$ is defined as

$$S_n(E) \equiv \int_0^{T_{\max}} T \mathrm{d}\sigma(T) \text{ , where} \tag{4.2}$$

$$T = \frac{4m_1 m_2}{(m_1 + m_2)^2} E \sin^2 \frac{\theta_c}{2} \text{ and } T_{\max} = T(\theta_c = 180°) \text{ .} \tag{4.3}$$

Here, m_1, m_2, E, and θ_c denote the masses of the particles involved in the BC, the energy of the incident particle, and the scattering angle in the CM system, respectively [NAM96].

The scattering cross section $\mathrm{d}\sigma(T)$ additionally depends on the repulsive potential V by which the particle collision is characterized. Due to shielding effects of the innermost electron shells, one generally assumes a screened Coulomb potential with regard to the distance r of the interacting atoms:

$$V(r) = \frac{Z_1 Z_2 e^2}{4\pi\epsilon_0 r} \chi\left(\frac{r}{a}\right) \text{ ,} \tag{4.4}$$

where χ and a denote the screening function and the screening length, respectively. The other variables bear common meaning.

Numerous variations of χ were developed to describe the potentials of as many projectile-target combinations as possible. Finally, a universal screening function

$$\chi_{\mathrm{uni}}(y) = 0.1818\,\mathrm{e}^{-3.2y} + 0.5099\,\mathrm{e}^{-0.9423y} + 0.2802\,\mathrm{e}^{-0.4028y} + 0.02817\,\mathrm{e}^{-0.2016y} \tag{4.5}$$

was established by Ziegler, Biersack, and Littmark, including a universal screening length

$$\frac{r}{y} = a_{\mathrm{uni}} = \frac{0.8845 a_0}{(Z_1^{0.23} + Z_2^{0.23})} \text{ ,} \tag{4.6}$$

where $a_0 = 0.053\,\mathrm{nm}$ denotes the first Bohr radius of the hydrogen atom [ZIJ00].

For convenience, reduced units for E and x were introduced:

$$\varepsilon = \frac{m_2}{m_1 + m_2} \frac{4\pi\epsilon_0 a_{\mathrm{uni}}}{Z_1 Z_2 e^2} E \quad \text{and} \quad \xi = N\pi a_{\mathrm{uni}}^2 \frac{4m_1 m_2}{(m_1 + m_2)^2} x \text{ .} \tag{4.7}$$

In the present case, Si ions with energies up to $100\,\mathrm{keV}$ were applied to targets which have Si or SiO_2 on top. The corresponding ε values range up to 2.27 in the case of a $100\,\mathrm{keV}$ Si^+ ion colliding with a Si target atom at rest. Thus, a low energy regime (after [RIE95] for all cases where $\varepsilon < 10$) is assumed here, for which an analytical fit function is available [NAM96]:

$$S_n(\varepsilon) = \left(\frac{\mathrm{d}\varepsilon}{\mathrm{d}\xi}\right)_n = \frac{0.5\ln(1 + 1.1383\varepsilon)}{\varepsilon + 0.01321\varepsilon^{0.21226} + 0.19593\sqrt{\varepsilon}} \text{ .} \tag{4.8}$$

Besides nuclear collisions, the projectile looses energy in inelastic interactions with the electron shells of the target atoms, i.e. electronic excitations or ionizations occur which are often accompanied by disintegration of chemical bonds.

For low particle energies,[1] a linear dependence between $S_e(\varepsilon)$ and the particle velocity (i.e. $\sqrt{\varepsilon}$) is assumed in accordance with Lindhard-Scharff:

$$S_e(\varepsilon) = \left(\frac{\mathrm{d}\varepsilon}{\mathrm{d}\xi}\right)_e = k\sqrt{\varepsilon} \,, \quad \text{where} \quad k = \frac{Z_1^{2/3} Z_2^{1/2} \left(1 + \frac{m_2}{m_1}\right)^{3/2}}{12.6 \left(Z_1^{2/3} + Z_2^{2/3}\right)^{3/4} m_2^{1/2}} \,. \tag{4.9}$$

In the case that Si collides with Si, $k = 0.146$.

For illustration, figure 4.1 depicts nuclear and electronic stopping powers as function of $\sqrt{\varepsilon}$. According to that, both nuclear and electronic energy losses contribute to the deceleration of the particles in the first part of the trajectory. Nuclear stopping, however, dominates the intermediate and the final part of the trajectory.
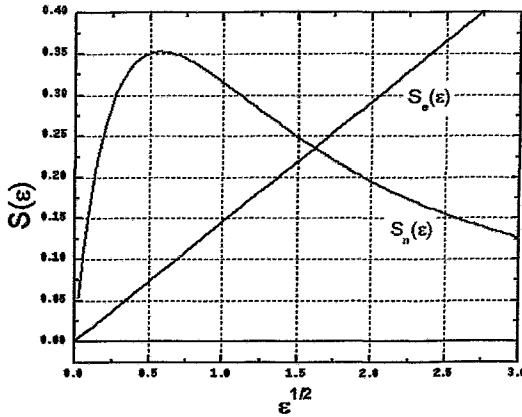

Figure 4.1: The comparison between the universal nuclear stopping cross section (red curve) and the electronic stopping cross section for Si colliding with Si (blue curve) exhibits the dominance of nuclear stopping for the energy regime and the possible projectile-atom combinations considered in this thesis. Here, $\varepsilon_{max}=2.27$, thus, $\sqrt{\varepsilon_{max}}=1.51$.

Implantation Profile

The path of a single projectile as well as its projected range, R_p, is random due to the stochastic nature of the stopping process within the collision cascade, the duration of which is approximately 10^{-13} s. The physics of the collision cascade is discussed in subsection 4.2.1 in further details.

The spatial distribution of the implanted species is usually Gaussian-like with respect to the direction x perpendicular to the sample surface ("longitudinal straggling"):

$$N(x) = \frac{\phi}{\sqrt{2\pi}\Delta R_p} \, \mathrm{e}^{-\frac{1}{2}\left(\frac{x-R_p}{\Delta R_p}\right)^2} \,, \tag{4.10}$$

where ΔR_p denotes the projected range straggling.

Radiation Damage

The collision cascade creates a nuclear damage profile, the maximum of which is slightly closer to the surface than the profile of the implanted species. Nuclear damage arises

---

[1]i.e. the projectile is significantly slower than the shell electrons: $v \ll v_0 Z_1^{2/3}$, where v_0 is the velocity in the first Bohr orbit: $v_0 = \frac{2\pi e^2}{h} = \alpha \cdot c = 2.1877 \cdot 10^6 \, \mathrm{m/s}$.

from the recoil of matrix atoms from their original position in the lattice. If T exceeds E_d, a so-called "Frenkel pair" is produced, i.e. the recoil atom comes to rest as interstitial atom elsewhere in the matrix leaving behind a vacancy at its initial site, e.g. in the case of Si:

$$Si \longrightarrow Si_{interstitial} + Si_{vacancy} . \tag{4.11}$$
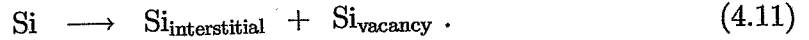
Likewise, oxygen of the SiO_2 layer can be displaced from the SiO_4 tetrahedra resulting in a SiO_x ($x<2$) suboxide:
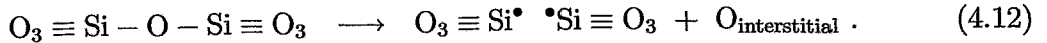
$$O_3 \equiv Si - O - Si \equiv O_3 \longrightarrow O_3 \equiv Si^\bullet \; {}^\bullet Si \equiv O_3 + O_{interstitial} . \tag{4.12}$$

Due to the forward momentum of the projectile, the distributions of interstitial atoms and vacancies do not completely coincide. Accordingly, there is a vacancy-rich region extending from the surface down to approximately $0.8R_p$ and a zone enriched with interstitial atoms between R_p and $2R_p$ for a Si target [MAA86].

Besides displacement collisions, also replacement collisions occur where the projectile takes the place of the recoiled matrix atom.

The number of displacements per atom (dpa) serves as common measure of the nuclear damage. It is proportional to the implantation fluence. As one result, crystalline semiconductors are fully amorphized when each atom of the crystal is displaced at least once, i.e. at a nuclear damage of 1 dpa at RT (see fig. 4.2). Some materials are far more sensitive to nuclear damage and are already amorphized at lower damage, e.g. crystalline quartz turns into a-SiO_2 at 0.04 dpa [HAF98].
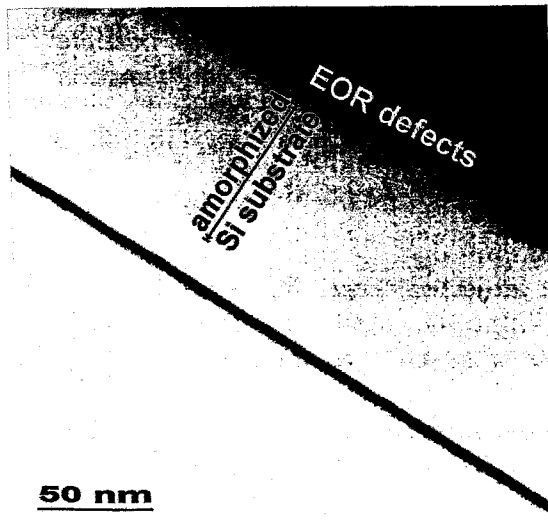
Figure 4.2: As-irradiated condition of SC3 (E_0=70 keV, ϕ=3·10^{15} Si$^+$/cm^2).

Here, the substrate is amorphized up to a depth of nearly 70 nm from the SiO_2-Si interface. Furthermore, end-of-range defects are visible.

Note the weak contrast between a-Si and a-SiO_2 which implies the non-observability of tiny a-Si NCs within a SiO_2 matrix!

Amorphization can be suppressed by elevating the temperature of the substrate (see fig. 4.3). Thus, the mobility of point defects increases significantly due to the temperature dependence of the point defect diffusion coefficient D_{pd}:

$$D_{pd} = D_{pd}^0 \exp\left(-\frac{E_a}{kT}\right) . \tag{4.13}$$

Here, E_a denotes the diffusion activation energy. Accordingly, Frenkel pairs become less stable resulting in interstitial-vacancy recombination. Therefore, the crystallinity

of the substrate can be preserved depending on the ratio between the rates of displacement and recombination. This indicates that the temperature regime during ion implantation may exert substantial influence on the dynamics of the compositional changes in the matrix.
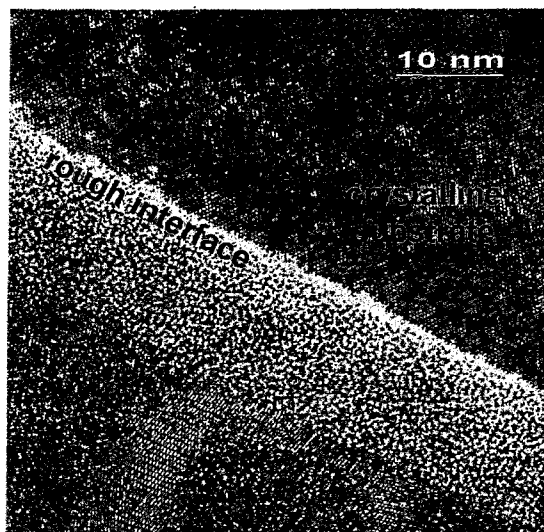

Figure 4.3: As-irradiated condition of SC1 (E_0=100 keV, ϕ=2.5·10^{16} Si$^+$/cm^2). Here, the target temperature was elevated to 400 °C in order to keep the substrate crystalline during irradiation.
Note, that the initially flat interface between oxide and substrate is roughened. Moreover, the contrast in the interface-near region of the substrate is weakened. Here, the Si lattice is disturbed on the one hand by oxygen atoms which are mixed into the substrate and on the other hand by Si substrate atoms which were recoiled from their lattice site.

Sputtering

As mentioned in subsections 3.2.2 and 3.3.3, sputtering of atoms close to the sample surface plays an important role during layer deposition and sample analysis, i.e. in magnetron sputtering and SIMS, respectively. However, the influence of sputtering on the implantation profiles and the nuclear damage, which causes the desired compositional changes in the matrix, is negligible. Nonetheless, the principles of sputtering have briefly to be mentioned here:

Due to the random nature of the nuclear collision cascade, a considerable fraction of the cascade is close to the surface of the target, particularly in the case of low projectile energies. If the energy transfer, T, is large enough to overcome the surface binding energy, E_b, an atom of the outermost atomic layers may leave the matrix if the momentum transfer points into the direction of the surface, thus leaving behind merely a vacancy.

The decisive quantity describing this phenomenon of surface erosion is the sputtering yield, Y_s, which is defined as ratio between the number of emitted atoms and the number of incident particles. Sigmund determined the dependence of Y_s on the physical parameters involved as follows [SIP69, NAM96]:

$$Y_s(E_0) \propto \frac{1}{E_b} \cdot \alpha \cdot S_n(E_0) \ . \tag{4.14}$$

Here, α denotes a function of the mass ratio (m_2/m_1) and the angle of incidence. E_b is usually equated with the heat of sublimation. Thus, for the poly-Si capping layer of SC1 and SC2, E_b(Si)=4.7 eV.[2]
The determination of Y_s for compounds like SiO$_2$, however, is rather complicated. In

---

[2]$\Delta_s H°$(Si) = 450kJ/mol [CHM98].

general, E_b, S_n, and α differ from element to element in a compound. Thus, preferential sputtering usually occurs which leads to a composition change of the surface region. Furthermore, chemical effects may influence the sputtering behavior of a surface which consists of miscellaneous atomic species.

SiO$_2$ is the only such system that needs to be considered. Here, the heat of formation of the oxide, $\Delta_f H$, as well as the enthalpy of the dissociation of molecular oxygen, ΔH^{diss}, have to be taken into account. It is not expected that oxygen is enriched at the surface because it is likely to form volatile molecules which are free to leave the sample. Thus,[3] in accordance with eqn. (17) in [MOW02]:

$$E_b(\text{Si} - \text{Si}) = 4.7 \,\text{eV} \, , \tag{4.15}$$

$$E_b(\text{O} - \text{O}) = 0 \,\text{eV} \, , \text{ and} \tag{4.16}$$

$$E_b(\text{Si} - \text{O}) = \frac{1}{2}\Delta_s H(\text{Si}) + \frac{3}{4}\Delta_f H(\text{SiO}_2) + \frac{3}{4}\Delta_{\text{diss}} H(\text{O}_2) = 13.3 \,\text{eV} \, . \tag{4.17}$$

In the present cases, the effect of sputtering on the effects of nuclear damage in the region of interest is practically inconsequential. By definition, Y_s is proportional to the total number of implanted ions and is assumed to be constant during implantation. The maximum surface erosion occurred in the cases of high ion fluences – $\phi_{\text{max}}=5\cdot10^{16}\text{Si}^+/\text{cm}^2$ – thus, causing a maximum surface erosion of 10 nm for $Y_s \approx 1$ in the case of a Si capping layer. Considering samples with a capping layer thickness of initially 50 nm, even a 20% reduction of the capping layer thickness generates merely insignificant changes in terms of nuclear stopping in the region of interest, namely at the interfaces of the buried oxide layer.

4.2 Computer Simulation

The above explained physical principles significantly improve the understanding of the various processes involved in ion implantation. However, for a quantitative description of an experiment, in which arbitrary target compositions and implantation parameters are given, this analytical apparatus is inefficient. Therefore, quantitative examinations are usually performed in computer simulations which allow to consider arbitrary beam-target combinations by predefining appropriate parameters.

In this connection, Monte Carlo simulation codes were developed, thus, implantation profiles, nuclear damage distributions, or even dynamic changes in the atomic composition of the matrix can relatively easily and rapidly be calculated.

Two computer programs served as simulative tools in the framework of the present tasks which are briefly portrayed in the following. For a comprehensive insight into this subject, the reader is referred to a monograph by Eckstein [ECW91] and the numerous references given therein.

4.2.1 TRIM

The widely used TRIM (transport of ions in matter) simulation program[4] describes the path of an incident projectile as a series of binary collisions with target atoms at rest.

---

[3] $\Delta_f H(\text{SiO}_2)$=9.44 eV, $\Delta_{\text{diss}} H(\text{O}_2)$=5.17 eV [CHM98]

[4] All TRIM simulations were performed with the TRIM98 code.

Thermal vibrations of matrix atoms around their positions are neglected. The momentum transfer in a single projectile-target collision occurs within a time frame much shorter than a period of lattice vibration at RT ($10^{-13}...10^{-12}$ s). Thus, the atoms of the matrix can legitimately be assumed to be motionless at RT.

The target atoms are quasi-randomly distributed in space which applies in a first approximation to amorphous materials, even though a short range order does always occur in reality.

The path of the ion is characterized by a constant free path length, λ, which the projectile travels between two successive collisions. Here, λ is given by the inverse cube root of the atomic density.

From a simulative point of view, the randomness is realized by a randomly generated impact parameter for each individual binary collision. From this, each nuclear collision is characterized, i.e. the nuclear energy loss as well as the polar deflection angle are calculated using the universal screening potential given by equations 4.4, 4.5, and 4.6. Thereafter, the azimuthal scattering angle is randomly determined.

Besides that, the electronic energy loss of each particle in motion is recorded on the intercollisional paths.

Consequently, positional, directional, and energetic changes of the projectile describe its path through the matrix. Moreover, all matrix atoms which are set into motion due to collisions and, thereby, participate in the collision cascade are similarly observed. Thus, the entire collision cascade is examined which comes to a standstill within the first 10^{-13} s after the ion strikes the target surface. For a profound insight into the realm of TRIM, the reader is referred to [BIJ80, ECW91, ZIJ00]. For illustration, figure 4.4 depicts the collision cascades of ten pseudoparticles for a target of SC1.
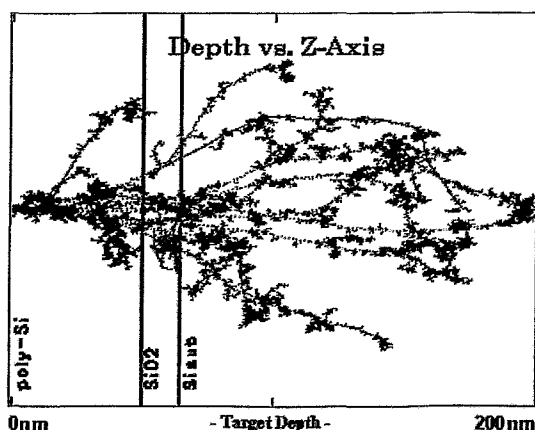

Figure 4.4: Ion and recoil trajectories for ten Si$^+$ pseudoparticles entered the target under normal incidence with E_0=100 keV (SC1).
Note, that along the projectile trajectories subcascades emerge which are caused by recoil atoms.

Prior to the simulation run, the target and projectile parameters (width and stoichiometry of the layers, atomic densities, number of pseudoparticles, initial projectile energy, and angle of incidence) have to be declared.

Furthermore, certain element specific energy parameters are predefined, namely E_d (the displacement energy above which a stable interstitial – Frenkel pair – is formed), E_s (the surface binding energy), and E_b (the bulk binding energy which is subtracted from the nuclear energy transfer T). The determination of E_b is not uniform throughout literature. Some authors ([BIJ84]) set E_b equal to zero, although E_b is generally interpreted as vacancy formation energy, i.e. as the minimum energy of an atom to leave the lattice site. In the present work, strong covalent atomic bonds are considered

(Si, Ge, SiO$_2$). Thus, E_b was set to 2 eV throughout all TRIM simulations. A further so-called "cutoff" energy, E_c, declares the termination of the particle motion through the solid. At the moment when the total particle energy becomes smaller than E_c it is assumed to have arrived at its final position. In any case, E_c needs to be smaller than E_b in order to discuss sputtering properly.

Table 4.1 presents an overview of the used parameters for the TRIM simulations conducted.

element	Si	O	Ge
E_d (eV)	15	20	15
E_b (eV)	2	2	2
E_s (eV)	4.7	(4.7)	–
layer	Si	SiO$_2$	Ge
mass density (g/cm^3)	2.32	2.28	5.35
atomic density (10^{22} at/cm^3)	4.98	6.85	4.43

Table 4.1: These are the discussed simulation parameter values for TRIM. In TRIM98, only one value for E_b can be declared, thus, no element specific distinction was possible in this respect. Therefore, E_b(Si) was used as general SBE.

The values for E_d are not to be taken literally. An average minimum energy for Frenkel pair formation of 25 eV is generally assumed. Strictly speaking, this is only valid for undisturbed matrices. In TRIM, each pseudoprojectile enters the target as if it were not modified by prior particle bombardment. This assumption is approximately applicable for very low fluences only. In the case of medium and high fluences ($\phi > 10^{15}$ Si$^+$/cm^2), however, the matrix is strongly damaged, thus, not of "virgin perfectness." Consequently, the average displacement threshold is lower due to numerous broken atomic bonds in the matrix. For this reason, even the values given above may be to high in the case of fluences greater than 10^{16} Si$^+$/cm^2. Halving E_d's results in the increase of the damage profile by a factor of two. The implantation profile, however, is not influenced by the choice of the E_d values. Nonetheless, this limits the literality of TRIM profiles to cases of low implantation fluences.

Besides implantation profiles, nuclear damage distributions were objects of major interest in the present studies. The amount of nuclear damage is related to the atomic redistribution of the target atoms, i.e. the stoichiometric "mixing" of the matrix components.

As mentioned above, the measure of choice with regard to nuclear damage is the number of displaced atoms. In TRIM, atomic displacements are defined as sum of vacancies and replacement collisions. Given the displacement distribution $d(x)$, the atomic density $n(x)$, and the ion fluence, one can determine the dpa-profile:

$$\text{dpa}(x) \propto \frac{d(x) \cdot \phi}{n(x)} \qquad (4.18)$$

For the three sample configurations, damage and implantation profiles are presented in figures 4.5, 4.6, and 4.7.
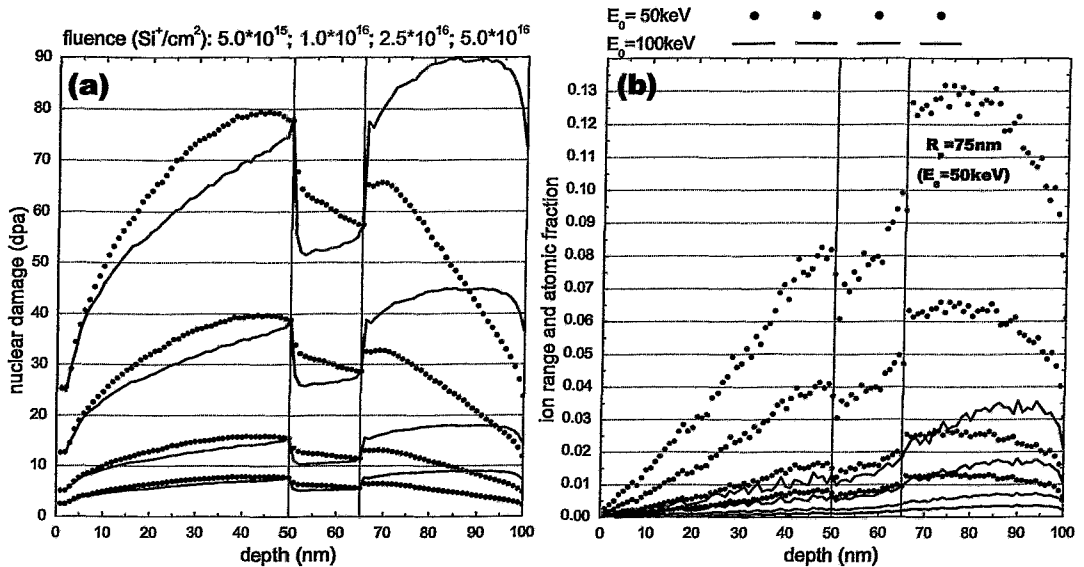
Figure 4.5: SC1 – for ion fluences up to $5 \cdot 10^{16}$ Si$^+$/cm^2, the damage profiles (a) and implantation profiles (b) are drawn for $E_0 = \{50; 100\}$ keV.
Note, that in the case of $E_0 = 50$keV the $_{\text{poly}}$Si–SiO$_2$ interface (a) suffers slightly stronger nuclear damage than the SiO$_2$–Si$_{\text{sub}}$ IF. For $E_0 = 100$keV, the damage is approximately equally strong at both IFs.
A comparison with TRIDYN results in fig. 4.8 explains the artificialness of the discontinuities at the interfaces in TRIM. The implantation profile continuously increases – even at the $_{\text{poly}}$Si–SiO$_2$ interface!

In all graphs, anomalous peaks and/or dips occur at layer interfaces. These phenomena are artificial and can be explained by the construction of the program. TRIM automatically divides the given target into 100 segments of equal width. In all simulations, a total target thickness of 100 nm was considered in order to avoid layer interfaces being situated within a segment. If the inner border of two such segments represents an interface between two target layers, the atomic density[5] undergoes a jumping discontinuity at this position. According to eqn. 4.18, jumps in dpa(x) and in the distribution of the implanted ion species, $c_{\text{ion}}(x)$, occur, too. Moreover, false damage "accounting" may occur if the ion jumps from one layer to another and the program has to decide where to register the collision data. The programmers of TRIM suggest in a stoical manner not to worry about these appearances and to average the final curves [ZIJ02].
Beside these disadvantages, one has to be aware that the bottom region of the simulated target exhibits inaccuracies, too. As soon as ions "leave" the 100 nm thick target, they are no further taken into account by TRIM. Thus, implantation profiles and damage distributions are only valid up to a depth of about 90 nm in the cases at issue. The projected range, R_p, in the cases of $E_0 = \{70; 100\}$ keV is more properly described by TRIDYN calculations which are presented in the following subsection.

---

[5]NB: The atomic density of a target segment is constant throughout the entire TRIM simulation.
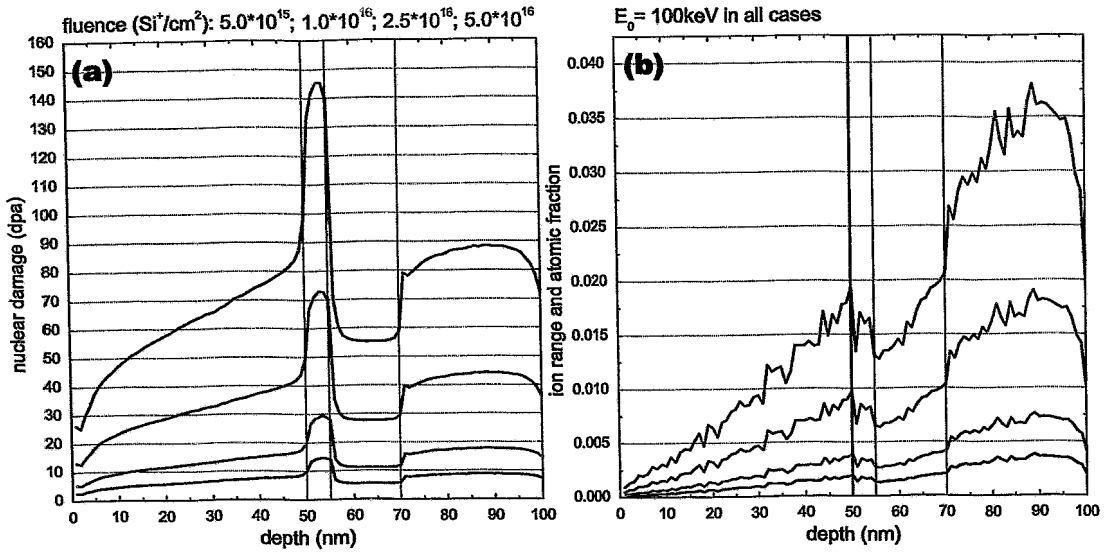
Figure 4.6: TRIM simulation for SC2. Note, that dpa(x) undergoes a siginificant rise in the Ge layer (a). This increase in nuclear damage in the thin Ge layer is attributable to the fact that $S_n^1(\varepsilon)/S_n^2(\varepsilon)=1.75$. Here, $S_n^1(\varepsilon)=S_n(\varepsilon(m_1=\text{Si},m_2=\text{Ge}))$ within Ge and $S_n^2(\varepsilon)=S_n(\varepsilon(m_1=\text{Si},m_2=\text{Si}))$ within a Si matrix. E_0 is equal in both cases.

Again, the implantation profiles (b) exhibit artefacts of discontinuity at the layer IFs.
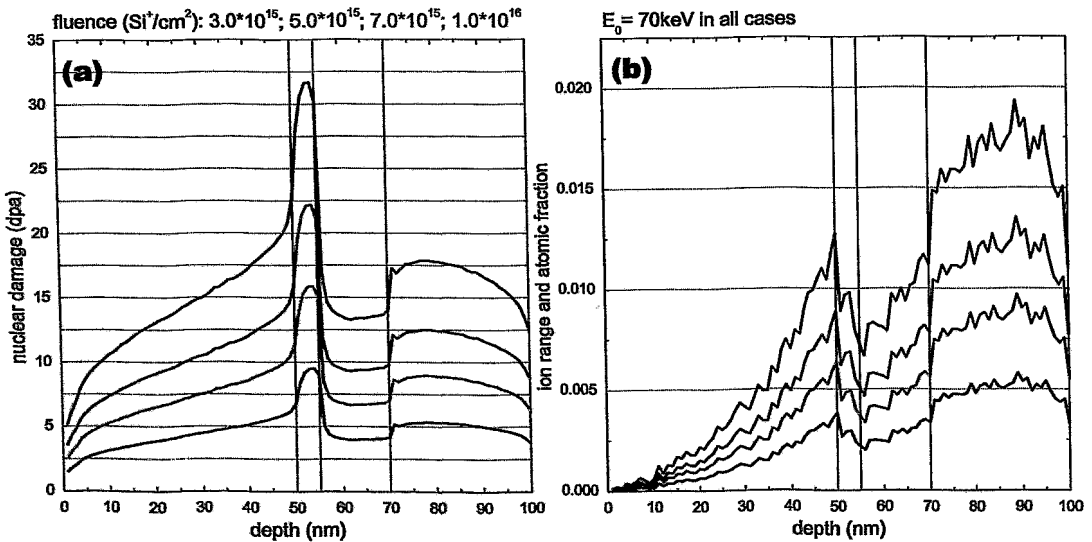

Figure 4.7: These TRIM profiles of SC3 are very similar to those in fig. 4.6.

Here, lower fluences were chosen in order to significantly reduce the damage at the IFs. During the course of the three experimental runs, which were performed one after the other, it became apparent that damage values of 30 dpa and above may be too high for achieving the desired structural effects during phase separation.

4.2.2 Advanced Simulation - TRIDYN

Given the above considerations, it becomes obvious that TRIM profiles merely reflect the truth in a first approximation. Therefore, a more sophisticated simulative approach is required in order to include target modifications which occur during implantation. For this purpose, a TRIM-like Monte Carlo code was developed by Möller and Eckstein in the 1980s – TRIDYN [MOW84, MOW85, MOW88]. The nuclear collision cascade is simulated like in TRIM based on a BC approximation. TRIDYN, however, takes dynamical changes of the atomic composition into account, i.e. stoichiometric modifications which occur during ion implantation are considered. Thus, fluence-dependent atomic redistributions of multicomponent substances ("mixing"), preferential sputtering, high-fluence implantations, and even thin film deposition can be studied.

Prior to the simulation run, all relevant parameters (initial structure and atomic composition of the target, energy values, beam parameters) had to be declared which are summarized in table 4.2. In addition, TRIDYN allows to define element and even compound specific SBE's. Different from TRIM, in TRIDYN each pseudoprojectile[6], each deposited or relocated, or sputtered atom is correlated to an infinitesimal increase or decrease in areal density. Thus, implantation fluence is a decisive parameter.

Moreover, TRIDYN allows to set the number of equal depth intervals in which the considered target is initially divided. Throughout all TRIDYN simulations, the depth intervals were chosen to be 0.5 nm in thickness. Thus, a target with a total thicknesses of 250 nm could be simulated.

element	Si	O	Ge
E_d (eV)	15	20	15
E_b (eV)	0	0	0
SBE (eV)			
Si	4.7	13.3	4.3
O	13.3	0	10.3
Ge	4.3	10.3	3.88
$E_{\text{cut-off}}$ (eV)	3	3	3
atomic density $(10^{22} \text{ at/cm}^3)$	4.98	8.47	4.43

Table 4.2: These are the TRIDYN parameter values of the target components discussed here. The values of the SBE matrix were calculated in accordance with formulae 13, 14, 16, and 17 in [MOW02]. Likewise, the atomic density of oxygen (in SiO_2) was determined with formula 21 ibid.

Again, the E_d values may be to high in the case of high implantation fluences due to a heavily disturbed matrix [MOW03p]. In a trial TRIDYN run, halving E_d's ($E_d'(Si)$=8 eV, $E_d'(Ge)$=8 eV, $E_d'(O)$=10 eV) resulted only in marginal changes in the atomic composition distributions.

---

[6]The total number of pseudoprojectile was N_{pp}=10^5 throughout all simulation runs.

The simulation of a single pseudoparticle history proceeds in two major steps:

1. calculation of the collision cascade with all usual effects discussed above (implantation, sputtering, relocation) and

2. relaxation of the depth intervals taking unchanging atomic volumes into account which results in thickness variations of the intervals.

After each run, the new areal densities are determined for all components. Thereby, the atomic composition of the target is modified pseudoparticle by pseudoparticle. Figure 4.8 impressively demonstrates that the target composition undergoes compositional changes with increasing implantation fluence. Here, SC1 serves as example that the buried SiO_2 layer is shifted towards the surface of the target due to surface erosion. Moreover, the composition of the oxide region is drastically changed with increasing fluence – from Si_1O_2 in the preimplantaion condition to Si_1O_1 at $\phi=5\cdot10^{16}\,Si^+/cm^2$! Nuclear collisions result in oxygen being displaced into the poly-Si capping layer and the Si substrate as well as Si being displaced into the oxide, respectively.
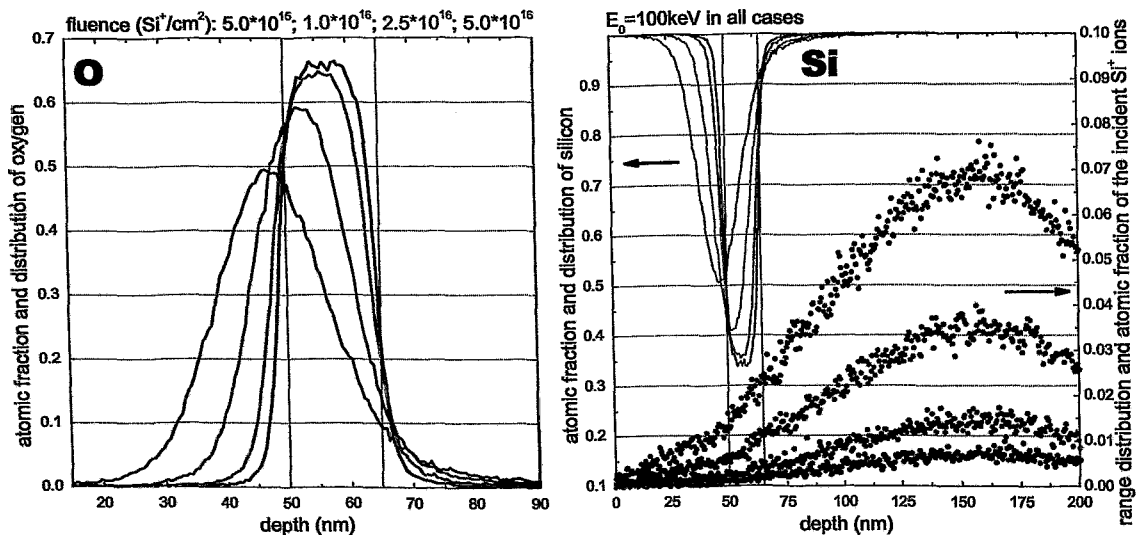

Figure 4.8: Target atom distributions and implantation profiles of SC1 for $E_0=100\,keV$. Note, that the principal share of the implanted silicon comes to rest far behind the oxide. Therefore and because of surface erosion, the oxygen distribution is shifted towards the surface. Moreover, the oxygen distribution is significantly widened which is attributable to ion mixing of both IFs, the strength of which scales with increasing fluence.

The smearing or broadening of initially sharp interfaces is not fully isotropic in the direction parallel to the ion beam which can clearly be seen in the shape of the oxygen curves. This phenomenon is caused by two effects: Firstly, nuclear mixing takes place within the collision cascade which is supposed to be isotropic. Secondly, primary collisions of rather high-energetic projectiles with target atoms lead to a momentum

transfer preferentially into the direction of the ion beam. Thus, the relocation profiles exhibit a small but noticeable asymmetry.

Furthermore, figure 4.8 exhibits one of the most important features of the present work, namely the "irradiation" of the buried oxide. In conventional IBS, the implanted species is directly implanted into the region where supersaturation is desired. Here, on the contrary, the implanted species is implanted far beyond the actual region of interest. The lion's share of implanted silicon is deposited behind the oxide layer – merely resulting in substrate swelling. Only a tiny fraction of the implanted silicon comes to rest within the oxide layer itself. Supersaturation of Si in the oxide mainly originates in collisional displacements of Si from the substrate and from the poly-Si capping layer into the oxide. Similarly, oxygen vacancies are generated in the oxide which can be interpreted as excess of silicon, too.

Likewise, figures 4.9 and 4.10 portray the ion beam induced interface broadening and the related compositional changes in the cases of SC2 and SC3.

The effect of interface mixing deserves closer examination which is performed in the following section.
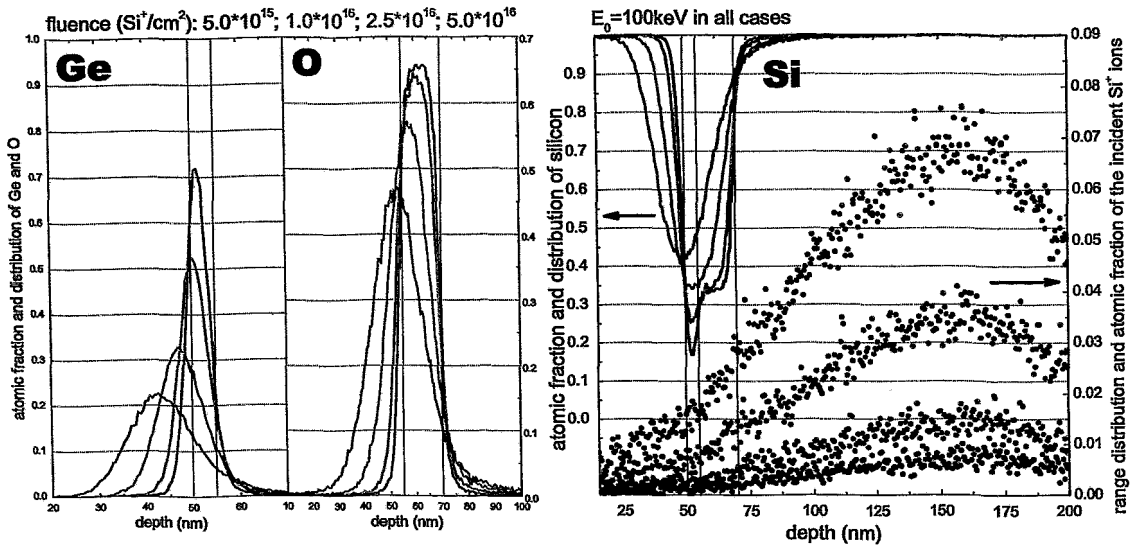
Figure 4.9: Target atom distributions and implantation profiles of SC2 for E_0=100 keV. Again, most of the implanted Si comes to rest far behind the oxide. With regard to the initial layer thickness, the germanium distribution is stronger widened than the oxygen distribution. This is in coherence with the model of a "marker layer" (see section 4.3).
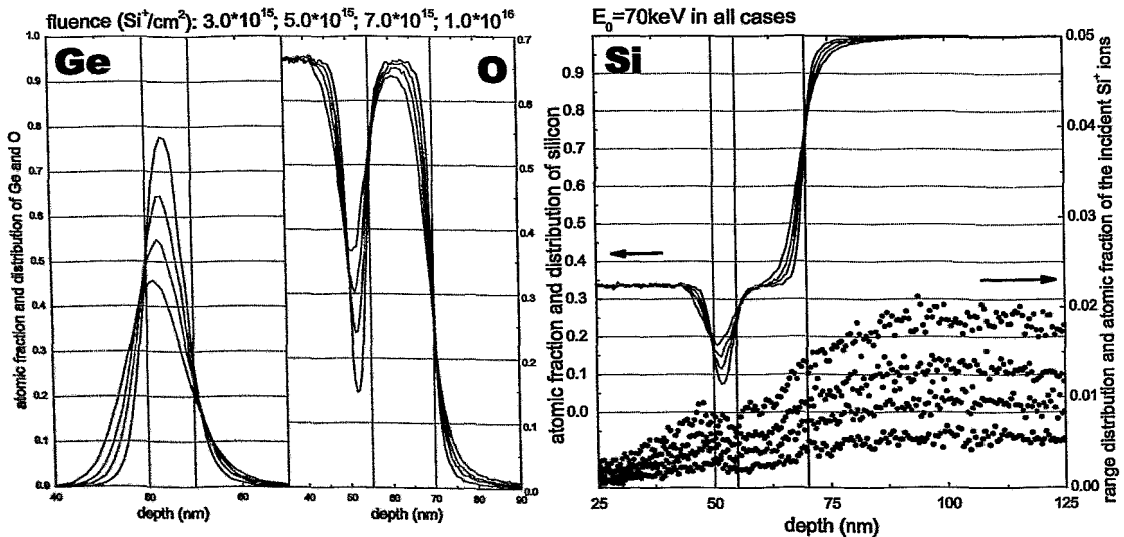

Figure 4.10: Target atom distributions and implantation profiles of SC3 for E_0=70 keV. Note, that R_p is closer to the surface ($R_p \approx 105$ nm). However, c_{ion} does not exceed 1.5% in the region of interest.
Here, the capping layer consists of SiO_2 in order to symmetrically surround the Ge layer by oxide.

4.2.3 Summary of Simulation Results

For clarity, a summary of the TRIM and TRIDYN outcomes is presented in table 4.3.

target config.	E_0 (keV)	ϕ (10^{16} Si$^+$/cm^2)	dpa at oxide IFs left	right	R_p(nm)	c_{ion}(at R_p)
1	50	0.5	7	6	80	0.012
		1.0	14	12.5	81	0.024
		2.0	22	24	82	0.046
1	100	0.5	6.5	7	155	0.007
		1.0	13	13.5	156.5	0.014
		2.5*	33	34	159	0.035
		5.0*	65	67	163	0.069
2	100	0.5	10	7	157	0.007
		1.0	21	13.5	158	0.015
		2.5	50	35	159	0.035
		5.0	105	69	160	0.070
3	70	0.3	6.5	4.5	106.1	0.006
		0.5	11.5	8	105.8	0.009
		0.7	16	11	105.7	0.0135
		1.0	22.5	16	105.6	0.0185

Table 4.3: Overview of the nuclear damage at the oxide interfaces (results of TRIM), ion ranges as well as peak fractions (results of TRIDYN). The red-colored numbers correspond to experiments which were performed in the frame of this thesis whereas the blue-colored data correspond to experiments which were conducted within NEON (part of the GROWTH Project of the European Commission) and which serve as comparison of experimental results.
The green stars mark the experiments in which the target was heated during implantation. In both cases, T$_{implantation}$={400; 600}°C.

4.3 Ion Mixing of Interfaces

The previous section indicated that ion mixing of interfaces leads to a significant change in the stoichiometry of irradiated target layers. By irradiation of interfaces and/or thin marker layers, materials with higher solute concentrations can be produced at lower fluences than in conventional high-dose implantation: in the present case, Si- and Ge-rich SiO$_2$ and O-rich Si, respectively.
Now, a deeper insight into the physical concepts of ion mixing is given in relation to the experimental as well as simulative features of the present work.

4.3.1 Mixing Regimes

Ion mixing originates in nuclear collisions between ions and target atoms. Two fundamental regimes of ion mixing have been revealed during the last three decades. These

are decisively determined by the temperature of the target during ion irradiation and by the target materials [NAM96] which is schematically drawn in fig. 4.11.
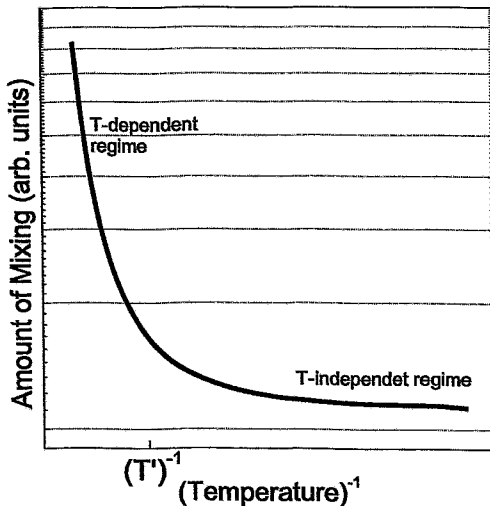

Figure 4.11: Mixing efficiency vs. temperature. The critical temperature T', which corresponds to the largest curvature of the graph, separates the *T-dependent* from the *T-independent* ion mixing regime. The illustration (after [NAM96]) points out that the amount of mixing is strongly biased by the temperature of the target if $T > T'$.

From a thermodynamic point of view, the mixing process is characterized by the heat of mixing, ΔH_{mix}. For a negative ΔH_{mix}, ion mixing is clearly enhanced. This behavior has mainly been observed in the formation of various metal alloys. In the case of silicide formation, T' was found to be between 0°C and $\sim$100°C [MAJ81, NAM96].

The case of Si-SiO$_2$, however, has not been discussed in this context, yet. It does not seem reasonable to consider a metastable Si-rich SiO$_2$ or an O-rich Si in the context of metallurgically distinct phases. From an experimental perspective, the target temperature did not exceed 100°C (see subsection 3.2.3), with the exception of some cases of SC1 (here, $T = \{400; 600\}$°C). In anticipation of the discussion of phase separation, it is worth mentioning that migration of Si in SiO$_2$ as well as of O in Si is not expected to a noticeable degree in the temperature regime up to 600°C. This is due to low solubilities and low diffusion coefficients of these species in the corresponding host matrices.

Therefore, one may consider the mixing processes described here to be independent of target temperature. They are predominantly characterized by dynamic collision processes, i.e. cascade and recoil mixing.

4.3.2 Ballistic Mixing

The above presented TRIDYN profiles indicate that the broadening of irradiated interfaces increases with increasing ion fluence, ϕ. Interface broadening is obviously governed by nuclear collisions, thus, a dependence on the ion mass m_1 (S_n increases with m_1) can be stated. Throughout all experiments and simulations, only Si$^+$ ion were used. Thus, only the dependence on the ion fluence, ϕ, needs to be discussed here.

Two principal displacement mechanisms characterize the ballistic ion mixing process:

Recoil Mixing. The smaller the impact parameter, b, in a nuclear collision the larger is the momentum transfer in forward direction. The maximum possible energy transfer can be achieved if $m_1 = m_2$, i.e. in the present cases, if Si$^+$ ions collide with Si target atoms at rest. Thus, in the case of high-energy "head-on"

(i.e. b=0) collisions, displaced target atoms may travel long distances and come to rest far away from their initial lattice site ($\vec{r'} = \vec{r_0} + \Delta\vec{r}$). This explains the asymmetry in the mixing profiles in favor of the direction of the incident particles (see e.g. silicon and oxygen distributions in fig. 4.13).

However, cases in which $b > 0$ are far more probable. Consequently, less energy is transferred, the trajectory of the recoil atom is shorter and does not point in forward direction.

Reasonably, the number of such single-recoil "long-range displacements", $\tilde{N}$, linearly depends on the number of incoming projectiles, thus, on the ion fluence: $\tilde{N} \propto \phi$ [MOW85].

Cascade Mixing. Cascade mixing occurs if an displaced target atom (a so-called primary recoil atom) knocks on other target atoms. Thus, secondary recoil atoms are produced which may continue knocking on other target atoms producing tertiary and quaternary recoils and so on an so forth. This chain of multiple displacements is a *collision cascade* (compare fig. 4.4). The atoms participating in the cascade experience numerous displacements and relocations in the low-energy regime, thus, cascade mixing is commonly entitled "short-range mixing." These events are isotropic in space. After a few collisions, the momentum of the incident projectile is statistically distributed over all directions due to the random nature of nuclear stopping. Thus, one can consider the atomic redistribution in the target as random-walk process of "pseudo-diffusion" character [MAJ81], the effective diffusion coefficient, $\tilde{D}$, of which is proportional to the ion fluence: $\tilde{D} \propto \phi$.

The above characteristics indicate that cascade mixing dominates, whereas recoil mixing is of minor importance. Therefore and because of the diffusion-like nature of cascade mixing, one can describe the broadening of a concentration depth profile $c(x, \phi)$,[7] which represents for ϕ=0 an initially sharp interface at x_0, by an error function:

$$c(x, \phi) = \frac{1}{2} \operatorname{erf}\left[\frac{x - x_0}{\xi(\phi)}\right] + \frac{1}{2} \ . \tag{4.19}$$

$\xi^2(\phi)$ corresponds to the width of the interface at position x_0 [NAM94]:

$$\xi^2 = 4\tilde{D}(\phi)t \ . \tag{4.20}$$

Since $\frac{\mathrm{d}}{\mathrm{d}x}\operatorname{erf}(x)$ results in a Gaussian distribution, ξ^2 can be related to σ^2 (see fig. 4.12):

$$\frac{\mathrm{d}}{\mathrm{d}x}\left(\frac{1}{2}\operatorname{erf}\left[\frac{x - x_0}{\xi}\right] + \frac{1}{2}\right) = \frac{1}{\sqrt{2\pi}\sigma} \exp\left[-\frac{(x - x_0)^2}{2\sigma^2}\right] \ , \ \text{with} \ \ \xi^2 = 2\sigma^2 \ . \tag{4.21}$$

In the case that only cascade mixing is considered, the broadening of an interface can be described by [BOW94]

$$\Delta\sigma^2(\phi) = \sigma^2(\phi) - \sigma_0^2 \ , \tag{4.22}$$
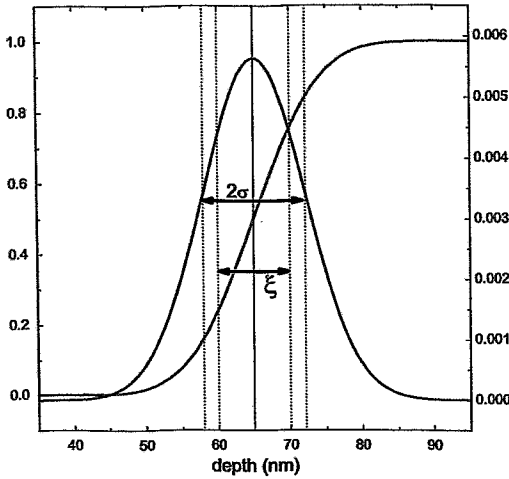
with

---

[7] $c_{\max}$=1

Figure 4.12: Error function describing the broadening of an interface (here at $x_{IF}=65\,\mathrm{nm}$). Its first derivative is a Gaussian with $\sigma = \xi/\sqrt{2}$, which is also displayed.

$$\frac{\xi^2}{2} = \sigma^2 = 2\tilde{D}t \propto \phi \,. \tag{4.23}$$

From an experimental point of view, σ_0^2 is always greater than zero because of omnipresent device functions (depth resolution, detector resolution etc.) Thus, in any spectrum – be it an outcome of RBS or SIMS – interfaces always appear smeared, even those which are sharp in a theoretical assumption.

4.3.3 Interface Broadening in TRIDYN

The present target structures are characterized by a 15 nm buried SiO_2 layer which is surrounded by the Si substrate on the one and a Si or Ge layer on the other side. Thus, two neighboring oxide interfaces (labelled with "left" and "right") have to be considered, the mixing strengths of which are favorably described by the broadening of the oxygen distribution $c_O(x)$. Thus, oxygen serves as "marker element" – just as Ge in SC2 and SC3, additionally.

In accordance with eq. 4.19, a superposition of two error functions expresses the present case:

$$c_O(x) = \frac{1}{2} \left(\mathrm{erf} \left[\frac{x - x_{\mathrm{left}}}{\xi_{\mathrm{left}}} \right] - \mathrm{erf} \left[\frac{x - x_{\mathrm{right}}}{\xi_{\mathrm{right}}} \right] \right) \,, \tag{4.24}$$

where x_{left} and x_{right} denote the centers of the error functions, the widths of which are denoted by ξ_{left} and ξ_{right}.

Due to sputtering, the center of $c_O(x)$ is shifted towards the surface (compare fig. 4.8). For the sake of simplicity, only SC1 is considered here.

It is known from the implantation profiles that the principal amount of implanted silicon comes to rest behind the oxide. Thus, swelling occurs mainly in the substrate. Therefore, sputtering and swelling are processes which shift the TRIDYN depth scale in the region of the oxide linearly. Thus, a more evident illustration of the dependence of interface broadening on ion fluence can be achieved by shifting the oxygen profiles of fig. 4.8 in a manner that the centers of all distributions coincide at equal depth (see fig. 4.13).
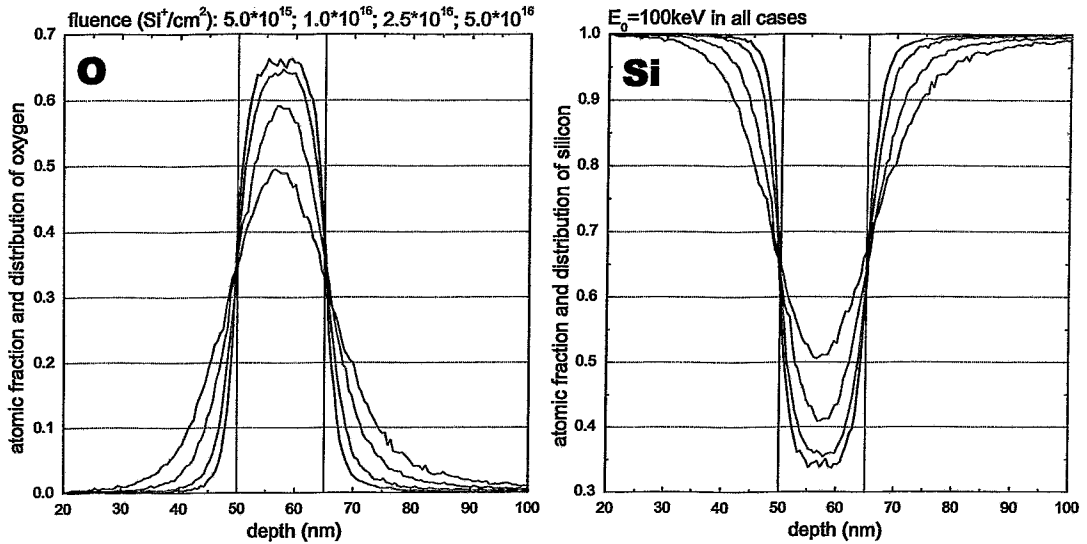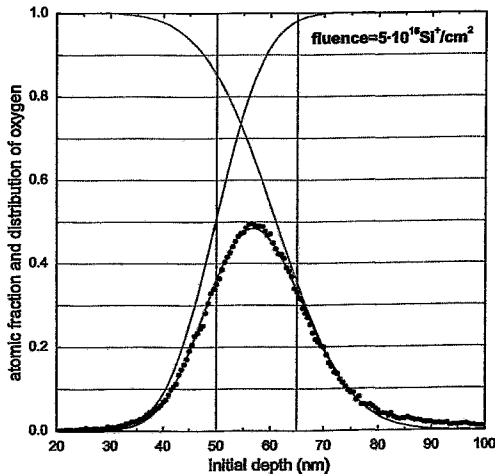
Figure 4.13: TRIDYN results for SC1. Oxygen and silicon distributions of fig. 4.8 are shifted so that the position of the centers of $c_O(x, \phi_i)$ and $c_{Si}(x, \phi_i)$ coincide for all ϕ_i. Note, that in the case of $c_O(x)$ all graphs cross at a point which represents the position of the initial interfaces at $c_O(x = x_{left} = x_{right}, \phi_i) = \frac{1}{2}c_O(SiO_2) = 0.33$. Accordingly, $c_{Si}(x = x_{left} = x_{right}, \phi_i) = 1 - \frac{1}{2}c_O(SiO_2) = 0.66$.

These graphs can be fitted by means of eq. 4.24 which is illustratively done in the case of $\phi = 5 \cdot 10^{16}$ Si$^+$/cm^2 in fig. 4.14. This fitting procedure was performed for all fluences displayed in fig. 4.13, the results of which are presented in the adjacent table.

fluence (10^{16} Si$^+$/cm^2)	ξ_{left} (nm)	ξ_{right} (nm)
0.5	6.5	6.9
1.0	7.0	7.7
2.5	8.4	10.1
5.0	11.0	15.1

Figure 4.14: According to eq. 4.24, the green fit function consists additively of two error functions. These are individually drawn in red and blue. Note the asymmetry between the two interfaces. Recoil displacements create the long-range tail in the oxygen distribution in the substrate. In accordance with theory, the IF widths, related to ξ_{left} and ξ_{right}, increase with increasing fluence as the tabled fitting results indicate.

4.3.4 Experimental Evidence

Only results of computer simulations have been presented so far. The outcomes of RBS and SIMS confirm the concept of ion mixing of interfaces to a further degree.

For example, fig. 4.15 demonstrates the mixing of the 5 nm Ge layer of SC2. Note, that the RBS-signal of the as-deposited Ge layer is naturally smeared due to various effects such as limited detector resolution, energy straggling of the He^+ beam penetrating through the Si capping layer, the isotopic abundance of Ge, and even layer roughness. In order to avoid disorientation, it is advantageous to remember that RBS spectra and TRIDYN profiles are mirror symmetric to each other, i.e. the SiO_2-$Si_{substrate}$ interface is here on the left-hand side.
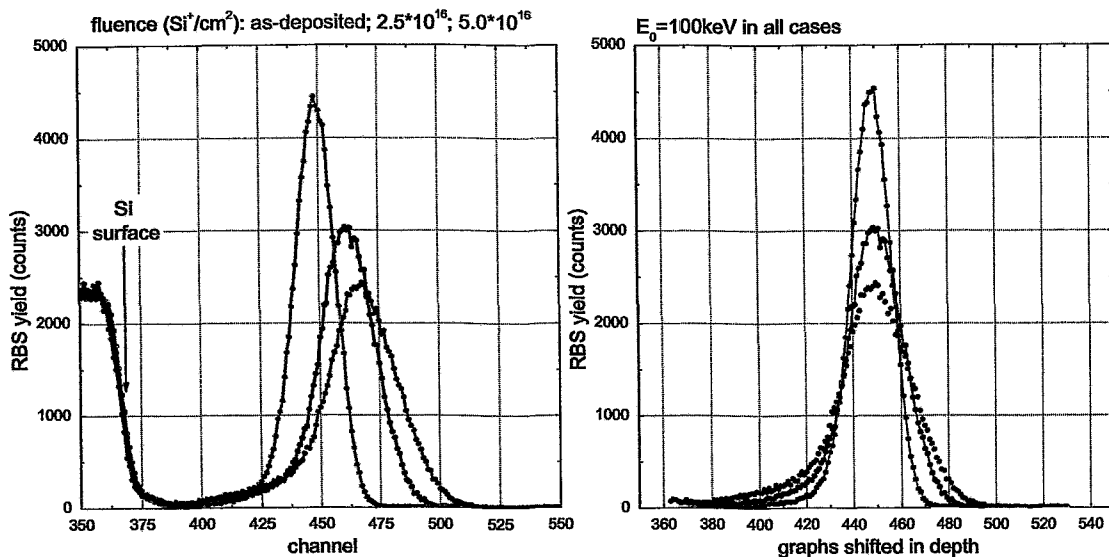

Figure 4.15: RBS spectra of SC2. The left illustration demonstrates the fluence-dependent shift of a buried Ge layer towards the surface which is due to surface erosion. Note, that the Si surface peaks coincide. By aligning the centers of the distributions (right hand side), the interface mixing of the marker layer is verified. Even the recoil-tail of Ge atoms can be identified (compare table 4.4).

If one assumes that the channel number linearly corresponds to depth, Ge is noticeably mixed about 15 nm deep into the oxide. The initial layer width is approximately 20 channels, whereas the substrate-oriented tail of the distribution is about 60 channels in length.

fluence (10^{16} Si^+/cm^2)	ξ_{left} (ch. no.)	ξ_{right} (ch. no.)
0.0	10.0	7.7
2.5	16.7	13.3
5.0	23.1	17.6

Table 4.4: Interface broadening in dependence on ion fluence. These ξ-values correspond to the RBS spectra presented in fig. 4.15. A fit function similar to eq. 4.24 was applied. The detector channel number served as depth scale. The RBS yield of 5000 was normalized to one.

Similar outcomes are found in the case of Si (see fig. 4.16). However, this discussion is limited to a qualitative analysis since the dip of the Si signal embodies the broadening of the oxygen distribution and the Ge distribution. Moreover, this RBS signal originates from a buried structure 50 nm beneath the sample surface. Thus, the depth resolution is significantly reduced which prevents a reasonable quantitative analysis.
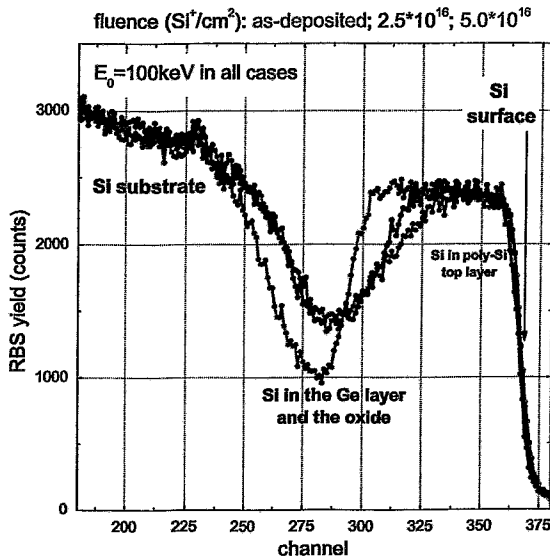

Figure 4.16: RBS spectra of SC2. The signals are drawn for the regions in the spectra which refer to silicon.
Sputtering leads to surface erosion. Thus, the dip in the Si signal is shifted towards the surface with increasing fluence.
Simultaneously, the dip width increases due to ion mixing.

The case of oxygen is even worse since the weak oxygen signal (compare fig. 3.19) overlaps with the predominant Si signal, thus, any RBS-analysis concerning the broadening of the oxygen signal is avoided here.

ToF-SIMS delivers a coherent picture of ion induced interface broadening which is shown in fig. 4.17 for the case of SC1.
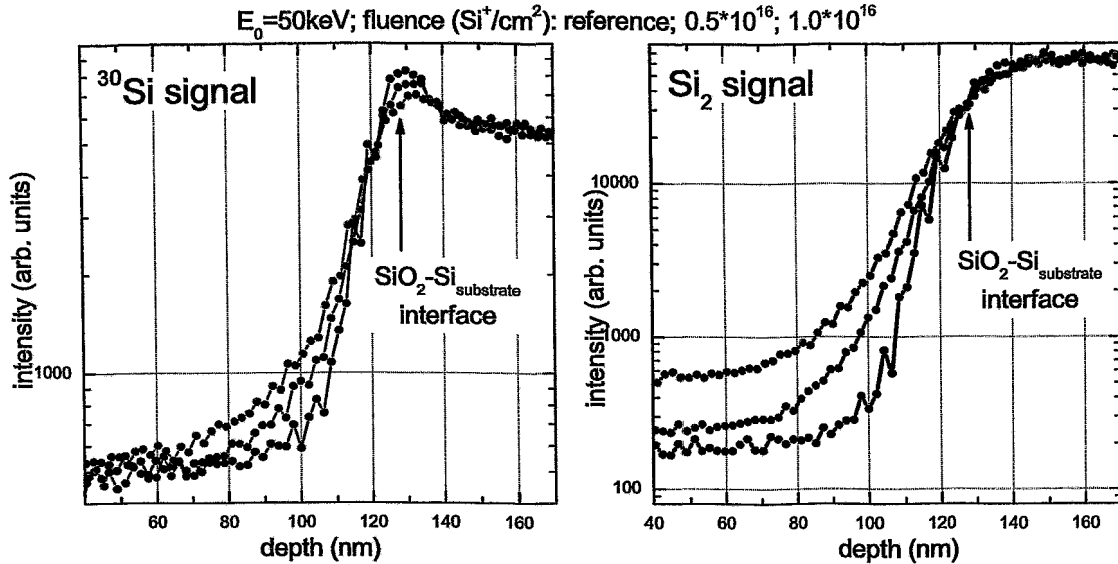

Figure 4.17: ToF-SIMS signals of SC1. Both ^{30}Si and Si_2 signals confirm excess of Si in the oxide layer after ion irradiation. For reasons of depth resolution, the capping poly-Si has chemically been removed. Thus, the broadening effect is examined only at the SiO_2-$Si_{substrate}$ interface.

4.3.5   Advantage over Common Low Energy Ion Implantation

The above results have simulatively as well as experimentally proved that ion mixing of a Si-SiO$_2$ interface generates atomic displacements and relocations between the two layers. Accordingly, displaced silicon as well as oxygen constitue the excess of Si in the oxide as interstitials and vacancies, respectively. Thus, atomic concentrations far beyond the bulk solubility limit of Si in SiO$_2$ are achievable.

The TRIDYN distributions of Si and O after irradiation quantify the excess of Si by

$$c_{Si,excess}(x) = c_{Si}(x) - 0.5 \cdot c_O(x) \ . \tag{4.25}$$

For illustration, $c_{Si,excess}(x)$ for the three SCs are drawn in figs. 4.18.1-3.

In comparison, common low energy ion implantation into a 15 nm thin oxide layer also generates supersaturation of Si in SiO$_2$. This approach, however, faces severe difficulties:

- Direct implantation into a 15 nm thin oxide results in a rather broad Gaussian implantation profile in the SiO$_2$ matrix. Locating the maximum of the profile at a distance of precisely 3 nm (in order to allow direct quantum mechanical tunnelling) is very complicated.
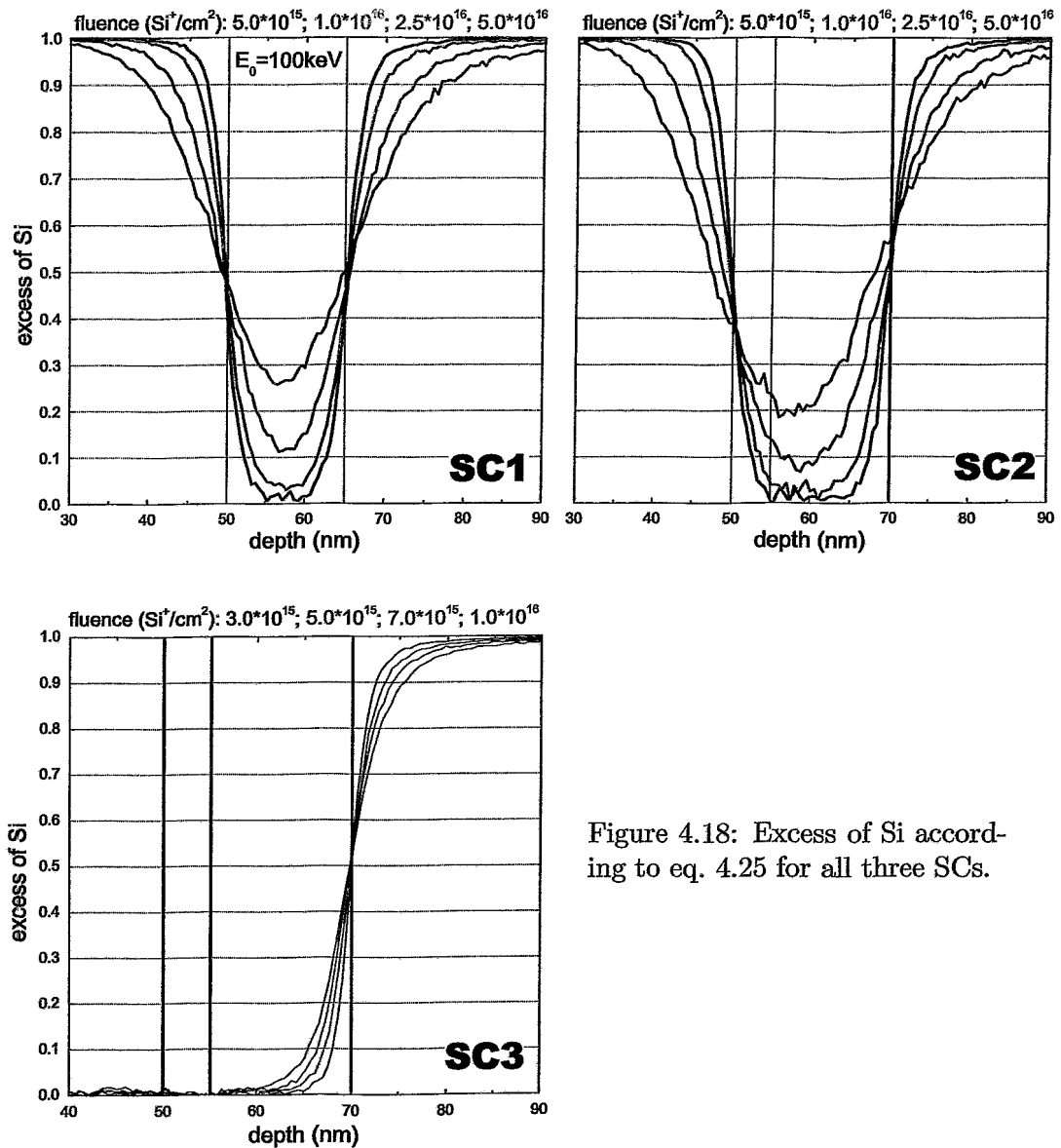
Figure 4.18: Excess of Si according to eq. 4.25 for all three SCs.

- Implantation close to the sample surface causes external chemical impact after removing the sample from the implantation chamber. Thus, oxygen and humidity from the ambient penetrate the sample surface and are stored in the surface-near region of the damaged oxide. Thus, a certain amount of the implanted species is oxidized during annealing, resulting in additional oxide swelling $(V_{SiO_2} \approx 2.2 V_{Si})$ [SCB02].

- If the implantation profile has its maximum close to the SiO_2-$Si_{substrate}$ interface, end-of-range defects are located in the region of the MOS transistor channel which leads to interference with the electronic properties of the transistor cell.

Chapter 5

Phase Separation

5.1 Regimes of Phase Separation

The previous chapter elucidated that ion mixing transfers a 15 nm thin SiO_2 layer, which is embedded in between a 50 nm thick Si capping layer and the Si substrate, into a region of substoichiometric oxide, i.e. into SiO_x with $x<2$. The substoichiometry of the oxide is obviously a function of depth (see fig. 5.2).

After ion irradiation, the system is in a state far from equilibrium, i.e. in a state of metastability or even instability. Moreover, the system is thermodynamically speaking "closed" after ion bombardment, i.e. at least exchange of matter with the surroundings is prevented. At sufficient high temperature, a relaxation process consequently starts which is expressed by phase separation into regions of Si and SiO_2. The separation of SiO_x into two phases obeys the following balance:

$$SiO_x \longrightarrow \frac{x}{2} SiO_2 + \left(1 - \frac{x}{2}\right) Si \ . \tag{5.1}$$
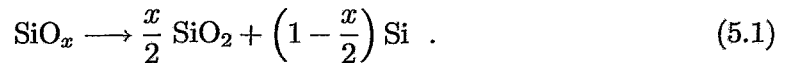
Depending on the degree of supersaturation, two different regimes of phase separation occur: nucleation and spinodal decomposition.

Phase separation can physically be described in the model of first-order phase transitions. The dynamics of phase separation is governed by a thermally activated material transport in the solid, i.e. by diffusion.

Due to the very low diffusion coefficients of Si in SiO_2, the system is metaphorically speaking "frozen" at RT, i.e. it would remain in the state of meta- or instability for a long period of time despite the tendency of separation into regions of SiO_2 and Si.

However, the time scale of phase separation can significantly be shortened by elevating the temperature of the sample. Diffusion processes generally depend on the temperature, T, of the system:

$$D(T) \propto \exp\left(-\frac{E_a}{kT}\right) \ , \tag{5.2}$$

where $D(T)$, E_a, and k denote the diffusion coefficient, the diffusion activation energy, and Boltzmann's constant, respectively.

From the experimental point of view, phase separation was performed at temperatures between 850° and 1050°C in the present cases. This thermal treatment is usually entitled "annealing." See section 3.2.4 for experimental details.

In the following, the two regimes are briefly portrayed. For a profound insight into the physics of phase separation and the particular fields of nucleation and spinodal decomposition, the reader is referred to [RAC78, WUD97, SCJ99].

5.1.1 Nucleation

The mechanism of phase separation via nucleation is valid for supersaturated, but still diluted systems. Fig 5.1 schematically depicts an idealized phase diagram of the binary system Si/SiO_2.
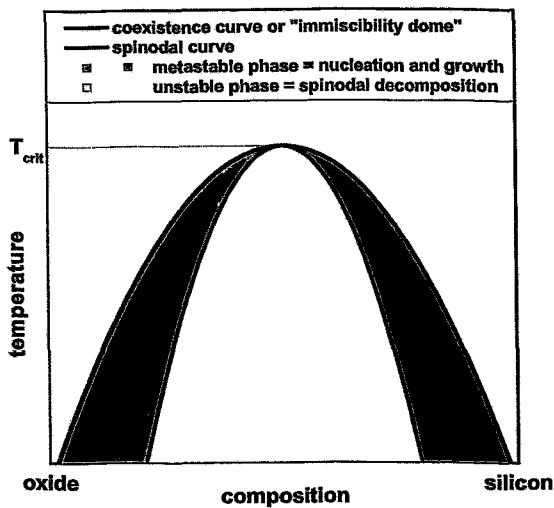

Figure 5.1: The Si/SiO_2 phase diagram schematically portrays the regions of metastability (cyan and magenta area) and instability (yellow area) of the homogeneous SiO_x ($x < 2$) phase. Depending on the degree of supersaturation, phase separation proceeds via nucleation or spinodal decomposition.

Figure 5.2: The 15 nm thick SiO_2 layer is decomposed into SiO_x ($x<2$) by ion irradiation (here, $E_0 = 100$keV and $\phi = 1 \cdot 10^{16} Si^+/cm^2$). The color code is applied in accordance with fig. 5.1.

Within the coexistence curve (cyan and magenta area), the system is in a state of metastability, i.e. it is in a local minimum of the free energy and, therefore, it is stable to small fluctuations in the local composition. Thus, the system can proceed from the homogeneous SiO_x state to phase separation into regions of Si and SiO_2 if a sufficiently large fluctuation occurs. This process is known as nucleation of a minority phase. It is triggered either by thermal fluctuations ("homogeneous nucleation") or by fluctuations which are induced by defects in the matrix ("heterogeneous nucleation").

In the present case, precipitates of Si are formed within the oxide (cyan area). Likewise, SiO_2 precipitates in the Si substrate (magenta area).

Since the system is closed, it relaxes towards equilibrium, i.e. towards the global minimum of F. In the course of nucleation, the contributions to the change in F are twofold according to the classical kinetic nucleation theory [VOM26]:
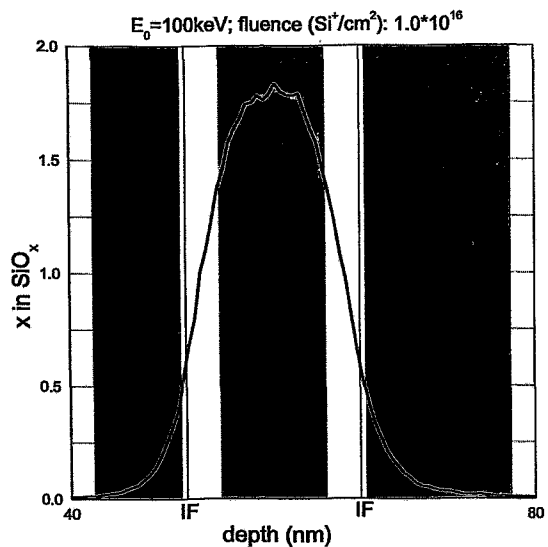
$$\Delta F = -\frac{4\pi}{3} r^3 \epsilon + 4\pi r^2 \sigma \quad , \tag{5.3}$$

where ϵ and σ denote the bulk free energy per unit volume and the surface free energy per unit area of the precipitate, respectively.

Obviously, there is a competition between surface and volume contributions in the free energy balance. On the one hand, the system lowers F by creating the volume of the precipitate which corresponds to a state of a minimum in F. On the other hand, the free energy of the system increases by creating an interface between the spherical precipitate and the surrounding matrix. Therefore, stable precipitates can only be formed if the bulk free energy "benefits" are larger than surface free energy "expenses."

This condition can mathematically be expressed by the maximum of $\Delta F(r)$:

$$\frac{\mathrm{d}(\Delta F(r))}{\mathrm{d}r} = 0 = -4\pi r^2 \epsilon + 8\pi r \sigma \quad , \tag{5.4}$$

which results in a critical radius,[1] r_c, for which eq. 5.4 is obeyed:

$$r_c = \frac{2\sigma}{\epsilon} \quad . \tag{5.5}$$

Accordingly, for precipitates with $r < r_c$, it is energetically favorable to reduce size, i.e. they release monomers to the surrounding matrix. On the contrary, precipitates with $r > r_c$ have an affinity for growth, i.e. monomers attach to them.

The above considerations have dealt with Si precipitates in the oxide phase as well as with SiO_2 precipitates in the silicon phase.

Thus, precipitates evolve on both sides of the SiO_2-Si interface which leads to Si NC formation in the oxide layer as well as SiO_2 NC formation in the substrate. For thermodynamical reasons explained below, these simultaneous processes proceed on different time scales resulting in structural asymmetry, i.e. SiO_2 NCs in the substrate dissolve more rapidly than Si NCs in the oxide which results in the desired sample structure of a Si NC δ-layer within SiO_2 above a pure Si substrate.

5.1.2 Spinodal Decomposition

There are regions in the phase diagram (see yellow area in fig. 5.1) where the surface free energy per unit area, σ, becomes insignificantly small. The spinodal curve in the phase diagram corresponds to $r_c = 0$. In this case, the homogeneous SiO_x phase is unstable towards arbitrarily small fluctuations in composition. Without any nucleation barrier, the unstable SiO_x phase immediately decomposes which results in the formation of interconnected (non-spherical) patterns of a Si and a SiO_2 phase. This situation is applicable to the regions where the degree of supersaturation is overwhelming after ion mixing. This condition is fulfilled in the region of the former interfaces (see fig. 5.2), where SiO_x with $0.5 < x < 1.5$ (approximate values) occurs. Here, the picture of a diluted matrix is not valid.

The mechanism of spinodal decomposition is driven by an overall interface minimization principle. Thus, in the immediate vicinity of a former interface, the two phases are

---

[1]known as critical nucleus size

rapidly separated from each other resulting in a minimum interface in this region, i.e. a flat phase boundary appears. In other words, spinodal decomposition leads to the prompt reformation of the Si–SiO$_2$ interface.

5.2   Growth and Ripening of the NC ensemble

In the regions of the oxide where phase separation proceeds via nucleation, the excess of silicon leads to growth of already existing precipitates, i.e. Si monomers attach to them. Phase separation ceases as soon as all excess Si is consumed.

A system which contains an ensemble of precipitates of different radii is not in equilibrium. On the relaxation path towards equilibrium, the precipitates "fight for survival," i.e. a selective process takes place.
The success of an individual Si precipitate decisively dependes on its radius r. Driven by an overall surface minimization principle, a redistribution process starts in the course of which small precipitates dissolve delivering monomers to the oxide matrix. These monomers attach to larger precipitates which develop to NCs.
The following considerations are addressed to this so-called Ostwald ripening (OR) of an precipitate ensemble which has attracted scientific interest since its discovery by Wilhelm Ostwald in 1900 [OSW00].
The first extensive theoretical description was published by Lifshitz, Slyozov, and Wagner ("LSW theory") in 1961 [LII61, WAC61]. Amongst other things, they discovered that the density of the number of precipitates decreases, whereas the volume of individual clusters linearly increases in time in the case of diffusion controlled OR.
In chapter 2, a striking feature of nanostructures was emphasized, namely the size-dependence of their physical properties.
In the case of spherical Si precipitates, the ratio between surface and volume energy strongly depends on the radius r. As mentioned in section 2.1, the impurity equilibrium concentration of monomers above a surface depends on its curvature. This phenomenon is described by the Gibbs-Thomson relation, given by [GOF81]

$$c^{GT}(r) = c_\infty \exp\left(\frac{R_c}{r}\right) \quad \text{with} \quad R_c = \frac{2\sigma V_a}{kT} \quad , \tag{5.6}$$

where c_∞ denotes the impurity equilibrium concentration of monomers above a flat surface ($r=\infty$). Here, R_c is the capillary length of the precipitate including terms referring to the surface tension, σ, and to the atomic volume, V_a.
Given this basic relation, two scenarios may occur concerning growth or shrinkage of a precipitate located in a monomer concentration field. If the concentration of monomers c^{MM} surrounding the precipitate is larger than c^{GT}, the precipitate acts as sink, i.e. monomers from the matrix attach to the precipitate (=growth). On the contrary, if c^{GT} is larger than c^{MM}, atoms detach from the precipitate (=shrinkage) (see fig. 5.3). Form an atomistic point of view, monomers have energetically to overcome a barrier at the interface between the precipitate and the surrounding matrix before they can migrate in the matrix. The ratio between the velocity of the detachment reaction and the monomer diffusion in the matrix determines the nature of OR -- whether it is reaction or diffusion controlled [STM96]. In the present case, Si monomers migrate within
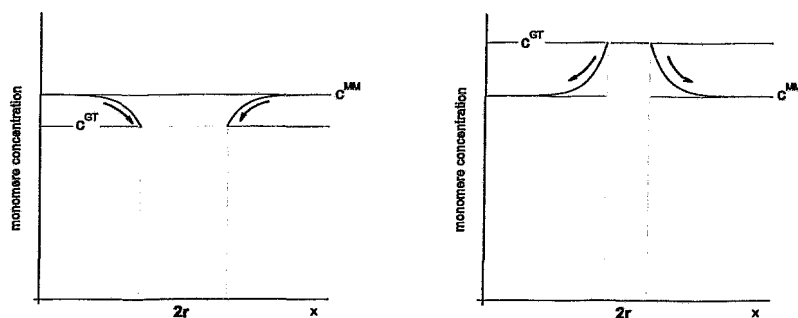
Figure 5.3: During Ostwald ripening, growth (left) or shrinkage (right) of a NC depends on whether $c^{GT}(r) < c^{MM}$ or $c^{GT}(r) > c^{MM}$.

SiO_2 which is assumed to be diffusion controlled due to the very low diffusivity of Si within SiO_2. The same argument holds for the OR of an ensemble of SiO_2 precipitates in the Si substrate [STM96].

The goal of the present work is to prove that a δ-layer of Si NCs within the oxide of a MOS structure emerges at a constant distance from the Si substrate in a self-organizing manner.

According to the mixing profiles discussed in chapter 4, a situation is applicable which is schematically drawn in figs. 5.4.1-6 for the SiO_2-$Si_{substrate}$ interface.

Due to the overall excess of Si in the oxide after ion irradiation (blue curve), spherical Si precipitates nucleate in every region of the oxide where phase separation proceeds via nucleation (see fig. 5.4.1). Throughout the ripening process, the Si substrate acts as perfect sink if one considers only dissolved Si monomers which exceed the solubility, c_∞. In this abstract picture, the Si substrate is a sphere of infinite radius within the oxide.

As soon as the Si monomer concentration in the oxide falls below c^{GT} of the smallest precipitates, Ostwald ripening starts (see figs. 5.4.2). Consequently, large precipitates grow at the expense of smaller ones which dissolve in Si monomers. The detachment of Si monomers from precipitates is supposed to be isotropic. Therefore, precipitates in the vicinity to the oxide-substrate interface permanently loose monomers on the one hand to the Si substrate, on the other hand to precipitates which are directed opposite of the substrate. The consequences are twofold: Firstly, a precipitate-free zone – the so-called "denuded zone" – emerges, the widths of which scales with the diffusion length, $\lambda \propto \sqrt{D(T)t}$, where $D(T)$ and t denote the diffusion coefficient and the process time, respectively (see figs. 5.4.3-5). Secondly, a layer of precipitates at a constant distance to the substrate is supplied with Si monomers (see fig. 5.4.3), as a result of which a layer of NCs grows up.

This NC layer, however, represents just an intermediate state of the system's relaxation path towards equilibrium. If phase separation continues (see figs. 5.4.4-6), the clusters in the δ-layer are not supported with monomers any longer. Finally, they dissolve, and all Si monomers in the oxide condense on the substrate (see fig. 5.4.6).

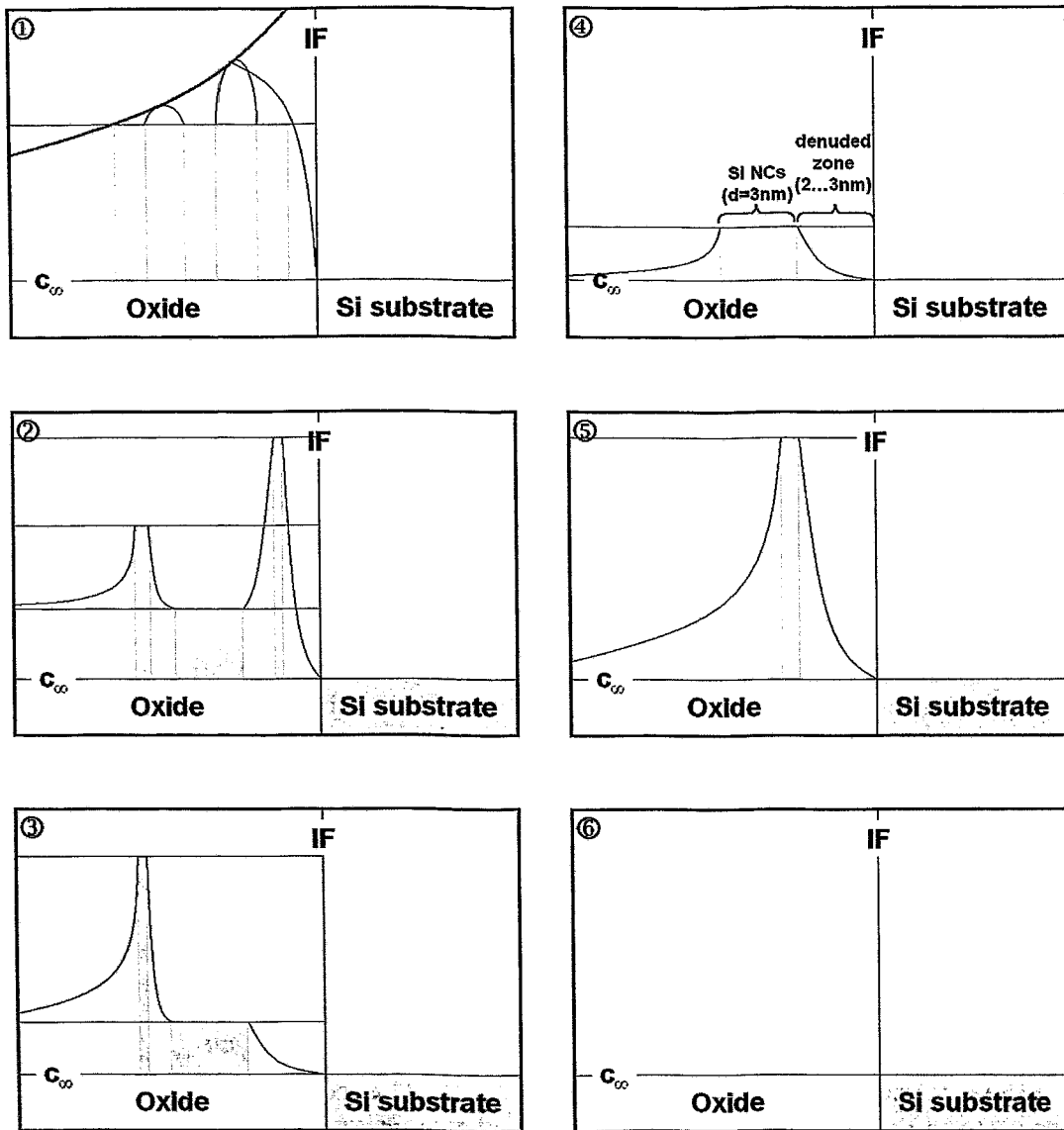For the sake of clarity, only the formation of Si NCs in the oxide is portrayed in

Figure 5.4: These schematic snapshots chronologically portray the course of Ostwald ripening at an ion-mixed SiO_2-Si interface. The phases of the NC ensemble evolution are described in the text. In all figures, the ordinate expresses the monomer solubility, $c(z)$, whereas the abscissa is related to the depth, z, of the sample. The grey columns in the region of the oxide refer to Si precipitates, the widths of which qualitatively indicate the altering diameters of the precipitates. Consequently, the curves portray the course of $c(z)$ in the oxide which locally differs due to the Gibbs-Thomson relation (see eq. 5.6).

figs. 5.4.1-6. Remember, that SiO_2 precipitates similarly nucleate in the Si substrate. As mentioned above, these two processes proceed on different time scales resulting in structural asymmetry, i.e. SiO_2 NCs in the substrate dissolve more rapidly than Si

NCs in the oxide.

Therefore, a δ-layer of Si NCs should be obtained if the process of OR discontinues immediately after reaching the status which corresponds to figs. 5.4.4-5. This can simply be achieved by instantly stopping annealing.

This rather empirical description of the course of phase separation at the interface requires further explanation.

The flux of Si monomers in the oxide depends on the product of two decisive quantities: solubility $c_{\mathrm{Si}}^{\mathrm{SiO_2}}$ and diffusivity $D_{\mathrm{Si}}^{\mathrm{SiO_2}}$. Thus, the following section briefly portrays the mechanisms which explain the migration of Si monomers in a SiO$_2$ host matrix.

5.3 Si Monomers in SiO$_2$

5.3.1 Diffusion

The general relation concerning diffusion of monomers in a matrix is expressed by Fick's first law,

$$\vec{j} = -D\nabla c \ ,\tag{5.7}$$

where $\vec{j}$, D, and ∇c denote the flux of monomers, the diffusion coefficient, and the gradient of the monomer concentration in the solid, respectively.

The gradient of c can be expressed by a linear approximation:

$$\nabla c = \frac{c - c_\infty}{\Delta x} \ .\tag{5.8}$$

Assuming that $c_\infty \ll c$, the monomer flux becomes approximately proportional to the product of solubility and diffusivity, e.g. in the case of Si monomers in a SiO$_2$ matrix:

$$j_{\mathrm{Si}}^{\mathrm{SiO_2}} \propto c_{\mathrm{Si}}^{\mathrm{SiO_2}} \cdot D_{\mathrm{Si}}^{\mathrm{SiO_2}} \ .\tag{5.9}$$

Therefore, a quantitative description of OR rests on experimental values of $c_{\mathrm{Si}}^{\mathrm{SiO_2}}$ and $D_{\mathrm{Si}}^{\mathrm{SiO_2}}$ in the present case.

Moreover, c and D are functions of temperature. In the picture of the Ising model (i.e. dissolution into the vacuum),

$$c = c_0 \cdot \mathrm{e}^{-\frac{E_c}{kT}} \ \text{and}\tag{5.10}$$

$$D = D_0 \cdot \mathrm{e}^{-\frac{E_a}{kT}} \ ,\tag{5.11}$$

where E_c and E_a denote the bulk cohesive energy and the activation energy for diffusion, respectively. c_0 and D_0 are pre-exponential factors.

E_c is lowered in the case of dissolution into a matrix because the monomers usually establish bounds to matrix atoms. In a first approximation, however, a determination of $c_{\mathrm{Si}}^{\mathrm{SiO_2}}$ can be based on the bulk cohesive energy of Si, i.e. the energy required to form separate neutral Si atoms in their ground state from the Si solid: E_{Si}=4.63 eV [KIC96]. For an annealing temperature of T=1000°C,

$$c_{\mathrm{Si}}^{\mathrm{SiO_2}} = 4.7 \cdot 10^{-19} c_0 \ .\tag{5.12}$$

Experimental data concerning c_0^{Si} in SiO$_2$ have not been found, and the value can hardly be calculated [HEK03p].

The determination of $D_{\text{Si}}^{\text{SiO}_2}$, is complicated as well. Different diffusion experiments have been conducted which revealed disparate results for D_0 as well as for E_a. Fig. 5.5 summarizes outcomes of three experiments which exhibit differences in $D_{\text{Si}}^{\text{SiO}_2}$ of some orders of magnitude for given T.
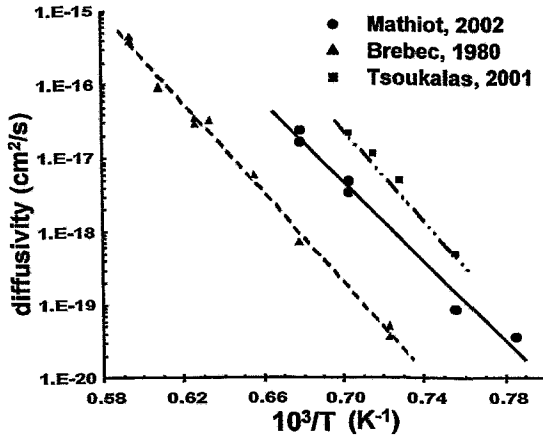
author	$D_0\,(\text{cm}^2/\text{s})$	$E_a\,(\text{eV})$
Mathiot	34.3	5.35
Brebec	328	6
Tsoukalas	1.378	4.74

Figure 5.5: Strong disagreement between the results of three experiments which were designed to determine the diffusivity of Si in SiO$_2$ (compare [MAD02, BRG80, TSD01]).

In terms of the diffusion length, $\lambda=\sqrt{D(T)t}$, the diffusivity values presented in fig. 5.5 are too low to describe the Si NC growth on a reasonable time scale (compare table 5.1).

$D_{\text{Si}}^{\text{SiO}_2}\,(\text{cm}^2/\text{s})$	$t\,(\text{s})$	$D_{\text{Si}}^{\text{SiO}_2}\,(\text{cm}^2/\text{s})$	$t\,(\text{s})$
10^{-12}	0.04	10^{-18}	$4{\cdot}10^4$
10^{-14}	4	10^{-20}	$4{\cdot}10^6$
10^{-16}	400	10^{-22}	$4{\cdot}10^8$

Table 5.1: For a diffusion length in the order of the denuded zone, $\lambda=2\,\text{nm}$, values for $D_{\text{Si}}^{\text{SiO}_2}$ and t are calculated.

For $T=1000°\text{C}$, all values of $D_{\text{Si}}^{\text{SiO}_2}$ are well below $10^{-18}\text{cm}^2/\text{s}$ (compare fig. 5.5). Relying on the experimental results presented above, an annealing time of many hours would be necessary for phase separation at the interface. This is in contradiction to the experimental outcomes of TEM and SIMS which are presented in subsections 5.4.2 and 5.4.3. Obviously, an effective diffusivity ($D_{\text{eff}}\gg D$) applies which incorporates the fact that diffusion starts in a state very far from thermodynamic equilibrium. Moreover, irradiation induced structural damage surely enhances the diffusion of Si monomers in the first moments of thermal annealing. D_{eff} is expected to be in the range between 10^{-14} and $10^{-16}\,\text{cm}^2/\text{s}$ for $T=1000°\text{C}$ (in green). A further possibility is that the NC ripening mechanism is governed by oxygen vacancy diffusion in addition to Si monomer diffusion [HEK03p].

Further experimental investigations are, therefore, indispensable in order to satisfyingly resolve this "diffusivity puzzle" in irradiated SiO$_2$.

5.3.2 Excursion to SIMOX

Besides the unsatisfying quantitative statements of several diffusion experiments, an interesting analogy can be drawn between the subject of the present work and former SIMOX studies. For two decades, numerous research groups have examined the kinetics of the formation of a buried SiO_2 layer as a result of high-dose oxygen implantation into silicon (see e.g. [STM83, NAS93, STJ93, ISY94, JIJ00]).

After annealing, many experimenters encountered Si inclusions in the buried oxide – even at annealing temperatures up to 1350°C for several hours (see fig. 5.6).

Figure 5.6: This series of CS TEM-images portrays the formation of Si islands in the buried oxide in dependence on annealing temperature. Here, the samples were implanted at 180 keV and 550°C with a fluence of $1.2 \cdot 10^{18}$ cm^{-2}. Thereafter, they were annealed at $T = \{1050; 1150; 1200; 1250; 1300; 1350\}$°C for $t = 4$h [NAS93].

Despite the different length scales of the Si islands in SIMOX in comparison with 2...3 nm Si NCs in the present case, an analogous conclusion imposes itself – the monomer flux of Si in SiO_2 is – qualitatively speaking – low compared to the monomer flux of oxygen in silicon.

Fig. 5.6 indicates the asymmetry in the growth of Si inclusions in SiO_2 and the growth of SiO_2 inclusions in Si. Obviously, SiO_2 inclusions in Si disappear more rapidly than Si inclusions in SiO_2 during thermal annealing.

Similar behavior is expected in the present experiments:

$$j_{Si}^{SiO_2} \quad < \quad j_O^{Si} \tag{5.13}$$

$$D_{Si}^{SiO_2} \cdot c_{Si}^{SiO_2} \quad < \quad D_O^{Si} \cdot c_O^{Si} \tag{5.14}$$

Three conclusions appear reasonable:

$$D_{Si}^{SiO_2} \quad < \quad D_O^{Si} \quad \text{or} \tag{5.15}$$

$$c_O^{Si} \quad > \quad c_{Si}^{SiO_2} \quad \text{or} \tag{5.16}$$

$$c_O^{Si} > c_{Si}^{SiO_2} \quad \wedge \quad D_{Si}^{SiO_2} < D_O^{Si} \quad . \tag{5.17}$$

5.4 Formation of NC δ-layers

5.4.1 Prediction of Kinetic Monte-Carlo Simulations

The course of phase separation towards thermodynamic equilibrium can numerically be simulated by Monte-Carlo computer codes. Although reliable input parameters are

not available, such atomistic simulations can predict the relaxation path of the system for different annealing conditions.

A multi-component kinetic lattice Monte-Carlo program (KLMC), which takes diffusion processes, phase separation, OR, and chemical reactions into account and, therefore, allows to simulate the formation of the desired NC δ-layer structure, was developed by Heinig and coworkers in recent years [HEK03, RES96, STM99t, STM01].

The program predefines a fcc-lattice cell of some 10^6 lattice sites which are partly occupied with atoms of the minority phase, i.e. Si in the present case. The empty lattice sites represent the majority phase, here SiO_2. The simulation rests on the assumption that the Si atoms move in the chemically inert SiO_2 matrix.

Therefore, Si impurity distributions which were taken from $c_{Si,excess}(x)$ TRIDYN profiles are important simulation inputs. Moreover, thermodynamic data (bond strengths, capture radii, solubilities, diffusivities, and temperature) have to be given.

In the simulation, positional changes of atoms are expressed in terms of probabilistic jumps of atoms between nearest neighbor (NN) lattice sites. Using the Metropolis algorithm [MEN53], the jump probability, $P_{i \to f}$, is given by

$$P_{i \to f} = \left\{ \begin{array}{ll} \tau_0^{-1} \exp\left(-\frac{E_a}{kT}\right) & , n_i < n_f \\ \tau_0^{-1} \exp\left(-\frac{E_a + (n_i - n_f)E_b}{kT}\right) & , n_i \geq n_f \end{array} \right\} , \qquad (5.18)$$

where τ_0^{-1} denotes the jump frequency. n_i and n_f denote the number of NN bonds at the initial and final lattice site, respectively. E_a characterizes the diffusion barrier of impurity atoms in a single NN jump. The NN bond strength is expressed by E_b. τ_0^{-1}, E_a and E_b are related to macroscopic experimental quantities – annealing time t, annealing temperature T, diffusivity $D_{Si}^{SiO_2}$, and solubility $c_{Si}^{SiO_2}$.

The time constant of the simulation, τ, is the so-called Monte-Carlo step, the duration of which depends on the diffusion coefficient $D(T)$. Since $D_{Si}^{SiO_2}(T)$ is rather unknown in the present cases, the duration of a Monte-Carlo step is uncertain, too. Thus, the conversion of the physical time, t, into the simulated time, τk (k is the total number of Monte-Carlo steps in a simulation), can only be performed with an assumed or measured diffusion coefficient.

However, the simulation does provide an imagination of the course of phase separation and NC-layer formation – merely in terms of an artificial, i.e. temperature-dependent, time scale, $k(D(T))$.

This rather brief characterization does not nearly cover all features of the kinetic lattice Monte-Carlo method. For a deeper insight, the reader is, therefore, referred to the references given above.

For illustration, fig. 5.7 presents snapshots of the course of phase separation in the case of SC1.

The first figure, 5.7(a), portrays the sample after ion irradiation with $\phi = 1 \cdot 10^{16} \, Si^+/cm^2$. The black curve indicates the Si excess distribution which was calculated with eq. 4.25 from TRIDYN profiles. Note the asymmetry in figs. 5.7(b) and 5.7(c) between the Si NC band in the oxide and the SiO_2 NC layer in the substrate. From a simulative point of view, this asymmetry was achieved by assuming different solubilities which are expressed as difference in E_b, i.e. $E_b(Si-Si \text{ in } SiO_2) : E_b(O-O \text{ in } Si) = 3 : 5$, where $E_b(O-O)$ means the efficient bond strength "between" oxygen atoms when it forms SiO_2 in Si.
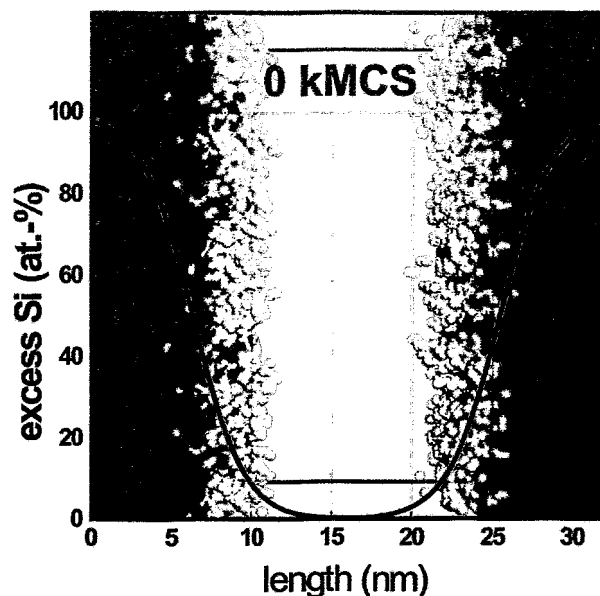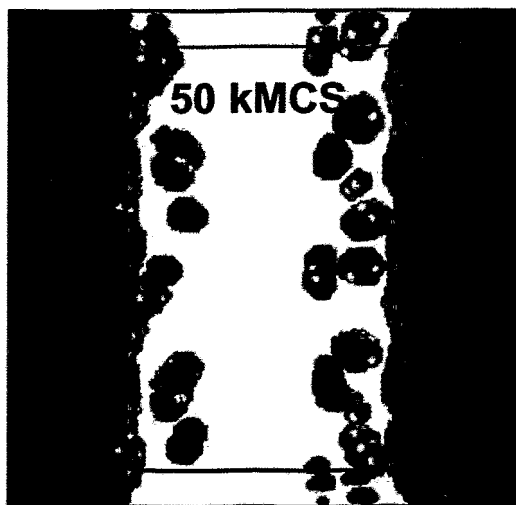
Figure 5.7: KLMC simulation of SC1 (performed by K.-H. Heinig, FWIT, 2003).

(a) The 3D simulation cell in the as-irradiated condition.

The black curve corresponds to the Si excess distribution calculated with TRIDYN for $\phi = 1 \cdot 10^{16}\,Si^{+}/cm^{2}$. The color code of the atoms reflects the number of diatomic bonds of the Si atoms.

(b) After 50.000 MC steps, excess Si has precipitated in the oxide. Likewise, SiO_2 precipitates occur in the substrate.

Note, that the oxide-substrate interface is reformed but still rough. The fact that $j_{Si}^{SiO_2} < j_{O}^{Si}$ causes SiO_2 precipitates in the Si substrate to dissolve more rapidly than Si precipitates in the oxide.
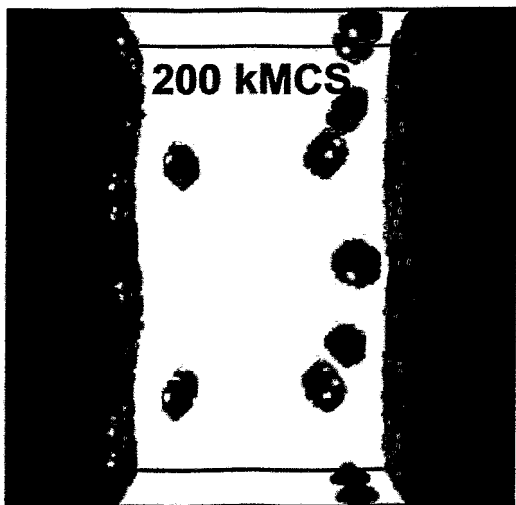
(c) After 200.000 MC steps, the NC density has decreased. The NCs appear arranged – i.e. self-organized – in a "δ-layer" which is separated from the substrate by a denuded zone.

Again, less SiO_2 NCs exist in the substrate than Si NCs in the oxide. As phase separation continues, all SiO_2 clusters dissolve, whereas Si NCs remain in the oxide (not shown here).

The interface is perfectly smooth.

5.4.2   TEM Study of SC1

As mentioned earlier in this work (compare subsection 3.3.1 and fig. 4.2), Si NCs within SiO$_2$ are not visible in TEM if they are smaller than 2...3 nm in diameter.

In the case of SC1, this experimental handicap limits the proof of the formation of NC δ-layers to the band of SiO$_2$ NCs in the substrate. Amorphous SiO$_2$ NCs in crystalline Si are clearly visible in TEM because they break the symmetry of the Si crystal.

For this purpose, the samples of SC1 were implanted at elevated temperatures of 400° and 600°C in order to preserve the crystallinity of the substrate. Thus, SiO$_2$ inclusions in the Si substrate are detectable directly after ion implantation.

Figs. 5.8, 5.9, 5.10, and 5.11 indicate that the formation of SiO$_2$ inclusions in the substrate is a function of ion fluence, ϕ, and target temperature during irradiation, T_{target}.

In the case of implantation at RT, the substrate is fully amorphized, thus, no inclusions appear in the irradiated state (compare fig. 4.2).
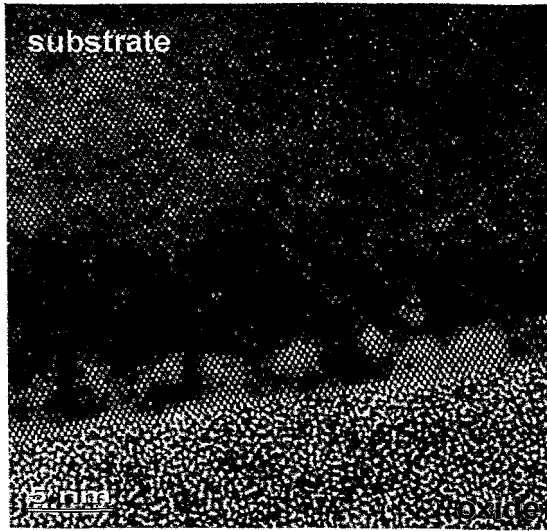
Figure 5.8: CS TEM image of SC1. E=100keV, ϕ=2.5·10$^{16}\frac{Si^+}{cm^2}$, T_{target}=400°C. The substrate remains crystalline during implantation, although the substrate-oxide IF is roughened due to irradiation. The substrate region close to the interface contains bright spherical patterns of 1...3 nm in diameter which are pronounced precipitates of SiO$_2$ within Si. Due to the temperature regime, phase separation already takes place during implantation, obviously.
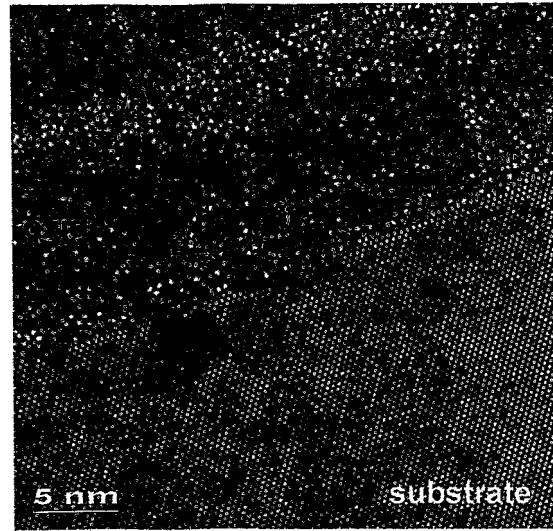
Figure 5.9: CS TEM image of SC1. E=100keV, ϕ=2.5·10$^{16}\frac{Si^+}{cm^2}$, T_{target}=600°C. Compared to fig. 5.8, the oxide-substrate IF remains smooth which is obviously due to the higher target temperature during implantation. The substrate remains almost perfectly crystalline which leads to the conclusion that less oxygen nucleates as SiO$_2$ precipitates in the substrate than in the case of $T_{target} = 400$°C.

After ion irradiation at elevated target temperature, the samples were thermally annealed at $T_{anneal} = 1000$°C for various annealing times $t_{annealing}$={30;750}s. As an illustration of the course of phase separation, the case of $\phi = 5.0 \cdot 10^{16}$Si$^+$/cm^2, $T_{target} =$

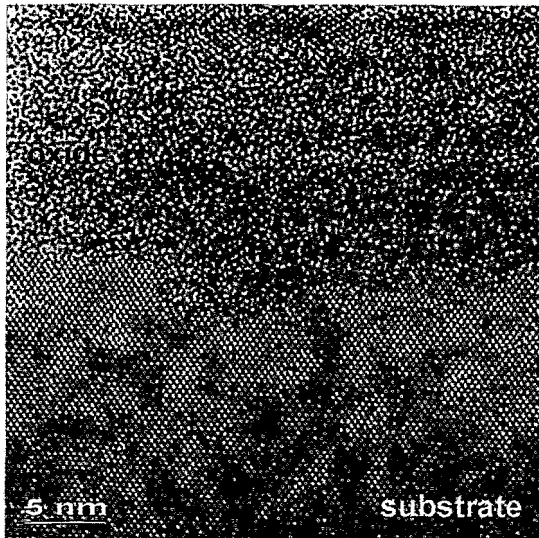Figure 5.10: CS TEM image of SC1. E=100keV, ϕ=5.0·$10^{16}\frac{\text{Si}^+}{\text{cm}^2}$, T_{target}=400°C. The interface-near substrate exhibits heavier damage of the substrate than in the case of $\phi = 2.5 \cdot 10^{16}\text{Si}^+/\text{cm}^2$ (dpa$(x) \propto \phi$). The IF is more strongly roughened, too.

The density of SiO$_2$ precipitates has significantly increased which can be explained by the higher concentration of oxygen in the substrate. Compared to fig. 5.11, the SiO$_2$ precipitates are randomly distributed.
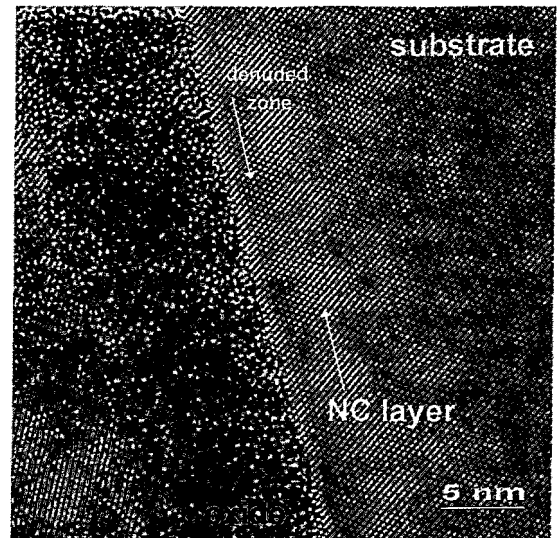
Figure 5.11: CS TEM image of SC1. E=100keV, ϕ=5.0·$10^{16}\frac{\text{Si}^+}{\text{cm}^2}$, T_{target}=600°C. A pattern of SiO$_2$ precipitates occurs in the substrate which inevitably reminds on the outcome of the Monte-Carlo simulations. Separated by a zone denuded of SiO$_2$ inclusions, a band of SiO$_2$ precipitates has formed at a distance of 1...2 nm from the interface. Consequently, phase separation and SiO$_2$ NC growth have already taken place during implantation at $T_{\text{target}} = 600°C$. Unfortunately, Si NCs in the oxide do not occur! However, the thin band in the oxide next to the oxide-substrate IF may be interpreted as denuded zone, i.e. as region free of Si excess.

600°C, is portrayed here. The corresponding TEM images are presented in figs. 5.12, 5.13, and 5.14.

Fig. 5.15 makes a comparison between the outcomes of 3D-KLMC simulations and 2D-TEM images. This comparison is of qualitative nature since the experiments were conducted at fluences of $\phi = \{2.5; 5.0\} \cdot 10^{16}\text{Si}^+/\text{cm}^2$, whereas in the KLMC simulations $\phi = 1.0 \cdot 10^{16}\text{Si}^+/\text{cm}^2$ was assumed. The message, nevertheless, is very similar, namely the formation of a SiO$_2$ NC layer in the substrate at the SiO$_2$-Si interface. However, the actual structure of interest, i.e. the layer of Si NCs in the oxide, still remains concealed in TEM. Yet, by induction, one may imagine Si NCs in the oxide as well. This argument does not withstand the scientific dispute.

Therefore, additional methods had to be found in order to prove the existence of Si NCs in the oxide as well. In this respect, two methods were considered: firstly, SIMS measurements and, secondly, Ge decoration experiments.
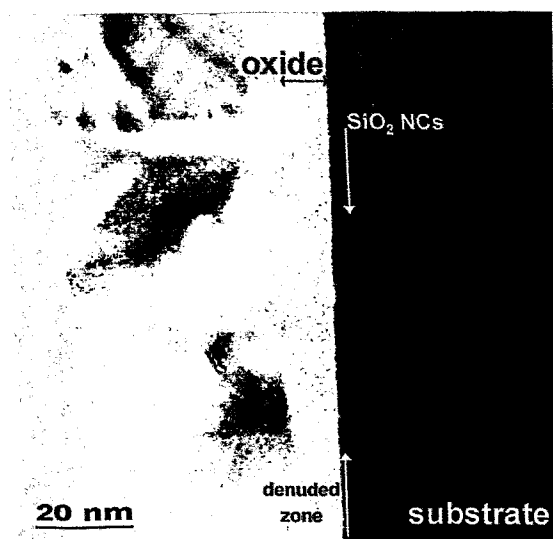
Figure 5.12: CS TEM image of SC1. E=100keV, ϕ=5.0·10$^{16}\frac{Si^+}{cm^2}$, T_{target}=600°C, $T_{annealing} = 1000$°C, $t_{annealing} = 30$s.
After 30 s of annealing, the SiO$_2$ inclusions in the substrate are still diffuse (comp. fig. 5.11) The denuded zone in the substrate is clearly visible.
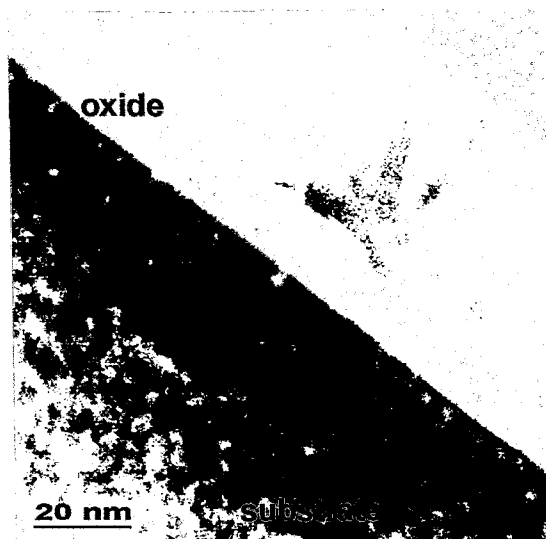

Figure 5.13: CS TEM image of SC1. E=100keV, ϕ=5.0·10$^{16}\frac{Si^+}{cm^2}$, T_{target}=600°C, $T_{annealing} = 1000$°C, $t_{annealing} = 750$s.
The SiO$_2$ inclusions are more accentuated after 750 s of annealing. They appear as sperical NCs. See fig. 5.14 for higher magnification.
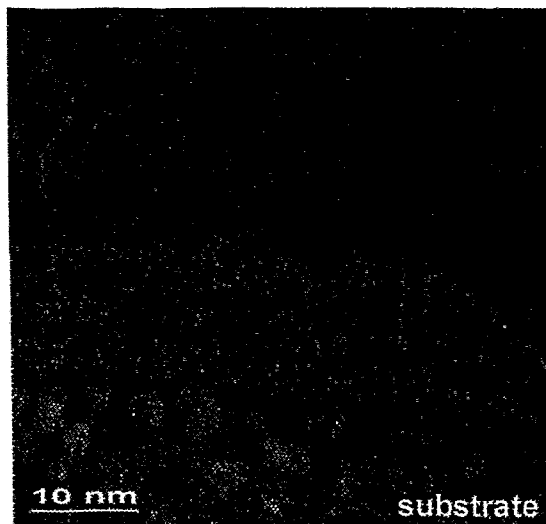

Figure 5.14: cf. fig. 5.13.
Again, the SiO$_2$ NCs in the substrate appear as spherical objects of 2...3 in diameter. The NC ensemble, however, is not an ideal NC monolayer which can be explained by the high ion fluence, ergo high amount of mixing, in this case.

Figure 5.15: Comparison between figs. 5.14 and 5.7(b). A qualitative agreement between KLMC simulation and TEM image in terms of SiO$_2$ NCs in the substrate can be announced. Si NCs in the oxide, however, do not appear in the TEM image due to their tininess and their weak contrast to the surrounding oxide.

5.4.3   Approval by SIMS

As mentioned in section 3.3.3, Si_n $(n>1)$ signals serve as indicator of Si excess in the oxide. Moreover, local maxima in the Si_n $(n>1)$ curves explain the presence of Si NCs in the oxide [PEM03].

In figure 5.16, the Si_2 signals exhibit a local peak in a distance of 3...4 nm from the SiO_2-Si interface for $t_{annealing} \geq 120$ s. The local peak width is approx. 2 nm (blue curve), i.e. in the order of the expected mean NC diameter.

The denuded zone between the local Si_2 peak and the interface emerges as little dip in the Si_2 signal. The dip does not appear more accentuated because of the overlapping signals originating in the Si substrate and in the Si NC layer. This overlap is due to the limited depth resolution of ToF SIMS which is approximately ± 1 nm [PEM03p].
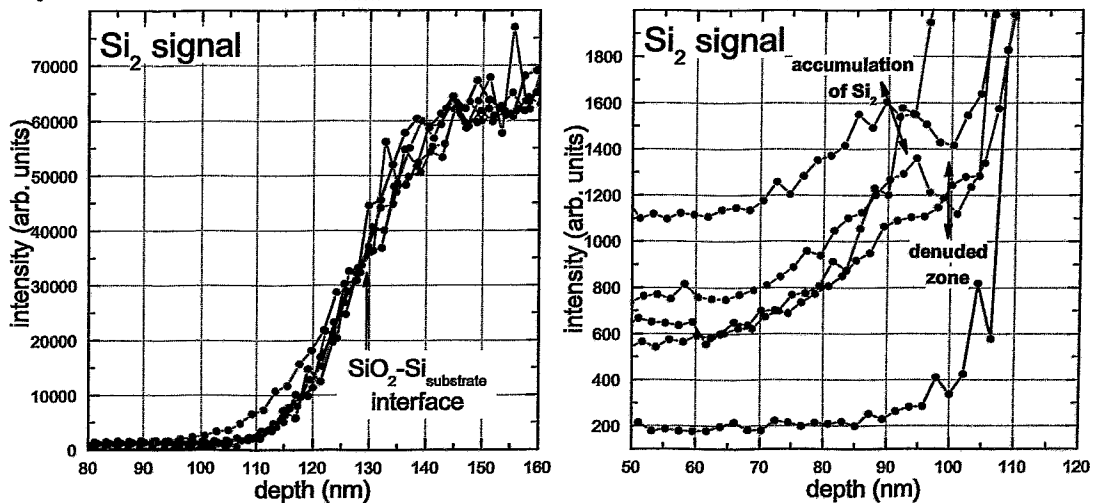

Figure 5.16: ToF SIMS spectrum of the Si_2 signal of SC1 for various annealing conditions.
left hand side: The SiO_2-Si interface is defined at the position where the Si_2 signals coincide at half maximum. The Si_2 signal confirms the excess of Si in the oxide layer after ion irradiation (red curve).
right hand side: During annealing, phase separation starts which ends up with a denuded zone between the substrate and the NC layer (blue and magenta curve). The hillocks in the Si_2 signals indicate the existence of Si NCs.

A further interesting feature of fig. 5.16 is the fact that the inner region of the oxide, which is theoretically expected to be free of Si excess after annealing, contains a relatively high amount of Si_2 in comparison with the stoichiometrically pure reference oxide. This implies that the thermal budget of annealing is to small in the present cases. During phase separation, excess Si does not obviously completely condense on the Si NC monolayer. However, phase separation clearly proceeds in the first 10^2 s of annealing which is not consistent with the assumption that (given the above experimental values of $D_{Si}^{SiO_2}$) only Si monomer diffusion contributes to phase separation.

The above SIMS results are mere indications of the existence of Si NCs in the oxide.

However, direct structural evidence is still missing. Due to the unobservability of tiny Si NCs within a SiO$_2$ matrix, a mechanism of contrast enhancement was necessary which is introduced in the following section.

5.5   Contrast Enhancement by means of Ge

All efforts to visualize Si NCs, which are smaller than 3 nm in diameter, in SiO$_2$ have failed applying common high-resolution TEM.

Thus, there has been a dire need for a method to reveal their existence in TEM which would irrefutably count as structural evidence of the presence of Si NCs in the oxide. For this purpose, germanium was used to "decorate" already existing Si NCs. In this connection, Ge is a unique element because of its similar chemical properties but its significantly higher mass.

5.5.1   Ge and the Si-SiO$_2$ System

The basic idea of Si NC decoration by means of Ge rests on the thermodynamic properties of the three elements involved.

The diatomic Ge–Ge bond strength is approx. 20% weaker than the Si–Si bond [KIC96]:

$$E_{\text{Si–Si}} = 4.63\,\text{eV}\quad\text{and} \tag{5.19}$$

$$E_{\text{Ge–Ge}} = 3.85\,\text{eV}\;. \tag{5.20}$$

Due to the fact that Ge and Si are arbitrarily miscible [GLW70], the diatomic bond strength between Si and Ge can be calculated with

$$E_{\text{Si–Ge}} = 0.5 \cdot (E_{\text{Si–Si}} + E_{\text{Ge–Ge}})\;. \tag{5.21}$$

$$\text{Thus,}\quad E_{\text{Si–Ge}} = 4.24\,\text{eV}\;. \tag{5.22}$$

In SC2, a 5 nm Ge layer was inserted between the oxide and the poly-Si capping layer. Figs. 4.9 and 4.15 have shown that the oxide contains a considerable amount of Ge (2...5 at.-%) after ion irradiation. Thus, Ge monomers are available as interstitials in the oxide which energetically tend to form Si–Ge bonds during thermal annealing since $E_{\text{Si–Ge}} > E_{\text{Ge–Ge}}$. Therefore, a Ge monomer flux is set in motion towards the Si substrate which can be interpreted as sink for Ge monomers. If Ge monomers pass Si NCs or Si precipitates on their path towards the substrate, they instantly form Si–Ge bonds with the Si atoms of the precipitates. In the present work, this process is entitled "Si NC decoration by Ge."

After ion irradiation, germanium and oxygen monomers can also form Ge–O bonds. From an energetic point of view, this configuration is less convenient for the system, since the diatomic Si–O bond is about 21% stronger than the diatomic Ge–O bond[2]. As in the case of Si, the diffusivity of Ge monomers in ion irradiated SiO$_2$ is unknown. Nevertheless, one may assume that the effective diffusivity D_{eff} of Ge in irradiated SiO$_2$

---

[2]D°_{298}(Si–O) $= 799\,\text{kJ/mol}$, D°_{298}(Ge–O) $= 659.4\,\text{kJ/mol}$ [CRC94].

is significantly higher than the diffusivity D of Ge in thermally grown and stoichiometrically pure SiO_2. Because of this lack of experimental data, one may assume in a first approximation that $D_{eff}(Si$ in $SiO_2)$ is approximately equal to $D_{eff}(Ge$ in $SiO_2)$. However, $j_{Si}^{SiO_2}$ and $j_{Ge}^{SiO_2}$ also depend on the solubility of the two elements in the oxide. In this connection, a comparison between $c_{Ge}^{SiO_2}$ and $c_{Si}^{SiO_2}$ may be done semi-quantitatively by assuming that $c_0^{Si} = c_0^{Ge} = c_0$, thus (for T=1000°C),

$$c_{Ge}^{SiO_2} = 5.8 \cdot 10^{-16} c_0 \quad \text{and} \tag{5.23}$$

$$c_{Si}^{SiO_2} = 4.7 \cdot 10^{-19} c_0 \quad . \tag{5.24}$$

Here, $E_c^{Si} = E_{Si-Si} = 4.63\text{eV}$ and $E_c^{Ge} = E_{Ge-Ge} = 3.85\text{eV}$, according to eq. 5.10. The reader is reminded that these bulk cohesive energy values are strictly valid only for dissolution into the vacuum. In the present cases, however, the monomers dissolve into SiO_2. Nevertheless, they can be applied in the framework of a first approximation. The corresponding results are schematically portrayed in fig. 5.17. Accordingly, the flux of germanium monomers in the oxide is expected to be higher than the flux of silicon monomers in SiO_2 since the probability of detachment, P_{detach} is proportional to $\exp(E_c/kT)$.
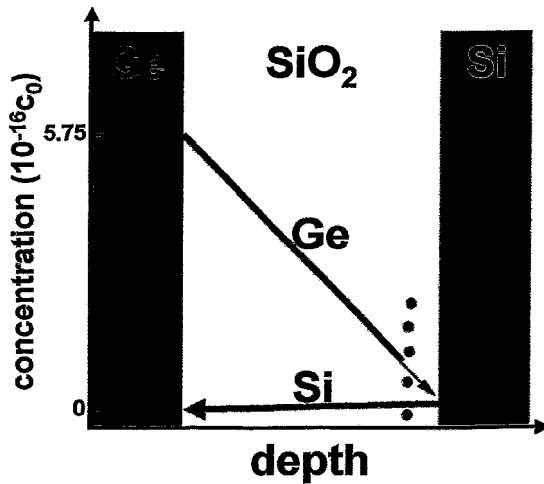

Figure 5.17: The Ge solubility is significantly higher than the solubility of Si. For energetic reasons, Ge monomers tend to form Ge–Si bonds. Thus, a flux of Ge monomers towards the Si substrate is expected which is much larger than the flux of Si monomers towards Ge. On this path through the irradiated oxide, Ge monomers pass Si precipitates to which they may attach forming Si–Ge bonds. Thus, an ensemble of Si_xGe_{1-x} NCs ripens in the oxide which is visible in TEM.

Because of the random path on which Ge monomers migrate during diffusion in SiO_2, the Si precipitates in the oxide act as very effective sink for Ge monomers. Thus, the major fraction of Ge atoms moving towards the substrate attaches to Si precipitates at first which is entitled "Ge decoration". In terms of TEM analysis, Ge atoms enhance the mass contrast of already existing Si NCs in the oxide.

The functionality of this mechanism is experimentally demonstrated in the subsequent subsections. In the case of SC2, the Si capping layer turned out to be less favorable since it also acts as sink for germanium. Therefore in SC3, the capping layer was chosen to consist of SiO_2 in order to symmetrically surround the Ge layer with SiO_2.

5.5.2 Study of SC2

In the case of SC2, relatively high ion fluences of $\phi = \{2.5; 5.0\} \cdot 10^{16} \, Si^+/cm^2$ were applied in order to achieve a considerable content of 2...5 at.% Ge in the oxide layer. For

a quantitative illustration, compare the corresponding TRIDYN profiles in figs. 4.9 and
4.18.2.

Like in the case of SC1, the excess of Si in the oxide nucleates in form of Si precipitates
to which Ge monomers are likely to attach for energetic and migrational reasons ex-
plained above. Thus, NCs consisting of both species silicon and germanium grow up.
Figs. 5.18 to 5.22 demonstrate that this mechanism of NC formation was observed in
TEM.

However, the effect of contrast enhancement turned out to be weaker than expected.
This can be explained by means of the the RBS spectra in fig. 5.23. The 50 nm Si
capping layer turned out to be very attractive towards Ge atoms. Therefore, the prin-
cipal part of the initially 5 nm thick Ge layer mixed with the Si in the capping layer
forming a Si–Ge alloy. The RBS spectra brilliantly demonstrate this Si–Ge intermixing
as function of annealing temperature. Therefore, the concentration gradient between
Ge layer and Si substrate significantly decreased causing a simultaneous reduction of
the flux of Ge monomers to the Si substrate. In the case of SC3, this effect could be
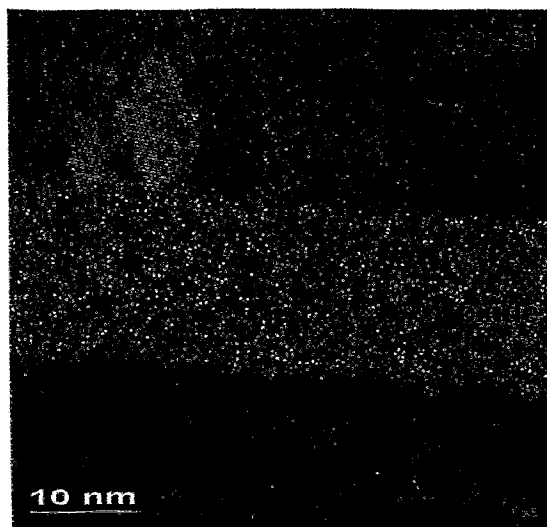suppressed by replacing the Si capping layer with SiO_2.

Figure 5.18: CS TEM image of SC2.
E=100keV, $\phi = 2.5 \cdot 10^{16}Si^+/cm^2$,
$T_{annealing} = 1000°C$, $t_{annealing} = 30s$.
After 30 s of annealing, the oxide does not
contain NCs nor any other structural pat-
terns. However, dark "veils of mist" can
be identified in the oxide originating from
Ge. Thus, a higher temperature budget is
necessary for cluster formation.
A distinction between the Ge layer and the
50 nm Si capping layer is no longer possi-
ble since Si and Ge have formed an alloy in
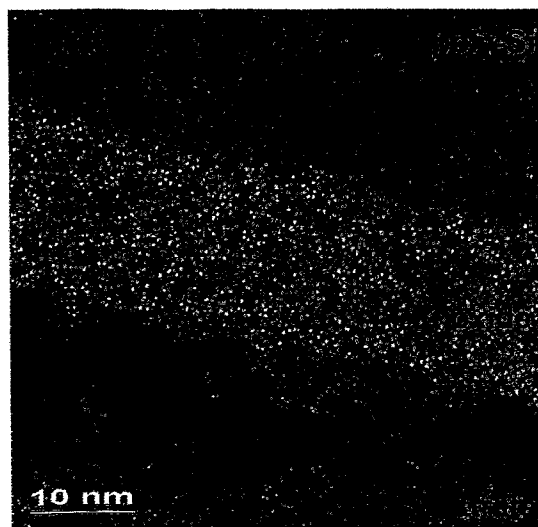this region (compare figs. 3.13 and 5.23).

Figure 5.19: CS TEM image of SC2.
E=100keV, $\phi = 5.0 \cdot 10^{16}Si^+/cm^2$,
$T_{annealing} = 1000°C$, $t_{annealing} = 30s$.
This TEM image contains the same fea-
tures like fig. 5.18. The only difference is
the higher degree of IF roughness which is
due to the higher ion fluence in this case.
Again, greyish veils occur in the oxide
which refer to the contrast enhancing con-
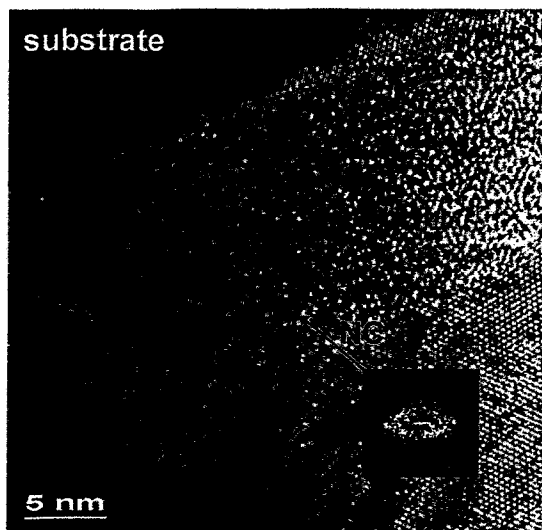tent of Ge in the oxide.

Figure 5.20: CS TEM image of SC2. E=100keV, $\phi = 2.5 \cdot 10^{16}\mathrm{Si}^+/\mathrm{cm}^2$, $T_{\mathrm{annealing}} = 1000°\mathrm{C}$, $t_{\mathrm{annealing}} = 270\mathrm{s}$. A higher termal budget causes NC formation in the oxide. The cluster portrayed here is about 3 nm in diameter and is even crystalline as its corresponding FT image reveals. The distance of the lattice plains turned out to be $d_{\mathrm{NC}} = 0.337\,\mathrm{nm}$ which comes very close to the bulk values of $d_{\mathrm{Si}}(111) = 0.3136\,\mathrm{nm}$ and $d_{\mathrm{Ge}}(111) = 0.3266\,\mathrm{nm}$.

In this case, it is not reasonable to conclude the ratio between Ge and Si in the cluster from d_{NC}. One the one hand, the lattice properties of the NC do certainly not completely coincide with the lattice properties in the corresponding bulk materials, one the other hand, the systematic error of determining d_{NC} is large due to the tininess of the cluster.
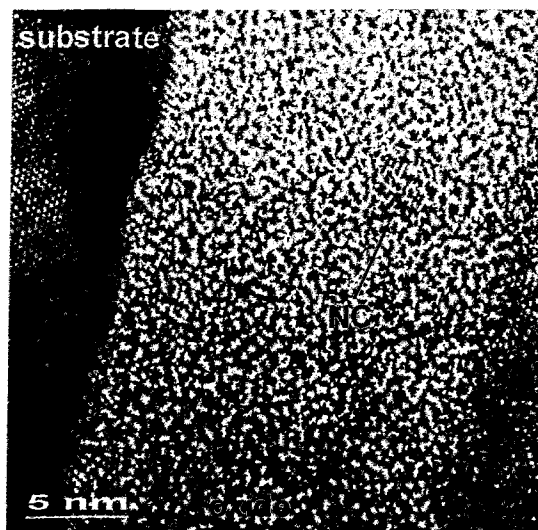
Figure 5.21: CS TEM image of SC2. E=100keV, $\phi = 2.5 \cdot 10^{16}\mathrm{Si}^+/\mathrm{cm}^2$, $T_{\mathrm{annealing}} = 1000°\mathrm{C}$, $t_{\mathrm{annealing}} = 750\mathrm{s}$. This image shows an high resolution TEM image similar to this in fig. 5.20. Again, crystalline NCs occur which are 2...3 nm in diameter. Here, the distance between the cluster and the $_{\mathrm{poly}}\mathrm{Si}\text{-}\mathrm{SiO}_2$ interface is about 3 nm.

The probability that lattice plains are portrayed in the high resolution TEM images is low because the NCs are randomly oriented in space. TEM images of lower resolution give an impression of a larger region of the sample, thus, the bands of NCs appear more clearly in terms of differences on the grey scale (see fig. 5.22).

Again, longer annealing times cause further smoothing of the interfaces (compare fig. 5.20).
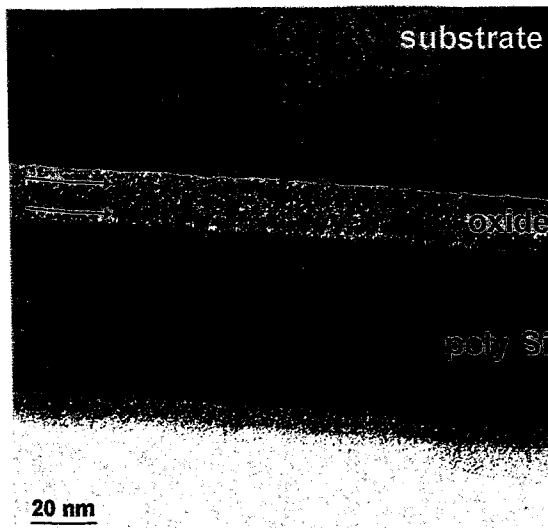
Figure 5.22: CS TEM image of SC2. E=100keV, $\phi = 2.5 \cdot 10^{16}Si^+/cm^2$, $T_{annealing} = 1000°C$, $t_{annealing} = 750s$. The two arrows point to the bands of NCs in the oxide (compare figs. 5.7.2-3). Although the contrast effect on the grey scale is rather weak, the denuded zones of about 3 nm clearly appear.
This structural feature becomes more apparent by rotating the paper about 90 degrees.
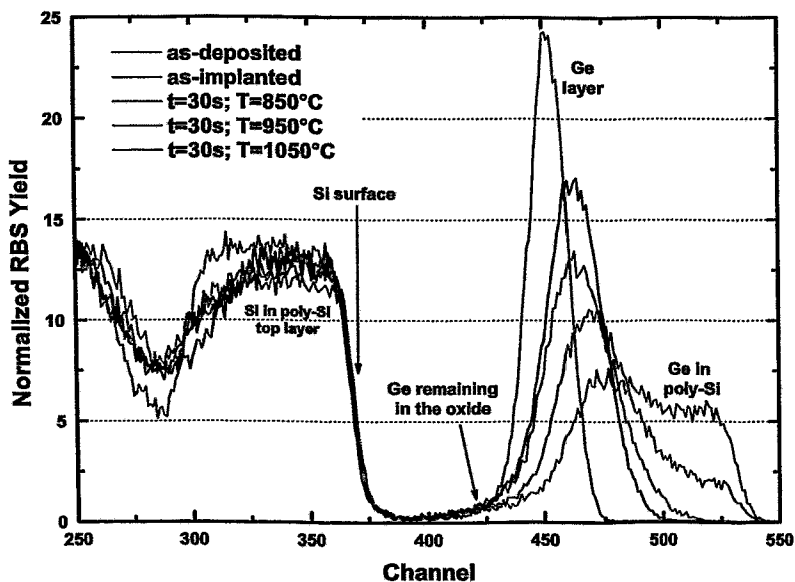

Figure 5.23: These RBS spectra of SC2 demonstrate that the principal amount of the 5 nm Ge layer mixes with the Si capping layer during annealing. The degree of mixing increases with increasing thermal budget – here, in terms of increasing annealing temperature at constant annealing time. In the case of T=1050°C (magenta curve), Ge is almost uniformly distributed throughout the capping layer. Thus, a Si_xGe_{1-x} alloy has formed at the interface between capping layer and oxide. Therefore, both the Si substrate and the capping layer act as sink for Ge monomers in the oxide. Accordingly, two NC layers are formed as being confirmed in fig. 5.22.

5.5.3 Study of SC3

Replacing the Si capping layer of SC2 with SiO_2 generates a symmetrical system, i.e. the Ge layer is surrounded by oxide on both sides and can be interpreted as Ge marker layer within SiO_2 from the standpoint of ion mixing.

The experimental investigations in the case of SC1 and SC2 were performed applying high ion fluences up to $5 \cdot 10^{16}$ Si^+/cm^2 resulting in Si excess concentrations up to 25 at.% in the middle and 40 at.% at the interfaces of the oxide (compare TRIDYN profiles in figs. 4.18.1-2).

Moreover, high fluences caused tremendous damage in the Si substrate which partially could not be fully annealed.

Therefore, in the experiments of SC3, lower fluences of $\{3; 7\} \cdot 10^{15}$ Si^+/cm^2 were applied. Accordingly, damage and Si excess are lower as well (see fig. 5.25). Here, Si excess occurs only at the SiO_2-substrate interface in accordance with eq. 4.25.

Fig. 5.24 demonstrates that the Ge layer is decomposed into spheres of 10...30 nm in diameter during thermal annealing. Although $T_{melting}(Ge) = 937°C$, the spherical shape indicates that the Ge reached the liquid state during annealing even at $T_{annealing} = 850°C$.
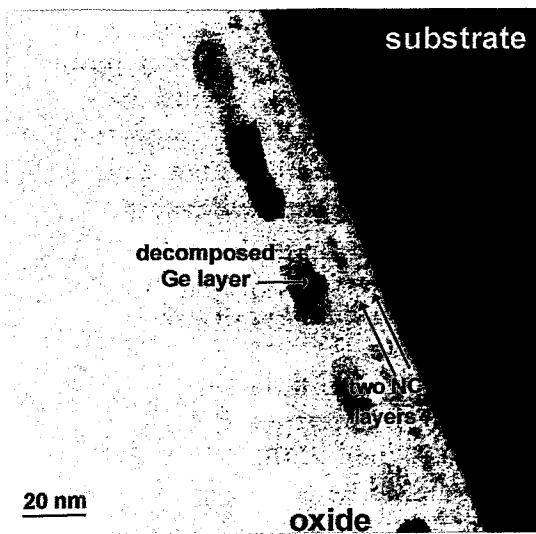

Figure 5.24: CS TEM image of SC3. E=70keV, $\phi = 7.0 \cdot 10^{15}Si^+/cm^2$, $T_{annealing} = 850°C$, $t_{annealing} = 750s$. The arrows point to the two NC layers which appear in the oxide of the MOS-like structure. The amount of Ge, which remains at the position of the former Ge layer, has formed spheres of 10...20 nm in diameter.

Figure 5.25: TRIDYN profiles corresponding to fig. 5.24. Note, that Si excess occurs only at the oxide-substrate IF. Moreover, Ge monomers are available in supersaturation in the oxide due to ion mixing.

The striking feature of fig. 5.24 is the formation of two NC layers in the oxide. One layer is next to the oxide-substrate interface, the other is close to the Ge layer-oxide interface. In comparison with the TRIDYN profiles in fig. 5.25, the positions of the NC δ-layers correspond to the tails of Si excess profile and the germanium profile. This
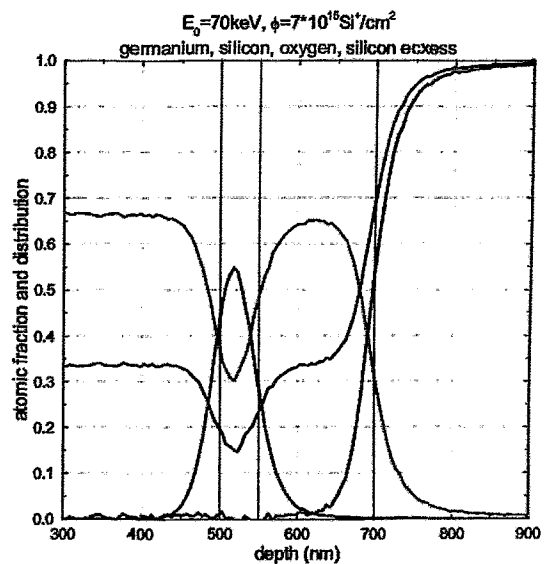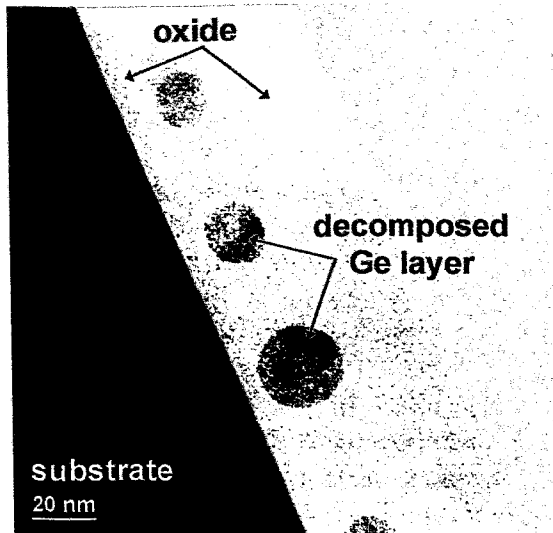
Figure 5.26: CS TEM image of SC3. This sample was not irradiated prior to thermal treatment.
$T_{\text{annealing}} = 950°C$, $t_{\text{annealing}} = 120s$.
The Ge layer merely decays into spheres if the sample is heated above $T_{\text{melting}}(\text{Ge})$. Thus, a δ-layer of NCs of 2...3 nm in diameter does not occur in the oxide.

scenario reminds of the outcomes of the 3D-KLMC simulations presented above. Both NC δ-layers appear in the TEM image since Ge monomers migrate during thermal annealing through the oxide attaching to Si precipitates which are formed by excess Si at the oxide-substrate interface. If no Si precipitates were at this very position, Ge monomers would directly condense on the Si substrate. Thus, the existence of Si precipitates at the expected position is proven – as the following TEM images confirm. Fig. 5.26 proves that the 5 nm Ge layer decays into spheres of 10...30 nm in diameter if the sample is heated above $T_{\text{melting}}(\text{Ge}) = 937°C$ without being irradiated previously. In this case, no NC layers appear in the MOS oxide.

Figs. 5.27, 5.28, 5.29, and 5.30 exhibit high resolution CS images paying attention to the influence of the relevant process parameters – annealing temperature, $T_{\text{annealing}}$, and ion fluence, ϕ – on the formation of the NC ensemble.

Fig. 5.27 depicts two NC δ-layers in the oxide as being described above in fig. 5.24. Here, the smallest distance between the NCs and the oxide-substrate IF is about 1.5 nm. With increasing temperature budget (see fig. 5.28, 5.29, and 5.30), the NC layer close to the oxide-substrate IF dissolves and only one NC layer remains in the oxide which was predicted by Ostwald ripening (compare figs. 5.4.2 and 5.4.3). The distance of the remaining NC layer to the oxide-substrate IF, i.e. the width of the denuded zone, increases with increasing annealing budget, i.e. with temperature and time of annealing, which coincides with the model of the diffusion length, $\lambda \propto \sqrt{D(T)t}$. The largest denuded zone of about 6 nm in width is observed for the highest annealing budget, namely for $T_{\text{annealing}} = 1050°C$ and $t_{\text{annealing}} = 750s$ (see fig. 5.30).

All TEM images demonstrate that Ge monomers, which attach to Si precipitates, enhance their contrast in TEM. Thus, the existence of Si precipitates, which emerge at the oxide-substrate IF during phase separation of SiO_x into SiO_2 and Si, is proven. Moreover, the resulting NCs collectively arrange themselves in a δ-layer which is separated from the oxide-substrate IF by a denuded zone. In addition, the spherical NCs are separated from each other by the SiO_2 matrix.

The width of the denuded zone, the mean distance between the NCs in the δ-layer, and the mean diameter of the NCs in the δ-layer are the characteristic quantities of
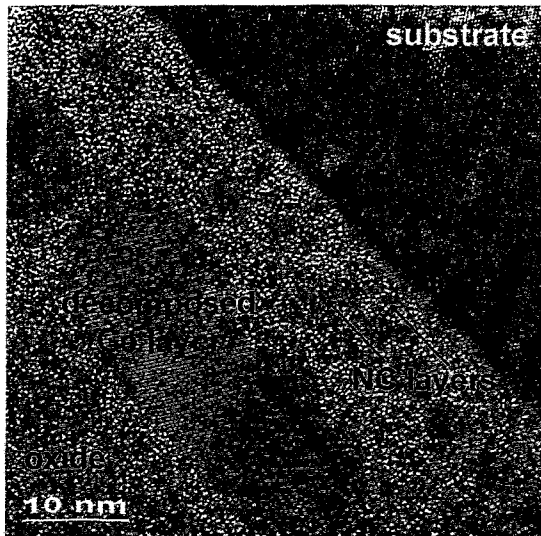
Figure 5.27: CS TEM image of SC3. E=70keV, $\phi = 7.0 \cdot 10^{15} \text{Si}^+/\text{cm}^2$, $T_{\text{annealing}} = 950°\text{C}$, $t_{\text{annealing}} = 30\text{s}$.
Two NC δ-layers occur in the oxide. The dunuded zone is about 1.5 nm in width.
For equal diameter, the grey scale of an individual cluster qualitatively indicates the Ge content. Thus, NCs close to the substrate, in which Si dominates, are brighter than those close to decomposed Ge layer.
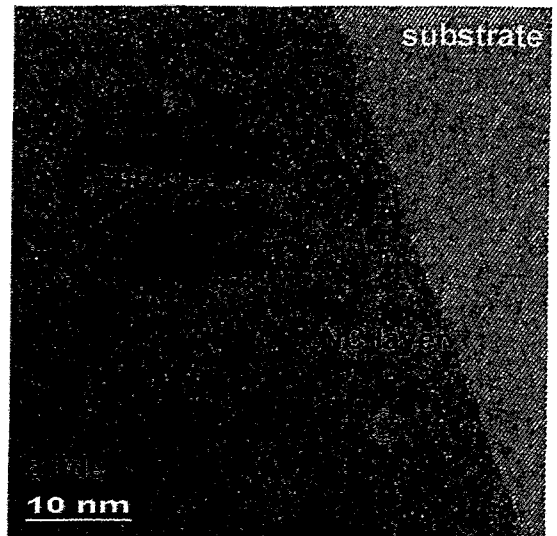
Figure 5.28: CS TEM image of SC3. E=70keV, $\phi = 7.0 \cdot 10^{15} \text{Si}^+/\text{cm}^2$, $T_{\text{annealing}} = 1050°\text{C}$, $t_{\text{annealing}} = 750\text{s}$.
Only one NC layer remains with increasing annealing budget.
The NCs become even crystalline (circle), however, the tininess prevents the precise determination of the lattice constant in order to calculate the $\text{Si}_x\text{Ge}_{1-x}$ composition of the cluster.
The denuded zone is about 4 nm in width. However, the large Ge sphere bulges in the NC δ-layer as soon as it approaches the layer.

this organizing process. Therefore, one may legitimately entitle this process the "self-organization" of a NC δ-layer.

It has semi-quantitatively been demonstrated that the denuded zone expands with increasing annealing budget (T,t) which can be explained in the picture of the diffusion length, $\lambda = \sqrt{D(T)t}$. In every case, the NCs show a mean diameter of about 3 nm. The mean NC diameter can only approximately be determined since the border between an individual NC and the surrounding oxide is not exactly measurable.

These results are also confirmed by TEM PV images which are presented in figs. 5.31 and 5.32, finally.
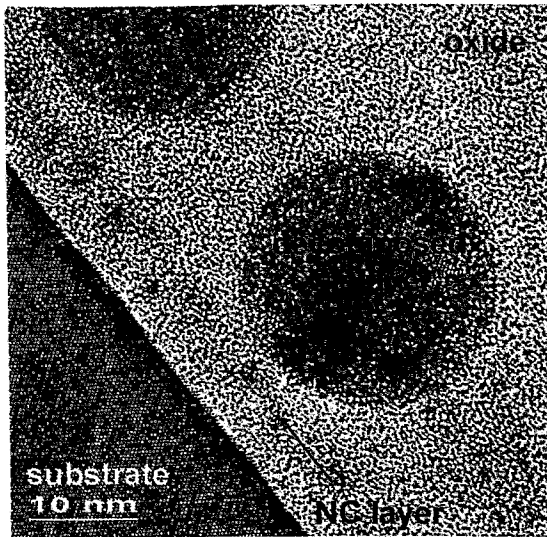
Figure 5.29: CS TEM image of SC3.
E=70keV, $\phi = 3.0 \cdot 10^{15} Si^+/cm^2$,
$T_{annealing} = 950°C$, $t_{annealing} = 750s$.
A NC δ-layer has formed at a distance of
about 3 nm from the oxide-substrate in-
terface. The NC diameter is hard to de-
termine – 3 nm is an approximate value.
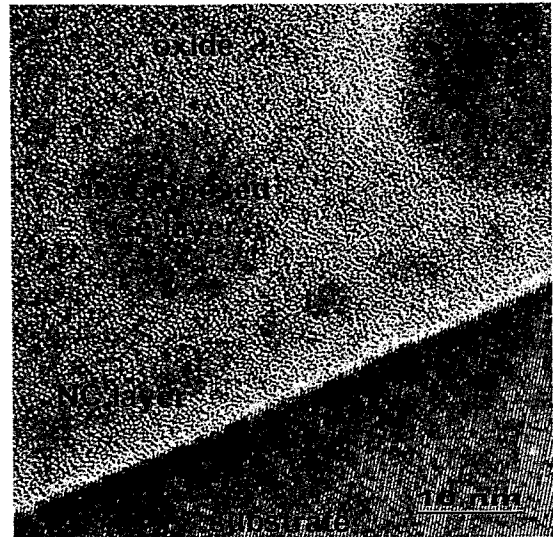
Figure 5.30: CS TEM image of SC3.
E=70keV, $\phi = 3.0 \cdot 10^{15} Si^+/cm^2$,
$T_{annealing} = 1050°C$, $t_{annealing} = 750s$.
The denuded zone is about 6 nm in width
which is in agreement with the highest an-
nealing budget in this case. Here, the NC
diameter is about 4 nm.
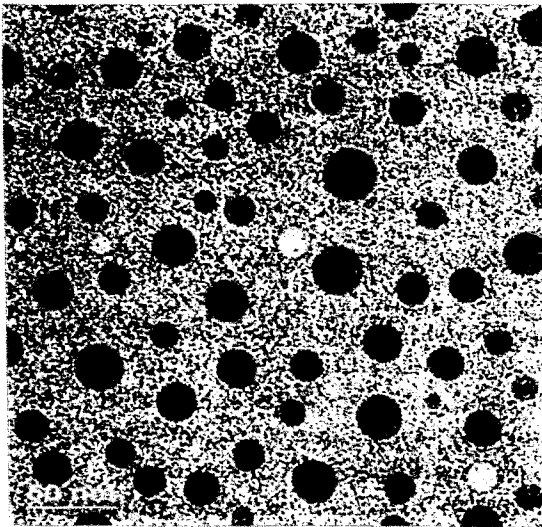
Figure 5.31: PV TEM image of SC3.
E=70keV, $\phi = 3.0 \cdot 10^{15} Si^+/cm^2$,
$T_{annealing} = 1050°C$, $t_{annealing} = 750s$.
The Ge layer has decayed in Ge spheres
of 10...30 nm in diameter during thermal
annealing with $T_{annealing} > T_{melting}(Ge)$.
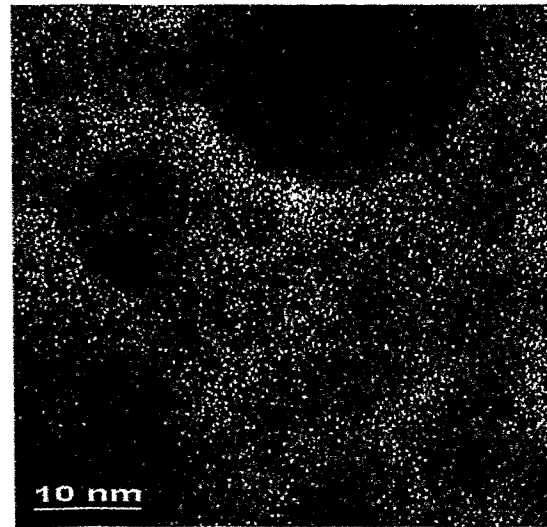
Figure 5.32: PV TEM image of SC3.
This is the PV image corresponding to the
CS image in fig. 5.30. Dark-grey spheri-
cal spots appear between the Ge spheres
which correspond to the NCs in the δ-
layer. The contrast to the surrounding
oxide is rather weak, unfortunately.

Chapter 6

Gain of Understanding and Outlook

6.1 Summary of the Results

For the first time, the theoretically predicted mechanism of self-organization of Si NC δ-layers in the buried oxide of a MOS structure is experimentally proven according to the goal of this thesis.

The formation of the desired NC arrangement is divided into two major steps:

1. Ion mixing of the Si-SiO$_2$ interfaces during medium energy ion irradiation through the MOS layer stack transforms the system into a zone of SiO$_x$ $(x < 2)$.

2. Subsequent phase separation (via spinodal decomposition as well as nucleation and growth) results in the reformation of the buried SiO$_2$ layer which contains a δ-layer of Si NCs at a constant distance of a few nanometers from the SiO$_2$-Si interface.

Simulations with TRIM and TRIDYN throw light on the compositional changes which occur in the target during ion implantation. The simulation results are in semi-quantitative agreement with the outcomes of RBS and SIMS measurements. In particular, the mechanism of ion mixing of interfaces is examined by means of TRIDYN, the results of which can be used as data input in KLMC simulations elsewhere.

First annealing experiments (SC1) show that Si NCs of less than 3 nm in diameter, which are embedded in SiO$_2$, are not visible by high resolution TEM -- the most convincing structural method of analysis in this case. However, the simultaneous formation of a SiO$_2$ NC layer in the Si substrate can be demonstrated which confirms the theoretical prediction of KLMC simulations in a first degree.

In order to enhance the contrast of Si NCs in SiO$_2$, Ge is used as decorating element in the experimental investigations of SC2 and SC3. Examinations with high resolution TEM prove this mechanism of Si NC decoration. Thus, Si precipitates in the buried oxide layer can successfully be revealed. Besides the mere presence of tiny Si NCs in the oxide, the collective and self-organizing arrangement of the NCs in a δ-layer is observed in TEM. The NC δ-layer is separated from the substrate by a denuded zone, the width of which increases with an increasing thermal budget of annealing (T,t). This is consistent with the model of the diffusion length, $\lambda = \sqrt{D(T)t}$.

All in all, the theoretically predicted mechanism of phase separation of an ion-beam-mixed Si-SiO$_2$ interface, in the course of which NC δ-layers emerge in the oxide, is

structurally proven by the experiments performed.

Due to synergetic effects between experiment and theory, a buried δ-layer of NCs can be produced in a bottom-up approach which is of prominent interest from a technological point of view, particularly in terms of future multidot nano-flash memories.

The following sequence of figures summarizes the results from a pictorial point of view. Here, results of SC1 and SC3 are portrayed.
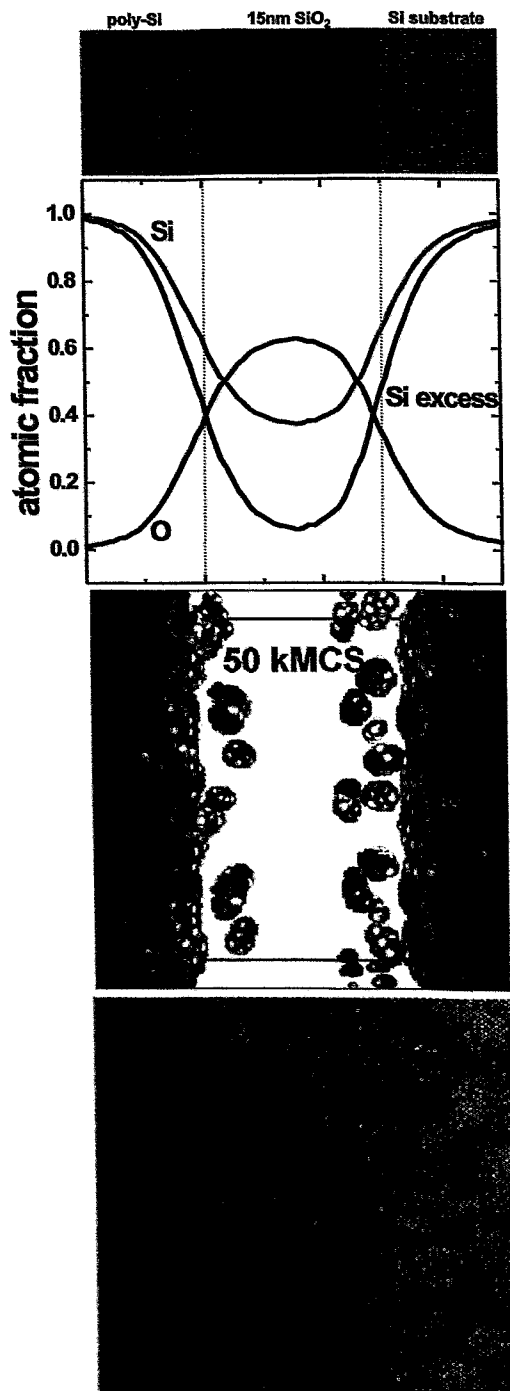
Figure 6.1: Course of investigations in the case of SC1

(a) Block diagram of the initial MOS-like sample structure.

(b) SC1 after ion irradiation. This fig. shows a TRIDYN simulation for $\phi = 1 \cdot 10^{16}$ Si$^+$/cm^2 and $E_0 = 100$ keV. The profiles indicate the compositional changes of the system which are due to ion mixing.
Note, that the black curve was calculated with $c_{Si,excess}(x) = c_{Si}(x) - 0.5 \cdot c_O(x)$.

(c) According to this KLMC snapshot (perfomed by K.-H. Heinig, FZR), theory predicts that NC layers emerge at the irradiated interface during phase separation. Phase separation proceeds via spinodal decomposition (reformation of the IF) as well as nucleation and growth (formation of NC ensembles).

(d) One aspect of KLMC simulations is proven here, namely the formation of SiO$_2$ NCs of ≈ 3 nm in diameter in the Si substrate during annealing. Amorphous SiO$_2$ NCs break the symmetry of the Si single crystal which causes their observability in high resolution TEM. Nevertheless, Si NCs within the oxide do not appear in high resolution TEM due to their weak contrast to the surrounding matrix.
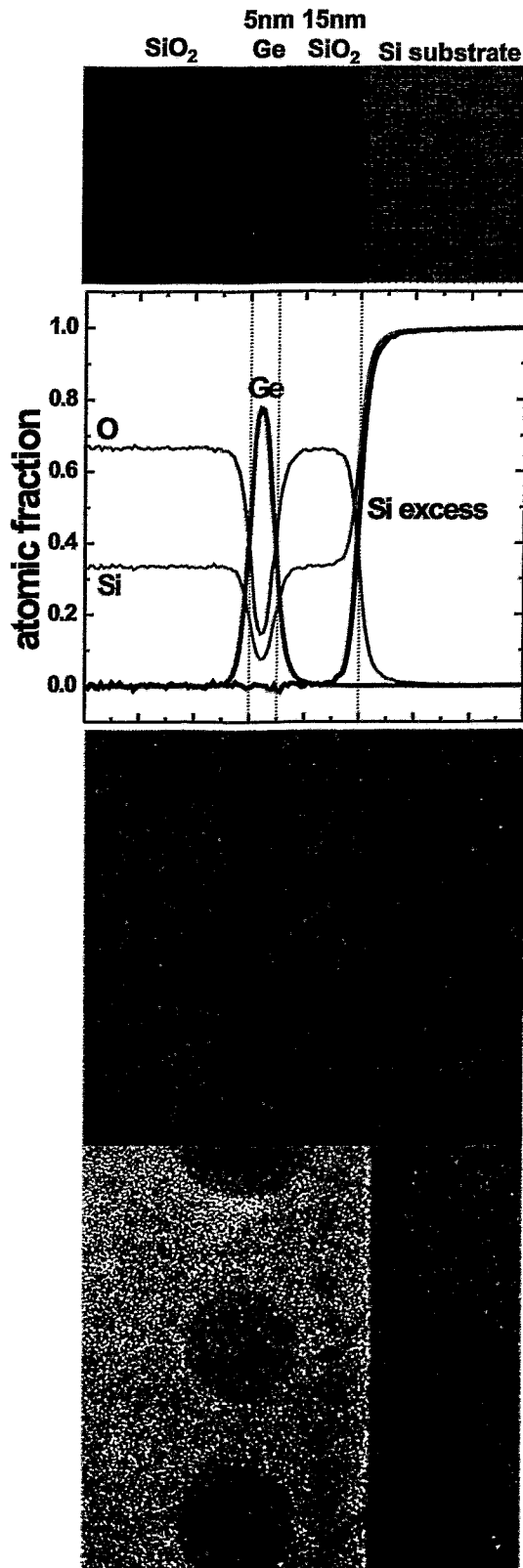
Figure 6.2: Course of investigations in the case of SC3

(a) Block diagram of the initial sample structure including a 5 nm Ge layer.

(b) SC3 after ion irradiation.
This fig. shows a TRIDYN simulation for $\phi = 3 \cdot 10^{15}$ Si$^+$/cm^2 and $E_0 = 70$ keV.
The profiles indicate the compositional changes of the system which are due to ion mixing.
Note, that the black curve was calculated with $c_{Si,excess}(x) = c_{Si}(x) - 0.5 \cdot c_O(x)$.
The widening of the Ge profile indicates that a considerable amount of Ge monomers is available in the 15 nm thin oxide layer after irradiation.

(c) As soon as phase separation starts, the former Ge layer decomposes.
Here, $t_{annealing} = 120$ s and $T_{annealing} = 850°$C. The SiO$_2$-Si IF is reformed and the crystallinity of the substrate is restored.
Interestingly, dark-greyish veils appear at a distance of ≈ 3 nm from the SiO$_2$-Si IF. This indicates the decoration of Si precipitates to a low degree.

(d) At a higher annealing budget, the effect of Ge decoration is clearly enhanced.
Here, $t_{annealing} = 750$ s and $T_{annealing} = 1050°$C. Spherical NCs of ≈ 3 nm in diameter appear which are collectively arranged in a δ-layer at a constant distance from the SiO$_2$-Si IF. The width of this "denuded zone" scales with increasing annealing budget. The large Ge spheres refer to the former Ge layer which is decomposed during annealing above the melting point of Ge.

6.2   Outlook on Future Investigations

EFTEM

The above considerations pointed out that Si NCs of less than 3 nm in diameter, which are embedded in an amorphous SiO_2 matrix, are not observable in common high resolution TEM. The weak mass contrast between Si NCs and the surrounding SiO_2 matrix is the reason for this unobservability.

In the bright field mode of conventional TEM, electrons of all energies are used for the formation of the image. Energy filters, however, allow image formation with electrons that have suffered specific energy losses in the sample. This technique, known as "energy-filtered TEM" (EFTEM), detects the chemical contrast within a specimen since it allows only those electrons to contribute to image formation which have lost a characteristic amount of energy during core ionizations of selected elements [FUB01]. Therefore, energy filtered images are highly promising in directly picturing tiny Si agglomerates within SiO_2. Thus, Ge decoration could be avoided and the pure Si-SiO_2 system could be studied. Moreover, statistical investigations in terms of NC densities or NC diameter distributions could reliably be performed in PV EFTEM images.

Structures of Higher Complexity

A very interesting structural feature emerged during the investigations of SC3. As "byproduct" of annealing, the former Ge layer decomposed into Ge spheres of 10...30 nm in diameter (see all the figures in subsection 5.5.3). Phase separation results in a double layer structure, i.e. the NC δ-layer emerged in between the Ge spheres and the Si substrate. This structural arrangement might improve the electronic behavior of non-volatile quantum memory devices. Very recently, Ohba et al. [OHR02] proposed a similar device structure. They claimed that the charge retention of the multidot nano-flash memory can significantly be improved using this "NC double-δ-layer" ordering (see the band diagram in fig. 6.3).
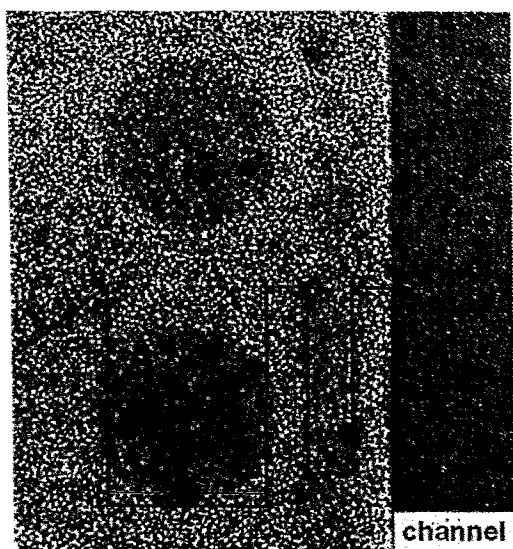
Figure 6.3: The interplay between quantum confinement and Coulomb blockade explains the better retention behavior of the "NC double-δ-layer" structure.
Electrons can easily be injected into the larger cluster via the double tunnel junction. In the storage mode, however, charge dissipation between the large cluster and the transistor channel is suppressed by the energy barrier of the small cluster (compare fig. 2.8).

More investigations are, therefore, necessary in order to determine whether the pre-

sented "NC double-δ-layer" structure can reliably be reproduced. Moreover, it is indispensable to examine the influence of the process parameters, e.g. initial layer thickness, ion fluence, or annealing conditions, on the size distribution of the two NC layers. In addition, the substitution of the initial Ge layer by a Si layer is worth being examined as well, particularly from an electronic point of view.

Synthesis of Structures under Irradiation

In connection with the previous case, inverse Ostwald ripening (IOR) may be helpful in adjusting the cluster diameters. Heinig et al. [HEK03] emphasized that the evolution of a NC ensemble results in a unimodal NC size distribution if the system is irradiated with ions during annealing. In other words, large clusters shrink delivering monomers to the matrix which attach to smaller ones that consequently grow.

This mechanism could be employed to reduce and to equalize the size of the large clusters (spheres) in the "NC double-δ-layer" structure. Likewise, monomers become available in the oxide matrix which feed the clusters in the NC δ-layer which is close to the SiO_2-substrate interface.

"Sophisticated Annealing"

In the frame of the present work, constant annealing temperatures were applied for given annealing times.

The schematic phase diagram of the Si-SiO_2 system, however, opens far more possibilities of influencing the course of phase separation by varying the temperature of annealing as function of time: $T_{annealing} = T_{annealing}(t)$.

As pointed out in section 5.1, phase separation can proceed via spinodal decomposition or via nucleation and growth (compare fig. 6.4).
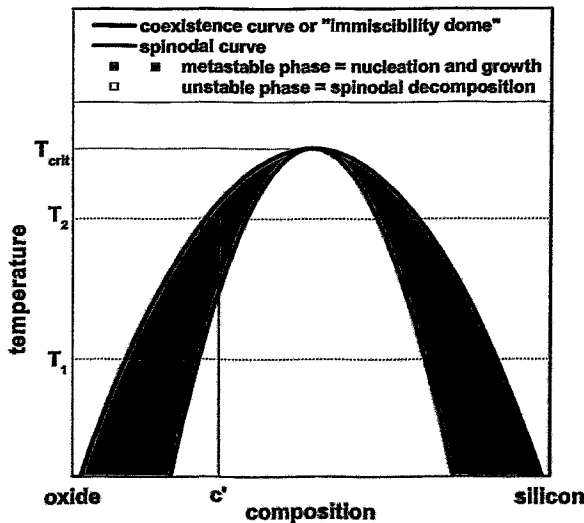
Figure 6.4: Varying the temperature of annealing as function of time can influence the regime of phase separation at a certain position in the sample depending on the local composition.

Here, for a local composition, c', phase separation proceeds via spinodal decomposition at $T = T_1$.

At higher $T = T_2$, however, the homogeneous SiO_x phase separates via nucleation and growth of Si precipitates in SiO_2.

The ability of selecting the local regime of phase separation is certainly helpful in defining the regions in the system where the minority phase precipitates. Thus, the subsequent evolution of an ensemble of NCs can sustainably be influenced.

Bibliography

[ADA93] *Technical Handbook ADDAX XM-A4 System.* Z.A.C., Montbonnot, 1993.

[AMS97] Amelinckx, S., D. van Dyck, J. van Landuyt, and G. van Tendeloo. *Handbook of Microscopy: Methods I.* Wiley-VCH, Weinheim, 1997.

[AZR87] Azzam, R. M. A., and N. M. Bashara. *Ellipsometry and Polarized Light.* North-Holland, Amsterdam, 1987.

[BIJ80] Biersack, J., and L. G. Haggmark. A Monte Carlo computer program for the transport of energetic ions in amorphous targets. *Nuclear Instruments and Methods in Physics Research*, 174 : 257, 1980.

[BIJ84] Biersack, J. P., and W. Eckstein. Sputtering Studies with the Monte Carlo Program TRIM.SP. *Applied Physics A*, 34 : 73, 1984.

[BOJ99] Borany, J. v., R. Grötzschel, K.-H. Heinig, A. Markwitz, B. Schmidt, W. Skorupa, and H.-J. Thees. The formation of narrow nanocluster bands in Ge-implanted SiO_2 layers. *Solid State Electronics*, 43 : 1159, 1999.

[BOJ02] Borany, J. v., T. Gebel, K.-H. Stegemann, H.-J. Thees, M. Wittmaack. Memory properties of Si^+ implanted gate oxides: from MOS capacitors to nvSRAM. *Solid State Electronics*, 46 : 1729, 2002.

[BOW94] Bolse, W. Ion-beam induced atomic transport through bi-layer interfaces of low- and medium-Z metals and their nitrides. *Materials Science and Engineering R*, 12 : 53, 1994.

[BRG80] Brebec, G., R. Seguin, C. Sella, J. Bevenot, and J. C. Martin. Diffusion du Silicium dans la Silice Aamorphe. *Acta Metallurgica*, 28 : 327, 1980.

[BUP92] Buseck, P. R., J. M. Cowley, and L. Eyring. *High-Resolution Transmission Electron Microscopy.* Oxford University Press, New York, 1992.

[CHM98] Chase, M. W., Jr. *NIST-JANAF Themochemical Tables* J. Phys. Chem. Ref. Data, Monograph 9, 1998.

[CRC94] *CRC Handbook of Chemistry and Physics.* 75th edition. CRC Press, Boca Raton, 1994.

[DOL85] Doolittle, L. R. Algorithms for the rapid simulation of Rutherford backscattering spectra. *Nuclear Instruments and Methods in Physics Research B*, 9 : 344, 1985.

[DOL86] Doolittle, L. R. A semiautomatic algorithm for Rutherford backscattering analysis. *Nuclear Instruments and Methods in Physics Research B*, 15:227, 1986.

[DUH99] Düsterhöft, H., M. Riedel, and B.-K. Düsterhöft. *Einführung in die Sekundärionenmassenspektrometrie - SIMS*. Teubner, Stuttgart, 1999.

[EBW98] Ebeling, W., J. Freund, and F. Schweitzer. *Komplexe Strukturen: Entropie und Information*. Teubner, Leipzig, 1998.

[ECW91] Eckstein, W. *Computer simulation of ion solid interactions*. Vol. 10 of *Springer series in materials science*. Springer, Berlin, 1991.

[FAI90] Fasol-Boltzmann, I. M., ed. *Ludwig Blotzmann Principien der Naturfilosofi*. Springer, Berlin, 1990.

[FAP89] Fahey, P., P. B. Griffin, and J. D. Plummer. Point defects and dopant diffusion in silicon. *Reviews of Modern Physics*, 61:289, 1989.

[FER59] Feynman, R. P. *Plenty of Room at the Bottom*. Lecture, December 1959.

[FLA89] Fletcher, A. J. *Thermal Stress and Strain Generation in Heat Treatment*. Elsevier Applied Science, London, 1989.

[FUB01] Fultz, B., and J. M. Howe. *Transmission Electron Microscopy and Diffractometry of Materials*. Springer, Berlin, 2001.

[GLW70] Glasow, W. M., and W. S. Semskow. *Die Germanium- und Silizium-Zweistofflegierungen*. Deutscher Verlag der Wissenschaften, Berlin, 1970.

[GOF81] Goodrich, F. C., and A. I. Rusanov (Eds.) *The Modern Theory of Capillarity*. Akademie-Verlag, Berlin, 1981.

[HAF98] Harbsmeier, F., and W. Bolse. Ion beam induced amorphization in α-quartz. *Journal of Applied Physics*, 83:4049, 1998.

[HAJ01] Hahn, J. *PVD – Physical Vapour Deposition*. 2. Dresdner Sommerschule Mikroelectronik. Dresden, July 2001.

[HAP00] Harrison, P. *Quantum Wells, Wires and Dots*. Wiley, Chichester, 2000.

[HEK01] Heinig, K.-H., B. Schmidt, M. Strobel, and H. Bernas. Inverse Ostwald Ripening and Self-Organization of Nanoclusters due to Ion Irradiation. *Materials Research Society Symposium Proceedings*, 647:O14.6, 2001.

[HEK03] Heinig, K.-H., T. Müller, B. Schmidt, M. Strobel, and W. Möller. Interfaces under ion irradiation: growth and taming of nanostructures. *Applied Physics A*, 77:17, 2003.

[HEK03p] Heinig, K.-H. *Private communication*. Rossendorf, Spring 2003.

[HIU99] Hilleringmann, U. *Silizium-Halbleitertechnologie*. Teubner, Stuttgart, 1999.

[HRB03] Hradsky, B., R. Rao, R. F. Steimle, M. Sadd, S. Straub, R. Muralidhar, and B. White. *Local charge storage in silicon nanocrystal memories.* 19th IEEE Non-Volatile Semiconductor Memory Workshop. Monterey, CA, February 2003.

[ISY94] Ishikawa, Y., and N. Shibata. Formation mechanisms of dislocation an Si island in low-energy SIMOX. *Nuclear Instruments and Methods in Physics Research B*, 91:520, 1994.

[JIJ00] Jiao, J., B. Johnson, S. Seraphin, M. J. Anc, R. P. Dolan, and B. F. Bordts. Formation of Si inlands in the buried oxide layers of ultra-thin SIMOX structures implanted at 65keV. *Materials Science and Engineering B*, 72:150, 2000.

[KER87] Kelly, R. The surface binding energy in slow collisional sputtering. *Nuclear Instruments and Methods in Physics Research B*, 18:388, 1987.

[KIC96] Kittel, C. *Introduction to Solid State Physics.* Wiley, New York, 1996.

[KIL97] Kimerling, L. C., K. D. Kolenbrander, J. Michel, and J. Palm. Light Emission from Silicon. *Solid State Physics*, 50:333, 1997.

[LII61] Lifshitz, I. M., and V. V. Slyozov. The kinetics of precipitation from supersaturated solid solutions. *Journal of Physics and Chemistry of Solids*, 19:35, 1961.

[MAA86] Mazzone, A. M. Defect Distribution in Ion-Implanted Silicon. *Physica Status Solidi A*, 95:149, 1986.

[MAJ81] Mayer, J. W., B. Y. Tsaur, S. S. Lau, and L.-S. Hung. Ion-beam-induced reactions in metal-semiconductor and metal-metal thin film structures. *Nuclear Instruments and Methods in Physics Research*, 182-183:1, 1981.

[MAD02] Mathiot, D. Silicon Self-Diffusivity Determination in Thermal SiO_2 from $^{30}Si/^{28}Si$ Isotopic Exchange. *NEON Report WP5.* September, 2002.

[MEN53] Metropolis, N., A: W. Rosenbluth, M. N. Rosenbluth, A. H. Teller, and E. Teller. Equation of state calculations by fast computing machines. *Journal of Chemical Physics*, 21:1087, 1953.

[MOT00] Mouthaan, T. *Semiconductor Devices Explained.* Wiley, Chichester, 2000.

[MOW84] Möller, W., and W. Eckstein. TRIDYN - a TRIM simulation code including dynamic composition changes. *Nuclear Instruments and Methods in Physics Research B*, 2:814, 1984.

[MOW85] Möller, W., and W. Eckstein. Ion mixing and recoil implantation simulations by means of TRIDYN. *Nuclear Instruments and Methods in Physics Research B*, 7-8:645, 1985.

[MOW86] Möller, W. A computer study of the collisional mixing of Pt in Si. *Nuclear Instruments and Methods in Physics Research B*, 15:688, 1986.

[MOW88] Möller, W., W. Eckstein, and J. P. Biersack. TRIDYN - binary collision simulation of atomic collisions and dynamic composition changes in solids. *Computer Physics Communications*, 51:355, 1988.

[MOW02] Möller, W., and M. Posselt. TRIDYN-FZR User Manual. FZR Publication Vol. 317, Rossendorf, 2002.

[MOW03p] Möller, W. *Private communication*. Rossendorf, Spring 2003.

[MUT02] Müller, T., K.-H. Heinig, and W. Möller. Size and location control of Si nanocrystals at ion beam synthesis in thin SiO$_2$ films. *Applied Physics Letters*, 81:3049, 2002.

[MUT03p] Müller, T. *Private communication*. Rossendorf, Spring 2003.

[MUY01] Murayama, Y. *Mesoscopic Systems*. Wiley, Weinheim, 2001.

[NAA97] Nakajima, A., T. Futatsugi, K. Kosemura, T. Fukano, and N. Yokoyama. Room temperature operation of Si single-electron memory with self-aligned floating dot gate. *Applied Physics Letters*, 70:1742, 1997.

[NAM94] Nastasi, M., and J. W. Mayer. Ion beam mixing in metallic and semiconductor materials. *Materials Science and Engineering R*, 12:1, 1994.

[NAM96] Nastasi, M., and J. M. Mayer. *Ion-Solid Interactions: Fundamentals and Applications*. Cambridge University Press, Cambridge, 1996.

[NAS93] Nakashima, S., and K. Izumi. Analysis of buried oxide layer formation and mechanism of threading dislocation generation in the substoichiometric oxygen dose region. *Journal of Materials Research*, 8:523, 1993.

[NIY00] Nishi, Y., and R. Doering (Eds.) *Handbook of Semiconductor Manufacturing Technology*. Dekker, New York, 2000.

[OHR02] Ohba, R., N. Sugiyama, K. Uchida, J. Koga, and A. Toriumi. Nonvoltile Si Quantum Memory With Self-Aligned Doubly-Stacked Dots. *IEEE Transactions on Electron Devices*, 49:1392, 2002.

[OHT94] Ohzone, T., and T. Hori. A MOSFET with Si-implanted gate-SiO$_2$ structure for analog-storeage EEPROM applications. *Solid State Electronics*, 37:1771, 1994.

[OSW00] Ostwald, W. Über die vermeintliche Isomerie des roten und gelben Quecksilberoxyds und die Oberflächenspannung fester Körper. *Zeitschrift für Physikalische Chemie*, 34:495, 1900.

[PEM03] Perego, M., S. Ferrari, S. Spiga, E. Bonera, M. Fanciulli, and V. Soncini. Time of flight secondary ion mass spectrometry study of silicon nanoclusters embedded in thin silicon oxide layers. *Applied Physics Letters*, 82:121, 2003.

[PEM03p] Perego, M. *Private communication*. Milan, July 2003.

[PRI77] Prigogine, I. *Time, Structure and Fluctuations.* Nobel lecture, 8 December, 1977.

[PRI84] Prigogine, I., and I. Stengers. *Order out of Chaos.* Bantam, New York, 1984.

[RAC78] Rao, C. N. R., and K. J. Rao. *Phase transitions in Solids.* McGraw-Hill, New York, 1978.

[RES96] Reiss, S., and K.-H. Heinig. Self-structuring of buried SiO_2 precipitate layers during IBS: A computer simulation. *Nuclear Instruments and Methods in Physics Research B*, 112:223, 1996.

[RIE95] Rimini, E. *Ion Implantation.* Kluwer Academic, Boston, 1995.

[SCG96] Schatz, G., and A. Weidinger. *Nuclear condensed matter physics.* Wiley, Chichester, 1996.

[SCB02] Schmidt, B., D. Grambole, and F. Herrmann. Impact of ambient atmosphere on as-implanted amorphous insulating layers. *Nuclear Instruments and Methods in Physics Research B*, 191:482, 2002.

[SCJ99] Schmelzer, J., G. Röpke, and R. Mahnke. *Aggregation phenomena in complex systems* Wiley, Weinheim, 1999.

[SCJ03] Schmidt, J. U., and B. Schmidt. Investigation of Si nanocluster formation in sputter-deposited silicon sub-oxides for nanocluster memory structures. To be published in 2003.

[SCJ03p] Schmidt, J. U. *Private communication.* Rossendorf, Spring 2003.

[SCJ03t] Schmidt, J. U. *On the synthesis of silicon nanocrystal memories by sputter deposition.* PhD thesis, draft, 2003.

[SHP89] Shewmon, P. *Diffusion in Solids.* The Minerals, Metals and Materials Society, Warrendale, 1989.

[SHY98] Shi, Y., K. Saito, H. Ishikuro, and T. Hiramoto. Effects of traps on charge storage charateristics in metal-oxide-semiconductor memory structures based on silicon nanocrystals. *Journal of Applied Physics*, 84:2358, 1998.

[SHY99] Shi, Y., K. Saito, H. Ishikuro, and T. Hiramoto. Effects of Interface Traps on Charge Retention Characteristics in Silicon-Quantum-Dot-Based Metal-Oxide-Semiconductor Diodes. *Japanese Journal of Applied Physics*, 38:425, 1999.

[SIP69] Sigmund, P. Theory of Sputtering. I. Sputtering Yield of Amorphous and Polycristalline Targets. *Physical Review*, 184:383, 1969.

[SIP81] Sigmund, P., and A. Gras-Marti. Theoretical aspects of atomic mixing by ion beams. *Nuclear Instruments and Methods in Physics Research*, 182-183:25, 1981.

[SMR97] Smith, R. *Atomic and ion collisions in solids and at surfaces.* Cambridge University Press, Cambridge, 1997.

[STM83] Stavola, M., J. R. Patel, L. C. Kimerling, and P. E. Freeland. Diffusivity of oxygen in silicon at the donor formation temperature. *Applied Physics Letters,* 42 : 73, 1983.

[STJ93] Stoemenos, J. Microstructure of SIMOX buried oxide, mechanisms of defect formation and related reliability issues. *Microelectronic Engineering,* 22 : 307, 1993.

[STM96] Strobel, M., S. Reiss, and K.-H. Heinig. Evolution of nanocluster ensembles: Computer simulation of diffusion and reaction controlled Ostwald ripening. *Nuclear Instruments and Methods in Physics Research B,* 120 : 216, 1996.

[STM97] Strobel, M., S. Reiss, K.-H. Heinig, and W. Möller. Computer simulation of precipitate coarsening: a unified treatment of diffusion and reaction controlled Ostwald ripening. *Radiation Effects and Defects in Solids,* 141 : 99, 1997.

[STM99t] Strobel, M. *Modeling and Computer Simulation of Ion Beam Synthesis of Nanostructures.* PhD thesis, 1999.

[STM01] Strobel, M., K.-H. Heinig, and W. Möller. Three-dimensional domain growth on the size scale of the capillary length: Effective growth exponent and comparative atomistic and mean-field simulations. *Physical Review B,* 64 : 245422, 2001.

[SZS81] Sze, S. M. *Physics of Semiconductor Devices.* Wiley, New York, 1981.

[SZS98] Sze, S. M. (Ed.) *Modern Semiconductor Device Physics.* Wiley, New York, 1998.

[TAT92] Takagahara, T., and K. Takeda. Theory ot the quantum confinement effect on excitons in quantum dots of indirect-gap materials. *Physical Review B,* 46 : 15578, 1992.

[TIS96a] Tiwari, S., F. Rana, H. Hanafi, A. Hartstein, E. F. Crabbe, and K. Chan. A Silicon nanocrystals based memory. *Applied Physics Letters,* 68 : 1377, 1996.

[TIS96b] Tiwari, S., F. Rana, K. Chan, L. Shi, and H. Hanafi. Single charge and confinement effects in nano-crystal memories. *Applied Physics Letters,* 69 : 1232, 1996.

[TRNE] Compañó, R. (Ed.) *Technology Roadmap for Nanoelectronics.* 2nd ed. http://www.cordis.lu/ist/fetnidqf.htm, November 2000.

[TSD01] Tsoukalas, D., C. Tsamis, and P. Normand. Diffusivity measurements of silicon in silicon dioxide layers using isotropically pure material. *Journal of Applied Physics,* 89 : 7809, 2001.

[VOM26] Volmer, M., and A. Weber. Keimbildung in übersättigten Gebilden. *Zeitschrift für Physikalische Chemie*, 119:277, 1926.

[WAC61] Wagner, C. Theorie der Alterung von Niederschlägen durch Umlösen. *Zeitschrift für Elektrochemie*, 65:581, 1961.

[WUD97] Wu, D. T. Nucleation Theory. *Solid State Physics*, 50:37, 1997.

[ZIJ00] Ziegler, J. F. (Ed.) *Ion Implantation - Science and Technology*. Ion Implantation Technology, Edgewater, 2000.

[ZIJ02] Ziegler, J. F. et al. *TRIM manual*. Retrieved October 20, 2002 from the World Wide Web: http://www.srim.org